Synthesis and Characterisation of Porous Mixed-Ligand Metal-Organic Frameworks for Sorption Studies

BY

MBONZHE LUCCILE

A dissertation submitted in the fulfilment of the requirements of the Master of Science in the

Department of Chemistry

Faculty of Mathematical and Natural Sciences

University of Venda

Supervisor: Dr Eustina Batisai

Co-supervisor: Dr Clive Oliver

March 2022

PLAGIARISM DECLARATION

I, **Luccile Mbonzhe [student no: 14014046]** confirm that I know the meaning of plagiarism and hereby declare that this mini dissertation entitled “Synthesis and characterisation of porous mixed-ligand metal-organic frameworks for application in gas storage” submitted by me to the department of chemistry at the University of Venda is my original work and has never been submitted for any degree at any other university or institution. This dissertation does not contain any other person’s writing unless specifically acknowledged and referenced accordingly.

Signature: Luccile Date: 01/03/ 2022

ABSTRACT

Metal-organic frameworks (MOFs) have been identified as promising physisorption candidates because of their unique structures. MOFs are a class of crystalline materials consisting of coordinate bonds between metal ions and organic ligands. The permanent porosity of MOFs enables them to be applied as gas storage and, carbon capture and utilization materials. The main portion of this study describes the synthesis of new porous MOFs from simple building blocks. A total of four (4) organic ligands, namely; *N,N*'–bis–(3-pyridylmethyl)–benzophone diimide (**L1**), *N*,*N*'–bis–(3-pyridylmethyl)–biphenyl diimide (**L2**), *N,N'*–bis(pyridin-4–ylmethyl) naphthalene diimide, *N*,*N*'–bis–(3-pyridylmethyl)–biphenyl diimide (**L3**) and *N,N'*–*bis*(gly)–biphenyl diimide (**L4**) were successfully synthesized and characterized. The second part of this study describes the synthesis of five (5) new MOFs, namely; {[Zn$_2$(OBZ)$_2$(**L2**)]·(DMF)$_3$}$_n$ (**LMMOF01**), {[Zn(TPA)(**L4**)$_{0.5}$]·(DMF)$_2$}$_n$ (**LMMOF02**), {[Co$_3$(TPA)$_3$(**L1**)]·(DMF)$_4$}$_n$ (**LMMOF03**), {[Co(BYP)(**L4**)]·(H$_2$O)}$_n$ (**LMMOF04**) and {[Cu(**L4**)$_{0.5}$]·(DMF)}n (**LMMOF05**). The MOFs were synthesized from the reactions of the pyridyl N-donor diimide ligands, carboxylate O-donor co-ligands (terephthalic acid (TPA), 4,4-oxybis benzoic acid (OBZ) and 2,2-bipyridy (BPY)) and transition metal salts. The MOFs were characterized using single-crystal X-ray diffraction (SCXRD), powder X-ray diffraction (PXRD) and variable temperature (VT-PXRD). The thermal stability of MOFs was determined using thermogravimetric analysis (TGA) and hot stage microscopy (HSM). SCXRD revealed that **LMMOF01** and **LMMOF03** are 3-D, **LMMOF02** is 2-D while **LMMOF04** and **LMMOF05** are 1-D. The 2-D and 3-D MOFs possess channels that are occupied by the solvent molecules. The porosity of the MOFs was tested using carbon dioxide, nitrogen and hydrogen gases.

ACKNOWLEDGEMENTS

First and foremost, I would like to thank the Almighty God for the gift of life, the ability to learn, and for giving me the power to believe in myself and pursue my dreams and in moulding me into the strong and wiser woman that I am today.

I would like to express my genuine gratitude to Dr Eustina Batisai for her excellent supervision, drive, great suggestions, and for introducing me to the exciting field of Metal-Organic Frameworks.

My thanks also go to my co-supervisor Dr Clive Oliver for helping me with the analysis of my samples. I am very grateful for the lifetime experience I had at the university of Cape Town under your supervision.

I would also like to thank my HOD Dr SS Mnyakeni Moleele for his motivation, encouragement and for making my student life as simple as he did by removing all the obstacles I faced as far as my research environment was concerned.

I would also like to extend my gratitude to Mr Pandelani for helping me with the NMR results of my synthesized organic ligands.

I would like to thank Dr Leigh Loots from Stellenbosch University for diffraction and thermal analysis.

I owe my sincere gratitude to my selfless parents Mr and Mrs Mbonzhe for their support, unconditional love, and for always pushing me to be the best version of myself.

My deepest gratitude goes to my friends Murendeni Ndou, Thisundiwi Malusela, Rolivhuwa Mahwasane, Kedibone Muguru, Nonhlanhla Baloyi and Dr Nabanita for being there for me when I need them during my research. Thank you so much.

Last but not least, I would like to genuinely thank the National Research Foundation and Sasol Foundation for their financial support throughout my research.

DEDICATION

I would like to dedicate this thesis to my supportive family and my supervisor Dr E.Batisai who were always there for me every step of the way for the whole two years of my master's research.

TABLE OF CONTENTS

LIST OF FIGURES

LIST OF SCHEMES

TABLES

ABBREVIATIONS

1-D	One dimensional
2-D	Two dimensional
3-D	Three dimensional
ASU	Asymmetric unit
BET	Brunauer-Emmett-Teller
CCDC	Cambridge Crystallographic Data Centre
CSD	Cambridge Structural Database
DMF	Dimethylformamide
MOF	Metal-organic framework
PXRD	Powder X-ray diffraction
SBU	Secondary building unit
SCXRD	Single Crystal X-ray diffraction
TGA	Thermogravimetric analysis
°C	Degree Celsius
ETOH	Ethanol
H	Hour
MeOH	Methanol
TGA	Thermogravimetric Analysis
CO_2	Carbon dioxide
CH_4	Methane
H_2	Hydrogen
PCP	Porous coordination polymers
L1	*N,N′*–bis–(3-pyridylmethy)–benzophone diimide
L2	*N,N′*–bis–(3-pyridylmethy)–biphenyl diimide
L3	*N,N′*- bis(pyridin-4-ylmethyl) naphthalene diimide
L4	*N,N′-bis*(gly)- biphenyl diimide
LMMOF01	$\{[Zn(OBZ)(L2)_{0.5}]\cdot(DMF)\}n$

LMMOF02	$\{[Zn(TPA)(L4)_{0.5}]\cdot(DMF)\}n$
LMMOF03	$\{[Co(TPA)(L1)_{0.5}]\cdot(DMF)\}n$
LMMOF04	$\{[Co(BYP)(L4)_{0.5}]\cdot(DMF)\}n$
LMMOF05	$\{[Cu(L4)]\cdot(DMF)\}n$
MW	Molecular weight
MP	Melting point
DMF	*N,N*-dimethylformamide
H_2O	water
IUPAC	International Union of Pure and Applied Chemistry
PSM	Post synthetic modification
VT-PXRD	Variable temperature
HSM	Hot stage microscope
NMR	Nuclear Magnetic Resonance
^{13}C NMR	Carbon-13 nuclear magnetic resonance
^{1}H NMR	hydrogen-1 nuclear magnetic resonance
FTIR	Fourier transform infrared
$CDCL_3$	Deuterated chloroform
COF	Covalent organic framework

ATOM COLOUR KEY

⚫	Carbon
⚪	Hydrogen
🔴	Oxygen
🔵	Nitrogen
🔵	Zinc
🟣	Cobalt
🟢	Copper

CHAPTER 1

INTRODUCTION

1.1. SUPRAMOLECULAR CHEMISTRY

The term supramolecular chemistry originates from the Latin word “supra” which means above and beyond.[1] The term “supramolecular chemistry” was first introduced in 1978 by J.M. Lehn and is defined as the chemistry of molecular assemblies and the intermolecular bond.[2] Supramolecular chemistry may be divided into two areas namely supermolecules and supramolecular assemblies.[2] Supermolecules are large structures consisting of two or more structures joined together *via* non-covalent interactions. Supramolecular assemblies are large assemblies of molecules that could be either large or small.[3] The different types of non-covalent intermolecular interactions include hydrogen bonds, coordinate bonds, $\pi\cdots\pi$ interactions, van der Waals forces, ionic bonds and hydrophobic interactions.[4] The important concepts of supramolecular chemistry involve molecular self-assembly, host-guest complex, template synthesis, mechanically interlocked molecular architecture, dynamic covalent chemistry and molecular imprinting techniques.[5] Host-guest chemistry is a popular branch of supramolecular chemistry in which two or more molecules are linked by non-covalent interactions resulting in the formation of a host-guest complex.[5] The host molecule is usually a large molecule which has a complementary binding site unique to a specific guest molecule. Metal-organic frameworks are good examples of supramolecular complexes due to their host-guest complex interactions.[6]

1.2. CRYSTAL ENGINEERING

Crystal engineering is a field of supramolecular chemistry.[7] G. R Desiraju defined crystal engineering as “the understanding of intermolecular interactions in the context of crystal packing and the utilization of such understanding in the design of new solids with desired physical and chemical properties”.[3] Crystal engineering involves the study of intermolecular interactions, packing modes and crystal properties.[3] New solid forms can be designed and synthesized based on the selection of building blocks known as supramolecular synthons.[8] Therefore, it is possible to predict, to a certain extent, the supramolecular synthons that may form between two or more molecules.[7]

1.2.1. Supramolecular synthons

Supramolecular synthons are defined as “structural units within supermolecules formed and brought together by known synthetic operations involving intermolecular interactions”.[9] Supramolecular synthons are repeating structural elements in crystalline structures that control the rational design of supramolecular architectures based on a small number of repeating patterns.[5] These structural units represent different ways in which functional groups of molecules interact with each other as shown in Figure 1.2.[20] Supramolecular synthons are subdivided into homosynthons and heterosynthons.[16] Homosynthons result from the interactions between identical functional groups (Figure 1.1) whereas heterosynthons result from the interactions between different functional groups (Figure 1.2).[10] The identification and recognition of supramolecular synthons is a key step in constructing and analysing crystalline structures such as pharmaceutical co-crystals and metal-organic frameworks.[11]

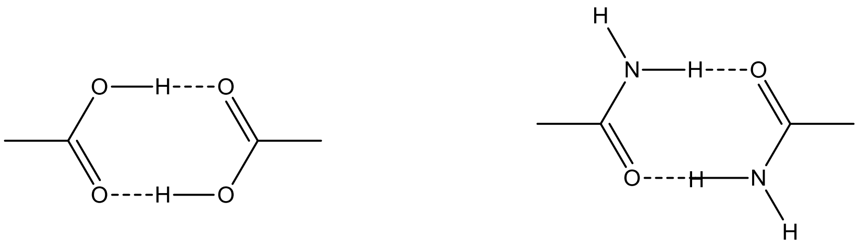

Carboxylic acid dimer

Amide dimer

Figure 1.1 Some common supramolecular homosynthons.

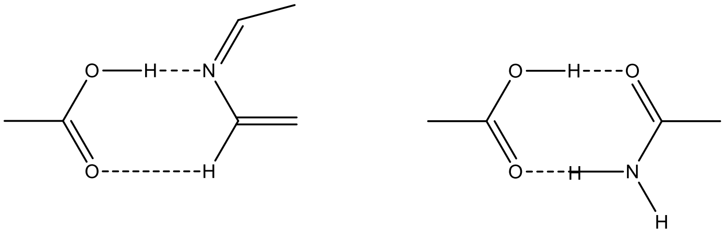

Carboxylic acid-pyridine

Carboxylic acid-amide

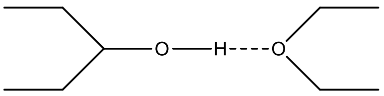

Alcohol-ether

Figure 1.2 Some common supramolecular heterosynthons.

1.3. INTERMOLECULAR INTERACTIONS

The existence of intermolecular interactions was first suggested by Johannes Diderik van der Waals in 1873.[12] Intermolecular interactions play an essential role in the self-assembly of molecular structures.[13] Self-assembly is a process whereby individual units interact with each other spontaneously without any external force resulting in highly ordered structures.[12] Intermolecular interactions serve as the glue holding molecules together in the solid state. Intermolecular interactions can be categorized into medium-range forces and long-range forces.[14] The medium-range forces define the molecular shape, size, and close packing of the structures while long-range forces involve the heteroatom interactions.[14] Long-range forces are also referred to as directional forces as they do not require contact between the individual molecules to exist. These forces often form between heteroatoms and carbon (C) or hydrogen (H) and form between two heteroatoms.[15] The medium-range forces are referred to as non-directional forces as they require contact between the structures to form.[15] Examples of intermolecular interactions and their relative strength are given in Table 1.1.

Table 1.1 Examples of intermolecular interactions and their strength.[16]

Molecular interactions	**Relative strength**	**Example**
Very strong hydrogen bond	15-40 kcal mol^{-1}	O—H···O═C
Strong hydrogen bond	4-15 kcal mol^{-1}	N—H···O═C
Weak hydrogen bond	<4 kcal mol^{-1}	CH···O
Coordinate bond	20-45 kcal mol^{-1}	Metal···O
Van der Waals interactions	0.5-20 kcal mol^{-1}	CH···π
π···π interactions	2-10 kcal mol^{-1}	π···π

1.3.1. DIRECTIONAL FORCES

1.3.1.1. Hydrogen bond

The hydrogen bond plays a significant role in crystal engineering and it is the most dependable directional interaction among all the intermolecular interactions.[17] Hydrogen bonds are normally stronger than ordinary dipole-dipole and dispersion forces, but they are weaker than true covalent and ionic bonds.[18] A hydrogen bond is an electrostatic attraction between a hydrogen atom in one polar molecule and an electronegative molecule (Figure 1.3).[19] Based on their strength, hydrogen bonds can be classified as very strong, strong and weak hydrogen bonds.[20] The strength of a hydrogen bond increases with the increase in electronegativity of the donor atom, because the electronegative atom will pull electron density away from the hydrogen making it electron deficient. The hydrogen atom can then get much closer to the electronegative atom of another molecule forming a hydrogen bond. This is made possible because of the reduced Pauli repulsion.[21] Hydrogen bonds play a vital role in determining the structure and properties of chemical and biological molecular systems.[22]

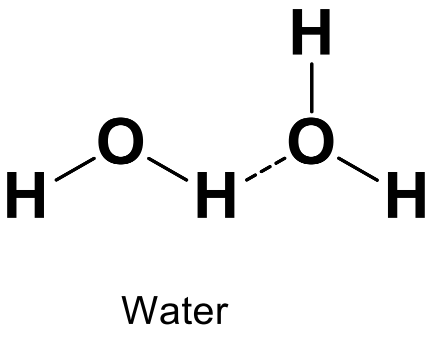

Figure 1.3 An illustration of a hydrogen bond formed between hydrogen and an oxygen atom in a water molecule.

1.3.1.2. Coordinate bond

A coordinate bond also known as a dative bond is defined as a covalent bond between two atoms in which both the electrons involved in the formation of the bond originate from one atom.[23] The atoms can form a bond because both their nuclei are attracted to the electron pair. This type of interaction is commonly seen in the coordination of organic ligands to metal ions during the formation of metal-organic frameworks.[24] The strength of the coordination bond ranges from 20 - 45 kcal mol^{-1} (Table 1.1).[20,13]

1.3.2. NON-DIRECTIONAL FORCES

1.3.2.1. $\pi\cdots\pi$ interactions

$\pi\cdots\pi$ interactions are intermolecular attractions that occur uniquely in aromatic molecules.[23] $\pi\cdots\pi$ interactions are defined as weak attractions that occur due to the modification of two different π electron clouds.[25] The strength of these interactions ranges from 2 - 10 kcal mol^{-1}.[20] Three of the most common $\pi\cdots\pi$ interactions are edge-to-face, stacked and offset (Figure 1.4).[26]

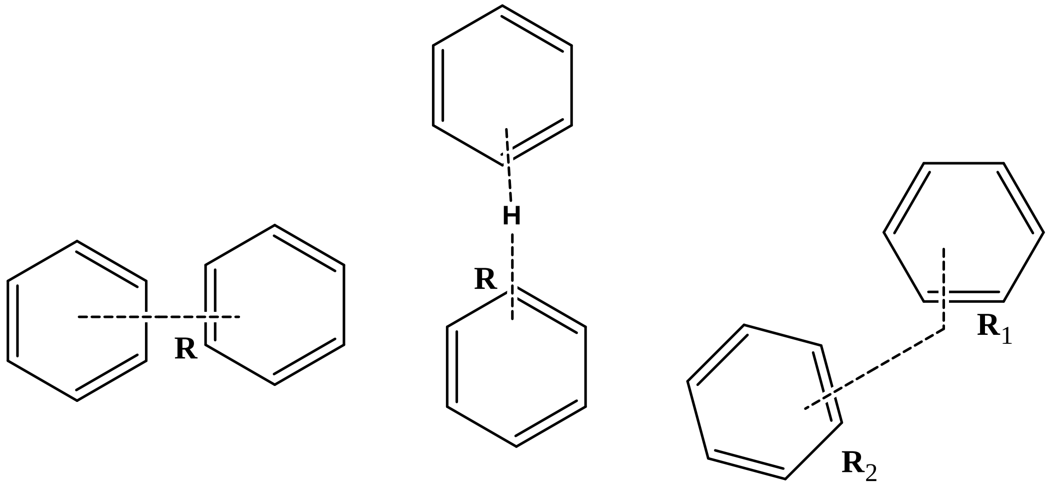

Figure 1.4 The three most common types of π⋯π interactions orientations that occur between aromatic compounds (a) stacked (b) edge-to-face and (c) offset.

1.3.2.2. Van der Waals interactions

Van der Waals forces are non-directional forces. These forces are important because they are universal and they exist even when the molecules are far apart.[28] Van der Waals forces are the weakest intermolecular interactions but their collective effect is much stronger and can cause a significant impact.[29] These interactions arise because of the polarisation of an electron cloud of an adjacent molecule which causes a weak electrostatic attraction.[30]

1.4. METAL-ORGANIC FRAMEWORKS

Metal-organic frameworks (MOFs) are crystalline porous materials described in the 1990s by Richard Robson (Figure 1.5).[32] This discovery was followed by the introduction of MOFs with permanent porosity in 1995 by Yaghi and Li.[33] MOFs consist of metal ions or metal clusters and organic ligands linked by coordinate bonds.[11] The organic ligands are often ditopic or polytopic which when coordinated to metal ions, produce architecturally robust 3-dimensional (3-D) crystalline materials (Figure 1.6).[34] MOFs possess large surface areas, high thermal stability and high chemical stability compared to other porous materials such as zeolites, covalent organic frameworks (COFs) and activated carbon.[35] Their porous nature enables reversible physisorption of gases like methane (CH_4), carbon dioxide (CO_2), and hydrogen (H_2).[36] As a result of their porosity, MOFs are considered to be ideal candidates for gas storage, gas capture, hydrocarbon separations and catalysis.[37] The synthesis of MOFs combines the two disciplines of chemistry (organic and inorganic) which are often viewed as distinct disciplines hence the name "metal-organic" frameworks.[26] The field of MOFs is new and rapidly growing worldwide because MOFs address many challenges related to energy and environmental sustainability.[38] There are currently 99 075 MOFs deposited in the CSD MOF subset (2020, version 5.38) (ccdc.cam.ac.uk) (Figure 1.7).

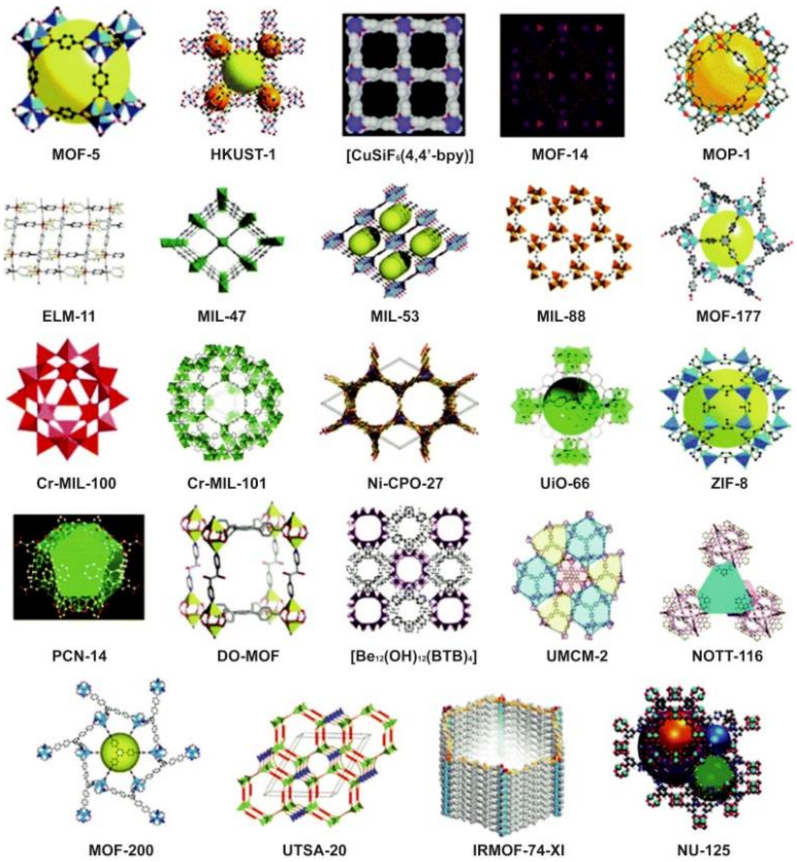

Figure 1.5 An Illustration of some of the popular MOFs synthesized by different research groups around the world. Figure taken from reference 31.

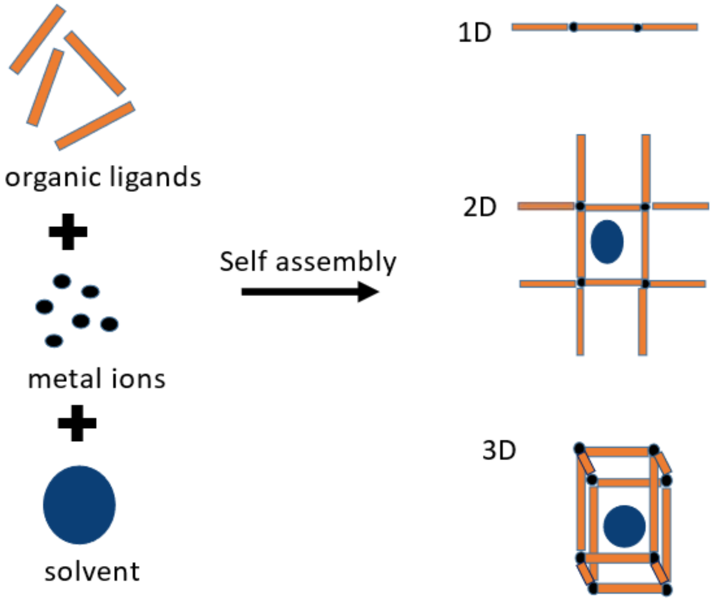

Figure 1.6 A pictogram displaying the self-assembly process of MOFs building blocks in the solution resulting in 1-, 2-, or 3- dimensional frameworks.[36]

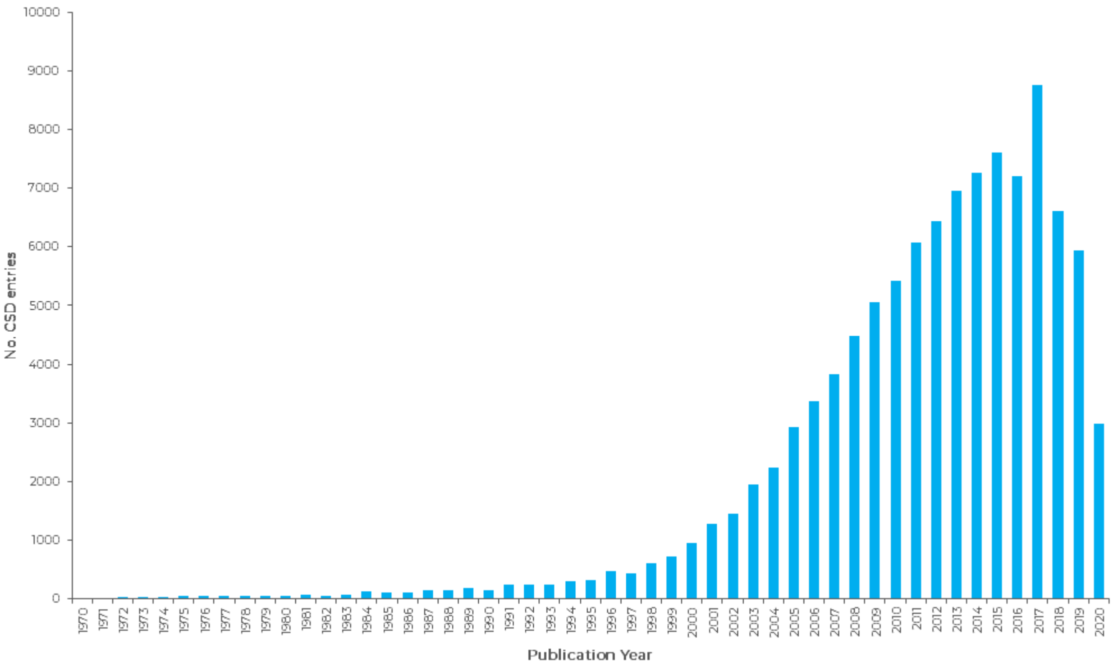

Figure 1.7 The number of MOFs reported in the Cambridge Structural Database (CSD) from 2000 to 2020. Retrieved from the CSD on 4th March 2020. Figure taken from ccdc.cam.ac.uk.

1.4.1. Synthetic methods for preparing MOFs

MOFs are formed through the self-assembly of metal ions and organic ligands in the presence of an organic solvent. Self-assembly is the spontaneous formation of ordered lattices under mild conditions.[39] The building blocks of MOFs can recognize each other and interact yielding continuous one-, two-, or three-dimensional frameworks (Figure 1.6).[40,41,42] The pore size, pore volume and the surface area of MOFs can be controlled by modifying the structures of the organic ligands. Two different organic ligands can also be incorporated together to synthesize mixed-ligand MOFs. The coordination of two organic ligands to a metal centre only occurs if one ligand has significant shared contributions to enable the ligation of the other ligand.[43] MOFs with increased topological complexity and desirable properties can be obtained by careful selection of organic ligands.[44]

1.4.1.1. Various methods used to synthesize MOFs

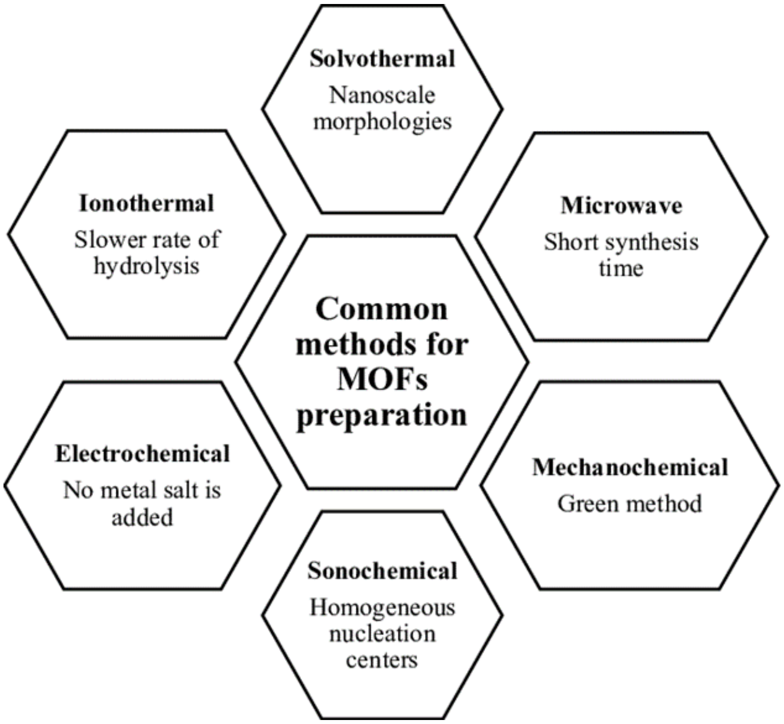

Figure 1.8 Common methods used to synthesize MOFs. Figure taken from reference 47.

There are different methods described in the literature that are used to synthesize MOFs. These methods include mechanochemical, solvothermal, slow evaporation, slow cooling, microwave-assisted, electrochemical, ionothermal and sonochemical methods (Figure 1.8). The synthetic method which is most commonly used in the synthesis of MOFs is the solvothermal method followed by the hydrothermal method, with the electrochemical method being the least utilized (Figure 1.9).[45,46] The most commonly used high boiling point organic solvents are *N,N*-dimethylformamide (DMF), *N,N*-diethyl formamide (DEF), and 1-methyl-2-pyrrolidone (NMP).[47] Mixtures of solvents such as DMF and ethanol (EtOH), DMF and water (H_2O), or DMF and methanol (MeOH) can also be used in the synthesis of MOFs.[48] During the synthesis process, crystalline products are formed which can then be characterized using X-ray diffraction techniques, thermal analysis and other characterization techniques.

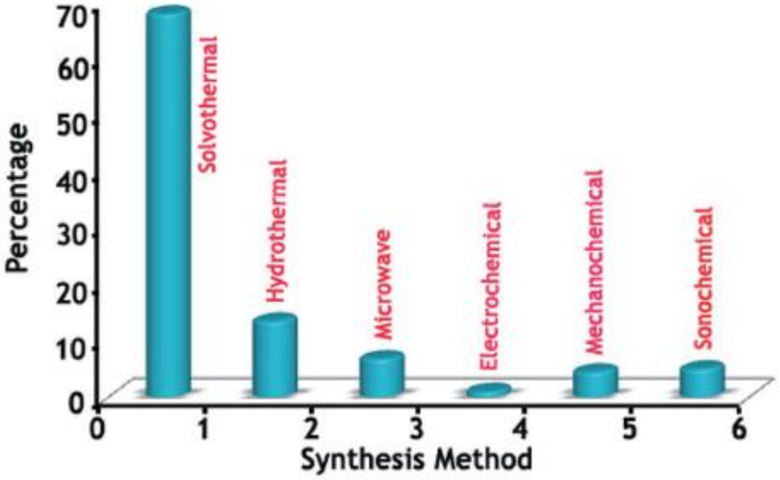

Figure 1.9 A bar graph summarizing the percentage of MOFs obtained using different synthesis methods. Figure taken from reference 46.

a) Solvothermal method

The solvothermal method is the commonly used method because the synthesis process can be easily controlled. The equipment used is fast and cheap. In addition, the method results in the formation of good quality crystals in high yield.[49] For higher temperature reactions Teflon-lined autoclaves are used because they can withstand very high temperatures while glass vials are used for low-temperature reactions (from 100 °C and below).[51]

b) Slow evaporation method

The slow evaporation method is a very simple method used to synthesize MOFs. This method is also cheap and does not require any external supply of energy.[36] The reactions take place at room temperature where the solvent or mixture of solvents is slowly allowed to evaporate.[52] The disadvantage of using this method is that it requires more time (7 days - 1 month) depending on the boiling point of the solvent used compared to other known conventional methods.[37] The organic linker and the metal ion are dissolved in the desired solvent in a vial or, a solution of an organic linker is added to a solution of a metal ion. Sometimes, mixtures of solvents are used to increase the solubility of the starting materials.[53]

c) Sonochemical method

The sonochemical method involves the application of intensive ultrasonic radiation.[45] Chemical and physical changes are induced by ultrasonic radiation due to cavitation processes. This results in the creation, growth and sudden breakdown of bubbles in a liquid creating short time local hot spots at higher temperatures and pressures.[54] These extreme conditions stimulate chemical reactions by the instantaneous establishment of a surplus of crystallization nuclei. Sonochemical methods have a fast crystallization time of around 30 minutes.

d) Microwave-assisted synthesis method

The microwave-assisted method involves heating the solution of the organic ligands and inorganic metal ions at high temperatures in a microwave.[54] Teflon-lined autoclaves which can withstand very high temperatures as well as high boiling organic solvents are used.[55] This method is very rapid and produces nano-sized crystals in a very short period in high yield and at a low cost.[55]

e) Electrochemical synthesis method

Electrochemical synthesis offers rapid reproducible production of MOFs in high yields.[55] The electrochemical method does not require metal salts right away because it uses separate cells (anodic and cathodic cells).[54] This method depends on the principle of providing the metal ions by anodic dissolution into the synthesis mixture containing the organic ligands and the electrolytes.[55]

f) Mechanochemical method

The mechanochemical method can be solvent-free or can involve a very small amount of solvent.[54] It is regarded as an environmentally friendly method as it produces very little or no solvent waste. This method relies on the application of mechanical force for coordinate bond formation. The mechanochemical force applied by either manual grinding or automatic ball mills enables mass transfer by reducing the particle size, and locally melting the reagents, thus, fast-tracking the time taken for the reaction to occur. [55]

1.4.2. Post-synthetic modification of MOFs

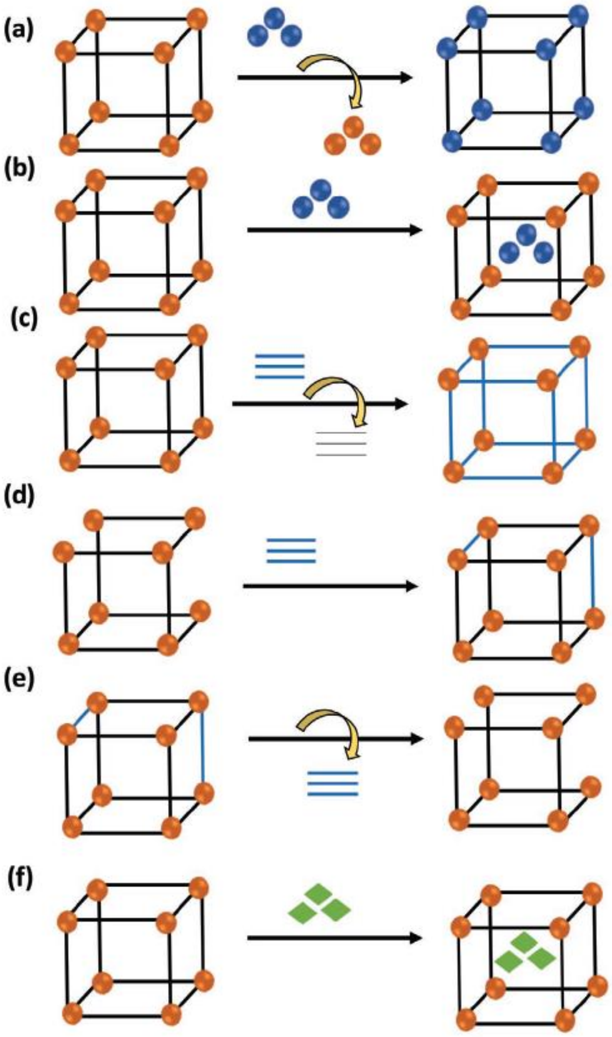

Figure 1.10 Different pathways in which MOFs can undergo PSM: a) exchange of metals, b) inserting metals in the synthesized MOFs structures, c) removing a ligand and inserting another, d) adding a ligand in the MOF structure, e) removing a ligand, and f) incorporating a guest molecule inside the pores of the MOF. Figure taken from reference 56.

Post-synthetic modification (PSM) is a technique used to incorporate desired functional groups into a synthesized MOF, resulting in a MOF with improved properties than those of the parent MOFs.[56] Synthesizing MOFs using ligands with different functionalities can be complicated because certain functionalities are not compatible with conditions used during the synthesis of MOFs.[57] PSM makes it possible for the desired functional groups to be introduced in MOFs after their synthesis using certain chemical interactions and reactions. Several methods of PSM that can be used to achieve structures with desired properties include the exchange of metals, inserting metals in the synthesized MOFs structures, removing a ligand and inserting another, adding a ligand in the MOF structure, and incorporating a guest molecule inside the pores of the MOF (Figure 1.10).[56]

1.5. ADSORPTION

The unique properties of the MOFs such as tunable pore size, large pore volumes and high surface areas make MOFs ideal candidates for gas sorption. Most MOFs are synthesized to analyze their gas sorption properties. Adsorption is the accumulation of a substance (adsorbate) on the surface of another substance (adsorbent) resulting in a higher concentration of molecular species compared to that in the bulk.[58] Desorption is the opposite of adsorption and it is the process by which the amount of the adsorbate is released from or through a surface. The term sorption is a special term which is used to describe the combined action of adsorption and absorption. Sorption is divided into physisorption and chemisorption. Physisorption involves the physical bonding of gas molecules to the surface of liquids or solids formed when gases are in contact with their surfaces at low temperatures while chemisorption takes place between the surface of a solid and the adsorbate resulting in the generation of new chemical bonds.

The physisorption process is analyzed by a plot of adsorbed amount versus relative pressure.[59] Six types of curves represent physisorption isotherms, namely type-I, type-II, type-III, type-IV, type-V and type-VI. (Figure 1.11).[60] Type-I, II and IV are both reversible and they are the most common physisorption curves.[61] Type-I is a horizontal plateau curve which displays a low-affinity adsorption process and is associated with microporous materials. This isotherm is formed during the analysis of gases in chemisorption systems. Type-II is a sigmoid type graph which is observed during physical adsorption. It is like a type-III curve, but it is not reversible. It is associated with mesoporous materials which may be composed of multilayers and pore condensation but no hysteresis. Type-III isotherms resemble a hyperbolic graph and are observed in systems where the amount of gas adsorbed increases without limit as its relative saturation approaches unity, where the adsorbate to sorbent interactions are weaker than the interaction between the adsorbates. Type-IV is a variant of type-II. It is characterized by finite multi-layer formation and shows hysteresis behaviour.[58] Type-V adsorption isotherm is an elongated S-shaped graph associated with mesoporous materials and pore condensation. It is similar to the type-III curve, but it is not reversible. The curve is attributed to sorbent-sorbent interactions. Type-VI is a very rare curve which displays stepwise multilayer adsorption which can be explained by layer-by-layer sorption on a uniform non-porous surface. [60] Type-VI is pronounced at low temperatures.

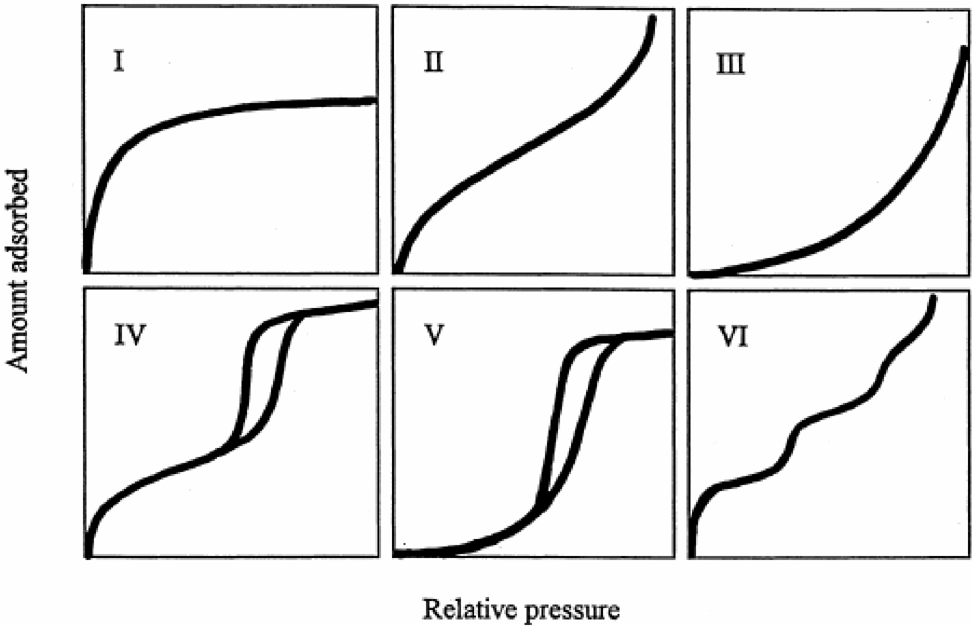

Figure 1.11 Different types of adsorption isotherms as classified by IUPAC. Figure taken from reference 60.

1.6. GAS SORPTION APPLICATION OF MOFs

Over the past few decades, industrials and academic researchers all around the world have been involved in the emergence of MOFs. MOFs have the potential to solve environmental and energy-related problems.[62] These structures are considered potential candidates for gas storage[63] and gas separation[41] owing to their permanently porous robust structures, flexible chemical composition,[38] high surface areas[42] and tunable pore size.[64] In addition, MOFs can be designed in such a way they are suited to a specific application. This can be achieved by carefully choosing the building blocks and introducing functionalities into the frameworks through PSM.[65,62] MOFs are ideal guest-responsive versatile materials because of their nature.[66] Approximately 10636 (ccdc.cam.ac.uk) MOFs have been synthesized and assessed for their gas sorption capabilities owing to their unique structural characteristics. Some examples such MOFs include ZTF-1, PCN-12, MIL-101(Cr), HKUST-1, Bio-MOF-11, MOF-5, MOF-74 and MOF-200.[67] (Figure 1.12).

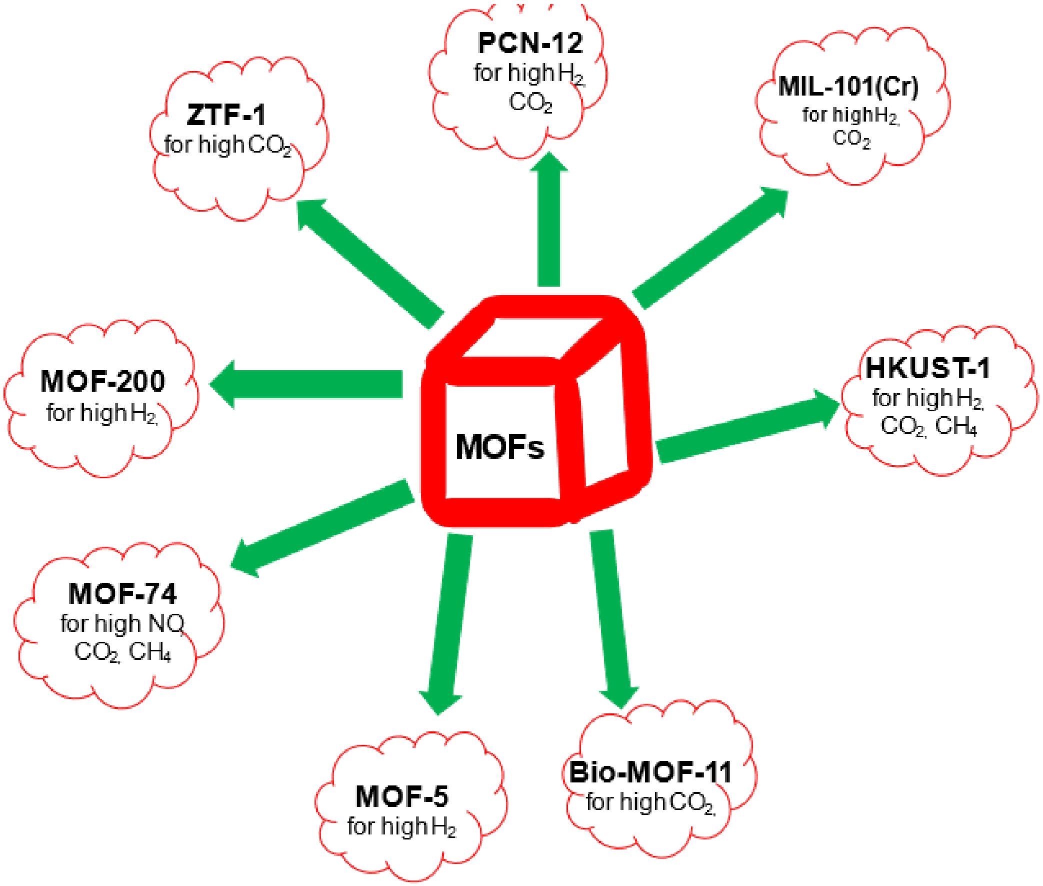

Figure 1.12 The structures of some of the MOFs that have been synthesized in the past for gas storage.

Hydrogen (H_2) has been recognized as a potential energy carrier which can successfully substitute the use of fossil fuels in the vehicular sector.[41] H_2 is a tasteless, colourless and non-toxic gas.[69] H_2 has a high gravimetric energy density than any other known potential energy fuel.[70] H_2 can be generated from water which is an abundant resource.[71] The by-products of burning H_2 in the presence of pure oxygen are water vapour and heat.[72] H_2 is considered green energy because it can be generated from renewable sources and it is also environmentally friendly. However, since the particles of H_2 gas are loosely packed, highly spread and have free movement, containing this gas is not an easy task. At near ambient conditions, H_2 is highly volatile, consequently, its volumetric energy density becomes too low for any practical applications.[73] The attempted methods for H_2 gas storage include the storing of H_2 in pressurized and cryogenic tanks.[73] These methods proved to be non-effective because of the higher amount of energy needed to liquefy H_2 than the amount of H_2, to keep the tanks cool, and to access the apparatus needed to stop hydrogen leakage thus hindering the use of H_2 as an energy fuel.[74] Thus the downside of the application of H_2 as a source of fuel energy is the absence of a safe, effective, and economically on-board hydrogen storage system.[75] MOFs have been identified as potential candidates for H_2 storage, thus several MOFs have been assessed for their H_2 storage capabilities.

MOF-5, also known as IRMOF-1, is a very popular MOF first described in 1999 as a pioneer MOF synthesized and evaluated for H_2 adsorption[76] owing to its high porosity, high surface area, and stable rigid structure in the absence of guest molecules.[77] At 78 K and 1 bar, MOF-5 adsorbed 4.5 weight %, which equates to 17.2 H_2 per Zn4O $(BDC)_3$ (where BDC is 1,4-benzene dicarboxylate) per formula unit. At ambient temperature, MOF-5 showed an increase in H_2 uptake with pressure until 1.0 weight % at 20 bar. It was also observed that the H_2 adsorption capacity of MOF-5 fluctuates to some degree depending on the method used to synthesize and activate the MOF.[32]

HKUST-1 first synthesized in 1999, is a 3–dimensional MOF named after the Hong Kong University of Science and Technology.[78] It is composed of copper ions coordinated to 1,3,5-benzene tricarboxylate ligands.[79] HKUST-1 MOF is very easy to synthesize and it possesses very large-sized pores and a large internal surface area. The MOF was assessed for hydrogen storage and it displayed a high hydrogen adsorption capacity at 77 K.[78] HKUST-1 was also tested for methane storage and it was found that it demonstrated a very high volumetric methane adsorption, meeting the required U.S. Department of Energy (DOE) new volumetric target at 65 bar when the limit of free space on the MOFs due to the packing of the structures is overlooked.[80]

Another MOF which adsorbed a high volume of methane (230 v/v at 290 K and 35 bar) is PCN-14.[81] This MOF material is built from copper(II) ions and 5,5’-(9,10-anthracenediyl) di-isophthalate units.[82] Another MOF which showed the potential to function as a methane storage material was MOF-519.[54] This MOF has a high methane volumetric storage capacity of 279 cm^3/g STP at a temperature of 298 K and a pressure of 80 bar because the pressure is measured at room temperature. Only the pressure is being varied and the other quantities are kept constant at STP.[54]

The primary source of energy used worldwide is the burning of fossil fuels which releases carbon dioxide (CO_2) into the atmosphere. The generation of energy by the burning of fossil fuels leads to global warming.[83] This leads to the absorption of some of the outgoing radiation and re-radiating it back towards the surface of the earth.[84] The effects of global warming include rising temperatures, shortage of water, an increase in wildfire threats, droughts and weed invasions.[85] Clearly, there is a need for clean energy to mitigate CO_2 emissions. To decrease and manage CO_2 levels, CO_2 could be captured and converted into valuable chemical products.[86] The MOF-based materials can be used as gas adsorbents and CO_2 capture and conversion catalysts. Features such as crystallinity, flexible pore dimensions, high surface area and structural stability make them ideal candidates for CO_2 capture and conversion.[31] MOFs are also exceptional heterogenous catalysts for the chemical conversion of pure CO_2.[88] The captured CO_2 can be converted to high-value products such as cyclic carbonate. Cyclic carbonates are compounds characterized by a carbonyl group flanked by two oxygen atoms and may be linear or cyclic.

1.7. MOTIVATION

The need to replace the current energy sources such as the burning of fossil fuels has driven an interest in green chemistry technology. MOFs have been identified as the most promising physisorption candidates owing to their unique structures and permanent porosity. The active research area of MOFs presents possibilities for solving the current climate change problems around the world. Experimental studies have shown that MOFs possess all the required characteristics to be used for gas storage and gas separation. This research project is aimed at synthesizing porous MOFs for gas sorption studies.

The project will firstly involve the synthesis and characterization of four (4) ligands namely *N,N′*–bis–(3-pyridylmethyl)–benzophone diimide **(L1)**, *N,N′*–bis–(3-pyridylmethyl)–biphenyl diimide **(L2)**, *N,N*- bis(pyridin-4-ylmethyl) naphthalene diimide, *N,N′*–bis–(3-pyridylmethyl)–biphenyl diimide **(L3)** and *N,N′-bis*(gly)-biphenyl diimide **(L4)** (Scheme 1.1). A Cambridge Structural Database (CSD) search revealed that ligands **L2** and **L3** have been investigated previously in the synthesis of MOFs while ligands **L1** and **L4** have not been used.

In the second part of the project, ligands **L1**, **L2** and **L3** will each be reacted with different transition metal salts in the presence of a carboxylate co-ligand (Scheme 1.1) while **L4** is reacted in the presence of a pyridyl ligand (Scheme 1.2) to generate crystalline porous MOFs. The MOFs will be synthesized using the mixed-ligand synthesis method under solvothermal conditions. This method incorporates different functional ligands in MOFs thus enhancing the stability of the MOF. In the third part of the project, the activated MOFs will be assessed for their gas sorption capabilities.

1.8. AIMS AND OBJECTIVES

This project aims to synthesize novel MOFs for gas sorption studies.

1.8.1. The objectives of this project are:

(i) To synthesize N-donor and pyridine donor organic ligand and characterize them using FTIR and NMR.
(ii) To prepare mixed-ligand MOFs based on carboxylate and pyridyl ligands.
(iii) To characterize the synthesized MOFs using single-crystal X-ray diffraction (SCXD) and powder X-ray diffraction (PXRD).
(iv) To evaluate the thermal stability of the synthesized MOFs using thermogravimetric analysis (TGA) and hot stage microscope (HSM).
(v) To assess gas sorption capabilities of the synthesized MOFs.

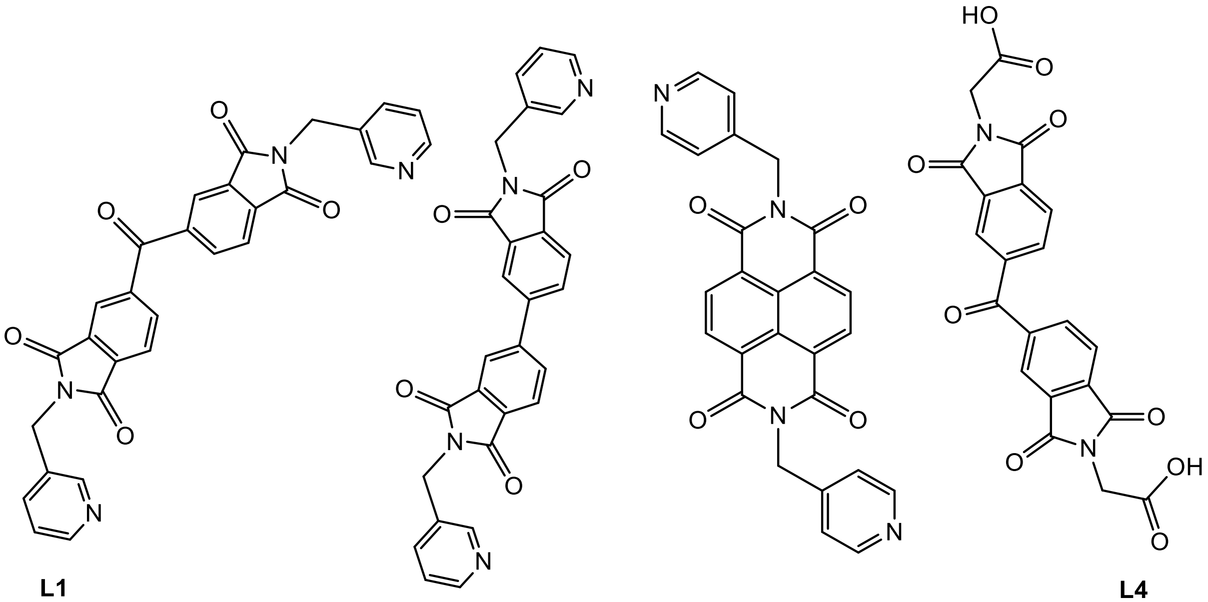

L1 **L2** **L3** **L4**

Scheme 1.1 The structures of the ligands used in this study.

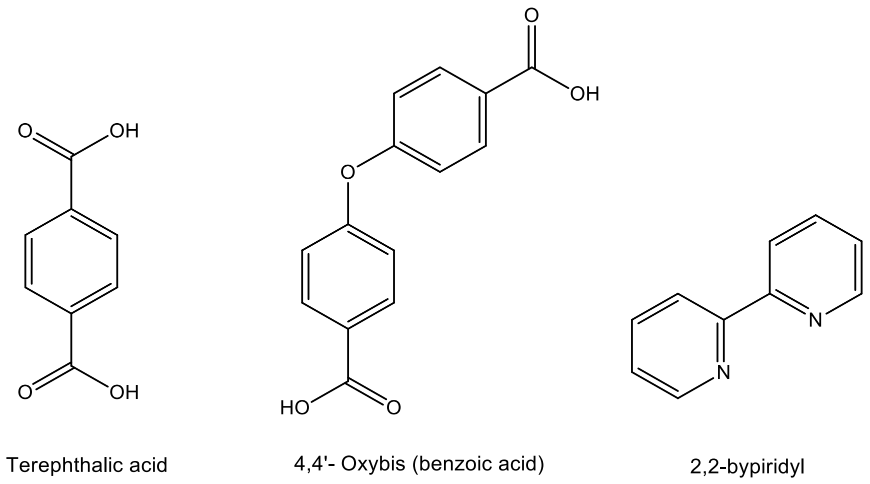

Scheme 1. 2 Structures of co-ligands used in this study.

1.9. THESIS OUTLINE

Chapter 2 outlines the synthesis and characterization of organic ligands and metal-organic frameworks (MOFs). The computer programs used to solve and analyse the MOFs structures are also discussed.

Chapter 3 discusses the SCXRD, PXRD, VT-PXRD, HSM, TGA and gas sorption data of $\{[Zn_2(OBZ)_2(\mathbf{L2})]\cdot(DMF)_3\}_n$ (**LMMOF01**), $\{[Zn(TPA)(\mathbf{L4})_{0.5}]\cdot(DMF)_2\}_n$ (**LMMOF02**) and $\{[Co_3(TPA)_3(\mathbf{L1})]\cdot(DMF)_4\}_n$ (**LMMOF03**).

Chapter 4 discusses the SCXRD, PXRD, HSM and TGA of two 1-D MOFs $\{[Co(BYP)(\mathbf{L4})]\cdot(H_2O)\}_n$ (**LMMOF04**) and $\{[Cu(\mathbf{L4})_{0.5}]\cdot(DMF)\}n$ (**LMMOF05**).

Chapter 5 gives a summary of the results of this project and proposed future work.

REFERENCES

1 J.M Lehn, *Pure Appl. Chem.*, 1978, **50**, 817–892.

2 J.M. Lehn, *Science*,1993, **260**, 1762.

3 G. R. Desiraju, *Angew. Chemistry- Int. Ed.*, 2007, **46**, 8342–8356.

4 D. Lu, Q. Huang, S. Wang, J. Wang, P. Huang and P. Du, J. Struct. Chem, 2019, **7**, 1–9.

5 D.V. Soldatov, and I.S. Terekhova, *J. Struct. Chem.*, 2015, **46**, 1–8.

6 F. Huang and E. V. Anslyn, *Chem. Rev.*, 2015, **115**, 6999–7000.

7 A. Nangia, *J. Chem. Sci.*, 2010, **122**, 295–310.

8 G.R. Desiraju, *Angew Chem. Int.*, 1995, **34**, 2311.

9 F. Krichen, S. Walha, J. Lhoste, A. Bulou, A. Kabadou and F. Goutenoire, *J. Mol. Struct.*, 2017, **1146**, 409–416.

10 J.D. Dunitz, *pure apple Chem. Int.*, 1991, **63**, 177.

11 J. Sosa, T. Bennett, K. Nelms, B. Liu, R. Tovar and Y. Liu, *Crystals*, 2018, **8**, 325.

12 A. K. Manna, *Chem. Soc. Rev.*, 2015, **4**, 892–899.

13 A. J. Misquitta, *Handb. Comput. Chem.*, 2017, **4**, 295–335.

14 G. R. Desiraju, *Angew. Chem. Int. Ed. Engl*, 2000, **34**, 2541.

15 G. R. Desiraju, *Chem. Soc. Rev.*, 2013, **135**, 9952–9967.

16 A. Nangia, *J. Chem. Sci.*, 2010, **122**, 295.

17 D. Braga, L. Brammer and N.R Champness, *Cryst.Eng. Comm.*, 2005, **7**, 1.

18 J. Lalnunsiama and V. Madhurima, *Pure Appl. Chem.*, 2010, **6**, 0–13.

19 G. C. Pimentel and A. L. Mcclellan, *Chem. A Eur. J.*, 1991, **22**, 347–385.

20 A. Nangia, *J. Chem. Sci.*, 2010, **122**, 295.

21 E. Arunan, G. R. Desiraju, R. A. Klein, J. Sadlej, S. Scheiner, I. Alkorta, D. C. Clary, R. H. Crabtree, J. J. Dannenberg, P. Hobza, H. G. Kjaergaard, A. C. Legon, B. Mennucci, D. J. Nesbit, *Pure Appl. Chem.*, 2010, **83,** 1637–1641.

22 C. N.R. Rao, *Pure Appl. Chem.*, 1972, **1**, 2.

23 M. M. Cooper, L. C. Williams and S. M. Underwood, *J. Chem. Educ.*, 2015, **92**, 1288–1298.

24 J. Evans, B. Garai, H. Reinsch et al., *Coord. Chem. Rev.*, 2019, **380**, 378–418.

25 C. R. Martinez and B. L. Iverson, *Chem. Sci.*, 2012, **3**, 2191–2201.

26 H.C. Zhou, J. R. Long and O. M. Yaghi, *Chem. Rev.*, 2012, **112**, 673–674.

27 R. Anjana, M. K. Vaishnavi, D. Sherlin, S. P. Kumar, K. Naveen, P. S. Kanth and K. Sekar, *Bioinformation*, 2012, **8**, 1220–1224.

28 R.H.S. Winterton, Plasma *Phys.*, 1970, **6**, 559–574.

29 G.R Desiraju, Chem. Educ. Res. Pract., 2005, **14**, 2123.

30 V. A. Parsegian, *Van der Waals forces: A handbook for biologists, chemists, engineers, and physicists*, 2005.

31 M. H. Yap, K. L. Fow and G. Z. Chen, *Green Energy Environ.*, 2017, **2**, 218–245.

32 N. Jiang, Z. Deng, S. Liu, C. Tang and G. Wang, *Chem. Soc. Rev.*, 2016, **33**, 2747–2755.

33 O. Yaghi, G. Li, and H. Li, *Angew. Chemie Int. Ed. English*, 1995, **34**, 207–209.

34 D. Nagaraju, D. G. Bhagat, R. Banerjee and U. K. Kharul, *J. Mater. Chem. A*, 2013, **1**, 8828–8835.

35 S. L. James, *Chem. Soc. Rev.*, 2003, **32**, 276–288.

36 C. Dey and T. Kundu, *Int. Educ. Stud.*, 2014, **70**, 3–10.

37 V. V. Butova, M. A. Soldatov, A. A. Guda, K. A. Lomachenko and C. Lamberti, *Russ. Chem. Rev.*, 2016, **85**, 280–307.

38 L. Jiao, Y. Wang, H. L. Jiang and Q. Xu, *Adv. Mater.*, 2018, **30**, 1–23.

39 A. Anumah, H. Louis, A. T. Hamzat and O. O. Amusan, *Chem. Soc. Rev.*, 2018, **3**, 283–305.

40 J. F. Stoddart and H. M. Colquhoun, *Tetrahedron*, 2008, **64**, 8231–8263.

41 D. J. Collins and H.-C. Zhou, *J. Mater. Chem.*, 2007, **17**, 3154.

42 Y. Zhao, Z. Song, X. Li, Q. SuN,N. Cheng, S. Lawes and X. Sun, *Energy Storage Mater.*, 2016, **2**, 35–62.

43 H. Furukawa and O. M. Yaghi, *J. Am. Chem. Soc.*, 2009, **131**, 8575–8883.

44 H. Furukawa, K. E. Cordova, M. O'Keeffe and O.M. Yaghi, *Science.*, 2010, **329**, 423–428.

45 J. Ru, X. Wang, F. Wang, X. Cui, X. Du and X. Lu, *Ecotoxicol. Environ. Saf.*, 2021, **208**, 111577.

46 E.A. Newton, A. Nimibofa, I. Azibaola Kesiye and W. Donbebe, *Am. J. Environ. Prot.*, 2017, **5**, 61–67.

47 B. Hashemi, P. Zohrabi, N. Raza and K. H. Kim, *TrAC - Trends Anal. Chem.*, 2017, **97**, 65–82.

48 F. Israr, D. K. Kim, Y. Kim and W. Chun, *Quim. Nova*, 2016, **39**, 669–675.

49 V.V. Butova, M.A. Soldatov, A.A. Guda, K.A. Lomachenko and C. Lamberti*, Russ. Chem. Rev.* 2016, **85,** 280

50 P.Pachfule, R. Das, P. Poddar and R. Banerjee, *Cryst. Growth Des.*, 2011, **11**, 1215–1222.

51 Y. Bae, D. Dubbeldam, A. Nelson, K. S. Walton, J. T. Hupp and R. Q. Snurr, *Chem. mater*, 2009, **111**, 131.

52 C. B. Carter and M. G. Norton, *Ceram. Mater.*, 2013, **1**, 523–542.

53 K. Seevakan and S. Bharanidharan, *Int. J. Pure Appl. Math.*, 2018, **Vol 119**, 5743–5758.

54 C. P. Raptopoulou, *Materials (Basel).*, 2021, 14, 1–32.

55 C. Dey, T. Kundu, B. P. Biswal, A. Mallick and R. Banerjee, *Cryst. Eng. Mater.*, 2014, **70**, 3–10.

56 S. Mandal, S. Natarajan, P. Mani and A. Pankajakshan, *Adv. Funct. Mater.*, 2021, **31**, 1–22.

57 J. L. Segura, S. Royuela and M. Mar Ramos, *Chem. Soc. Rev.*, 2019, **48**, 3903–3945.

58 G. Anusha, Adsorption; Shodhganga: Ahmedabad, India, 2013, 25.

59 N. Ayawei, A. N. Ebelegi and D. Wankasi, *J. Chem.*, 2017, **11**, 303–817.

60 S. Brunauer, L. S. Deming, W.E. Deming and E.Teller,*J. Chem. Soc.*, 1940, **62**, 1723–1732.

61 C. D. Smedt, F. Ferrer, K. Leus and P. Spanoghe, *Adsorpt. Sci. Technol.*, 2015, **33**, 462.

62 O. Mansour, G. Kawas, M. A. Rasheed and A. A. Sakur, *Res. J. Pharm. Technol.*, 2018, **11**, 8–11.

63 A.U. Cjaza, N. Trukhan, U. Muller, *Chem. Soc. Rev.*, 2009, **38**, 1284–1293.

64 N. L. Rosi, M. Eddaoudi, J. Kim, M. O’Keeffe and O. M. Yaghi, *CrystEngComm*, 2002, **4**, 401–404.

65 V. Guiller, D. Kim, J. F. Eubank, R. Luebke, X. Liu, K. Adil, M. S. Lah and M. Eddaoudi, *Chem. Soc. Rev.*, 2014, **43**, 6141–6172.

66 H. Furukawa, K. E. Cordova, M. O. Keeffe and O. M. Yaghi, *Sciences (New. York).*, 2013, **341**, 123.

67 J.Y. Ying and C. Wang, J. Mater. Chem., 1999, **11**, 3113–3120.

68 J. Ren , N.M. Musyoka, and H.W. Langmi, *Chem. Soc. Rev.*, 2016, **12**, 163–188.

69 S. Thomas, and M. Zalbowitz, *Chem. Sci.*, 2000, **33**, 12–17.

70 H. Audus, O. Kaarstal and O.M. Kowal., *Nature*, 1997, **38**, 431–436.

71 N. L. Garland, D. C. Papageorgopoulos and J. M. Stanford, *Energy Procedia*, 2012, **28**, 2–11.

72 P. P. Edwards, V. L. Kuznetsov and W. I. F. David, *Philos. Trans. R. Soc. A Math. Phys. Eng. Sci.*, 2007, **365**, 1043–1056.

73 J. L. C. Rowsell and O.M. Yaghi , *Angew Chem. Int. Educ.*, 2005, **44**, 4670–4679.

74 A. W. C. van den Berg and C. O, Areán, *Chem. Commun.*, 2008, **1**, 668–681.

75 A.R. K. Rajesh, and R. Xinglian, *Chem. Soc. Rev.*, 2004, **130**, 192–201.

76 Z. Linjian, A. Garg and A. Jain., *Earth Environ. Sci.*, 2018, **108**, 042104

77 M. Arjmandi, M. Pakizeh, M. Saghi and A. Arjmandi, *Chem. Eng. J.*, 2018, **58**, 317–329.

78 S. Ashtiani, Z. Sofer and K. Friess, in *Metal-Organic Frameworks (MOFs): Chemistry, Applications and Performance*, 2021, pp. 157–174.

79 K. Lin, K. Lin, A. K. Adhikari, C. Ku, C. Chiang and H. Kuo, *Int. J. Hydrogen Energy*, 2012, **37**, 13865–13871.

80 T. Yildirim, *J. Am. Chem. Soc.*, 2013, **135**, 11887–11894.

81 Y. Peng, V. Krungleviciute, I. Eryazici, J. T. Hupp, O. K. Farha and T. Yildirim, *J. Am. Chem. Soc.*, 2013, **135**, 11887–11894.

82 S. Ma, D. Sun, J.M. Simmons, C.D. Collier, D. Yuan and H.C. Zhou, *J. Am. Chem. Soc.*, 2008, **130**, 1012–1016.

83 L. Schlapbach, and M. Bull*., Nat. Rev. Chem.*, 2005, **34**, 621–629.

84 S. Abouelfadl, *J. Eng. Sci.*, 2012, **40**, 1233–1254.

85 L. A. Ngongeh, I. K. Idika and A. R. Ibrahim Shehu, *Open Parasitol. J.*, 2014, **5**, 1–11.

86 R. Aniruddha, I. Sreedhar and B. M. Reddy, *J. CO2 Util.*, 2020, **42**, 101297.

87 W. D. Jones, *J. Am. Chem. Soc.*, 2020, **142**, 4955–4957.

88 R. Tang, J. Xu, B. Zhang, J. Liu, C. Liang and J. Hua. *Nat Commun*, 2017, **8,** 123

CHAPTER 2

EXPERIMENTAL

This chapter discusses the synthesis and characterization of three pyridyl ligands and one carboxylate ligand. The synthesis of MOFs is also discussed in detail. The instrumentation used to characterize the ligands and the MOFs as well as the computer programmes used to analyse the MOFs are also discussed. Crystallographic data are given on page 23.

2.1. Synthesis and characterization of organic ligands

Four (4) ligands namely *N,N′*–bis–(3-pyridylmethyl)–benzophone diimide **(L1)**, *N,N′*–bis–(3-pyridylmethyl)–biphenyl diimide **(L2)**, *N,N*–bis(pyridin-4-ylmethyl) –naphthalene diimide, *N,N′*–bis–(3-pyridylmethy)–biphenyl diimide **(L3)** and *N,N′*–bis(gly)–biphenyl diimide **(L4)** were successfully synthesized.

2.1.1. Synthesis of N,N′–bis–(3-pyridylmethyl)–benzophone diimide (L1)

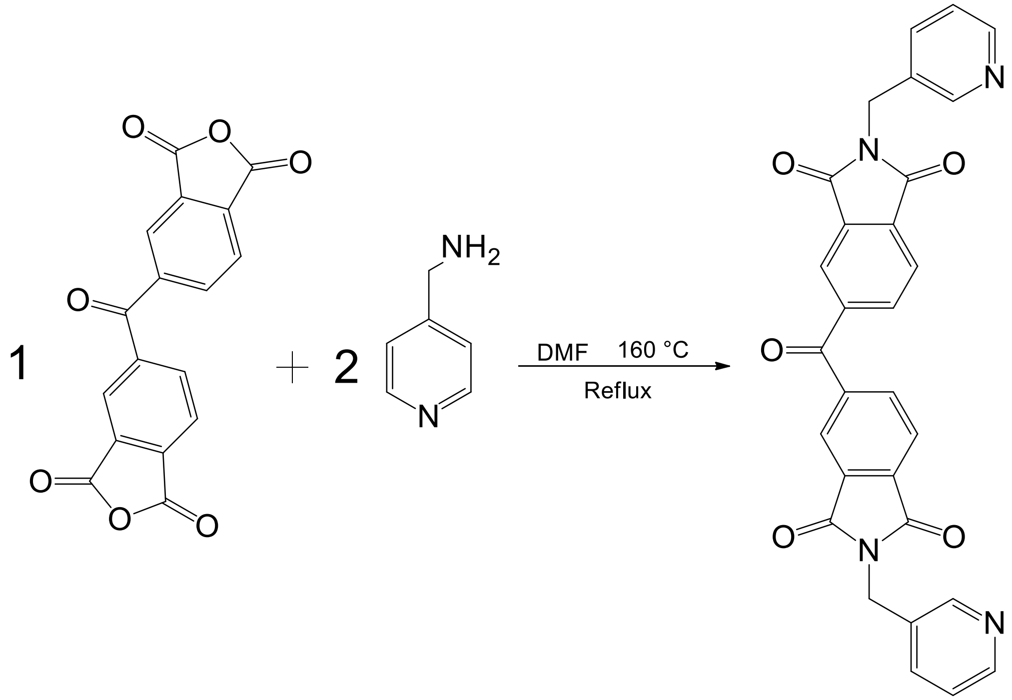

Scheme 2.1 The synthesis of *N,N'*-bis-(3-pyridylmethyl)-benzophone diimide **(L1).**

L1 was synthesized by refluxing a mixture of benzophenone-3,3′,4,4′-tetracarboxylic dianhydride (1 g, 3.10 mmol) and 3-aminomethyl pyridine (0.67 g, 6.21 mmol) in DMF (20 mL) for 24 hours at 160 °C. The yellow solution was filtered, and the crude solid was collected and recrystallized from DMF. Yield 71%, melting point (Mp) 267 ºC. FTIR-ATR: ν_{max}: 3478 cm^{-1} (N-H stretch) 3025 cm^{-1} (C–H stretch) 1769 cm^{-1} (C=O stretch), 716 cm^{-1}, 696 cm^{-1} (C–H bend. FTIR spectrum of **L1** is shown in Figure 2.1. ^{1}H-NMR (DMSO-d_6, 400 MHz): δ 8.613 (s, H_{py}, 2H), δ 8.503 (s, H_{py}, 2H), δ 8.199 (d, H_{Ar}, 2H), δ 8.107 (m, H_{Ar}, 4H), δ 7.776 (d, H_{py}, 2H), δ 7.393 (t, H_{py}, 2H), δ 4.862 (s, CH_2, 4H). ^{13}C-NMR ($CDCl_3$, 100 MHz): δ 193.89 (C), δ 167.40 (C×4), δ 162.76 (C×2), δ 149.44 (CH×2), δ 149.21 (CH×2), δ 141.94 (C×2), δ 136.17 (CH×2), δ 135.92 (CH×2), δ 135.30 (C×2), δ 132.54 (C×2), δ 132.46 (C×2), δ 124.19 (CH×2), δ 124.14 (CH×2), δ 39.81 (CH_2×2). Proton, carbon and DEPT-135 NMR spectra are shown in Figures 2.2, 2.3 and 2.4 respectively.

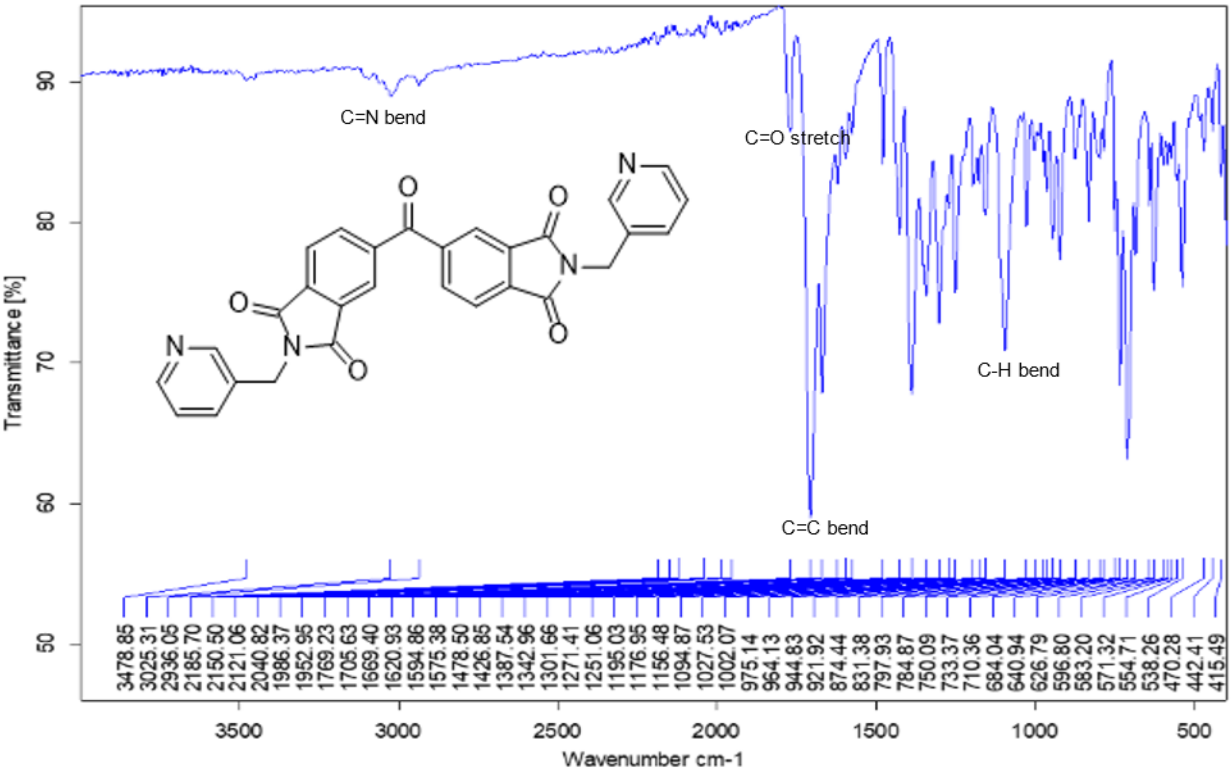

Figure 2.1 FTIR spectrum of **L1.**

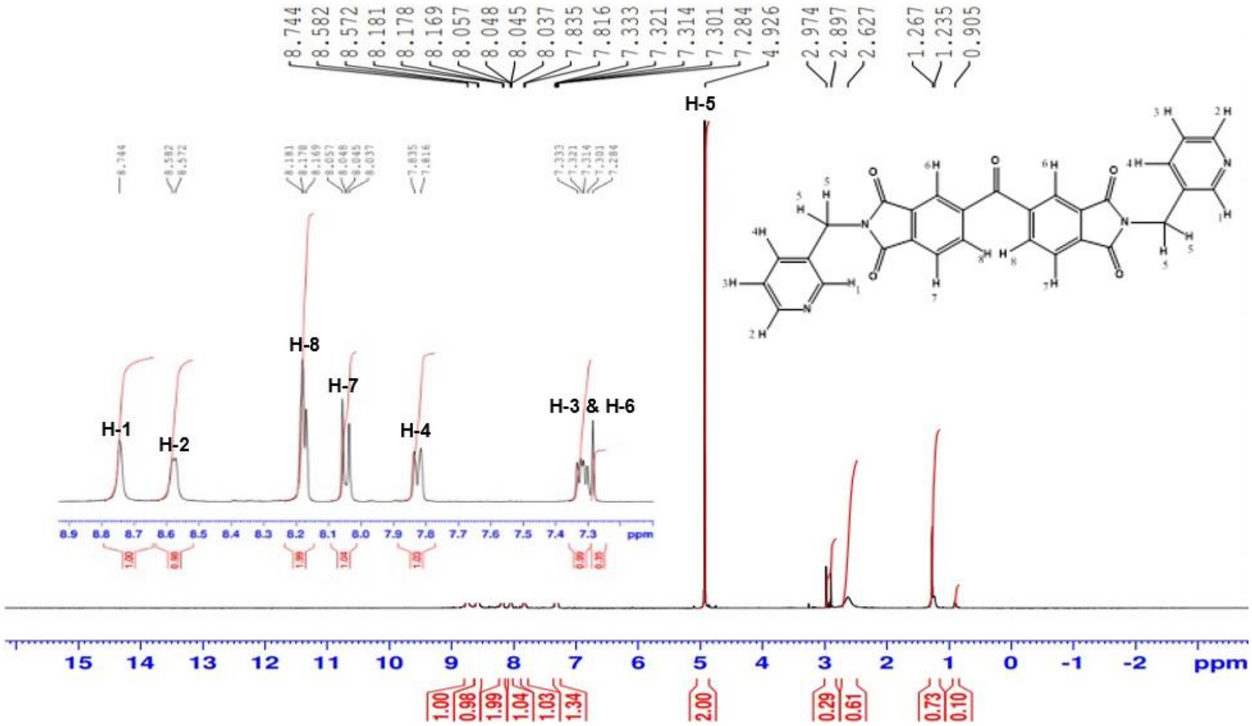

Figure 2.2 ^{1}H NMR spectrum of **L1**.

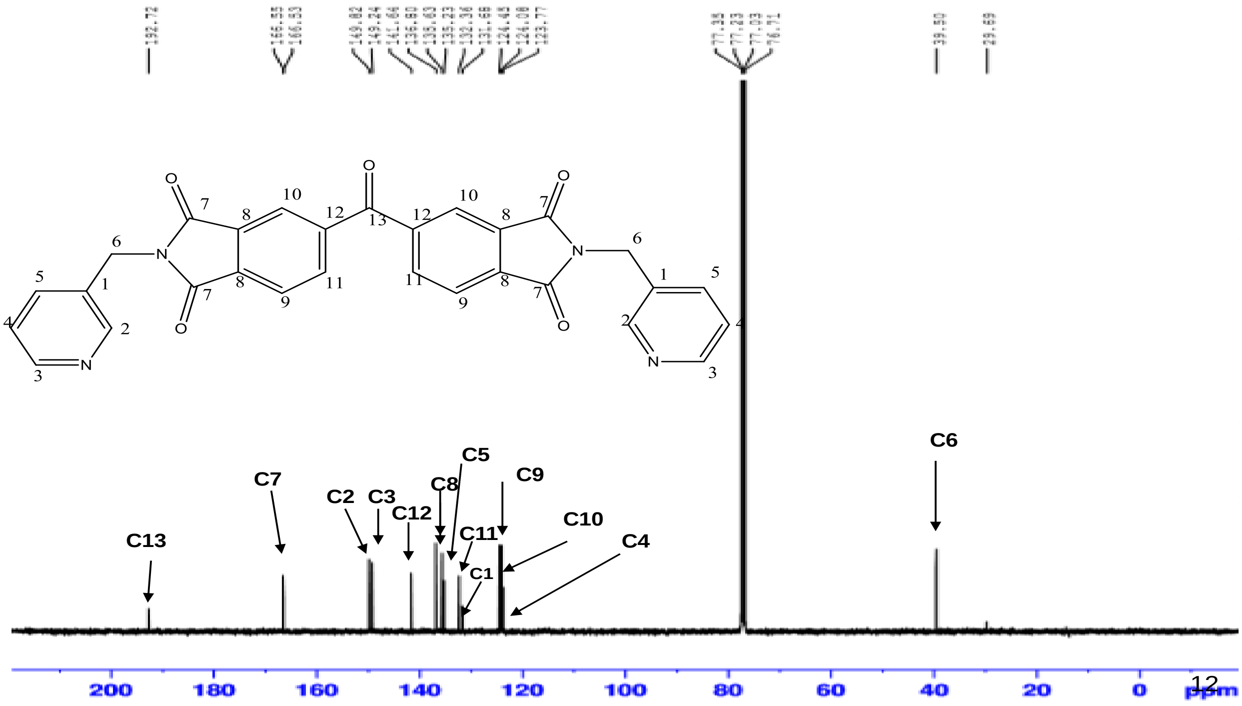

Figure 2.3 ^{13}C NMR spectrum of **L1.**

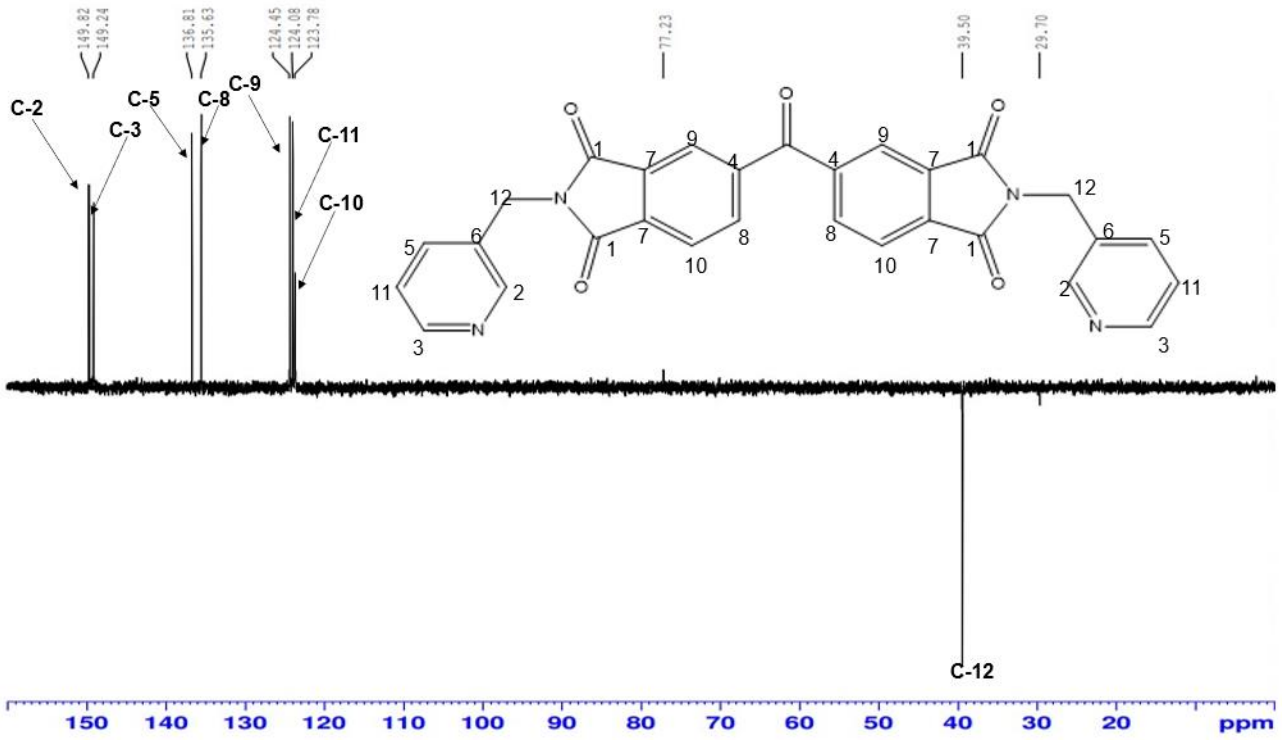

Figure 2.4 DEPT-135 spectrum of **L1.**

2.1.1.1. Crystallization of L1

Single crystal X-ray diffraction (SCXRD)

Molecular formula: $C_{29}H_{19}N_4O_5$

Formula weight: 502.47 g.mol^{-1}

a = 5.9017 (2) Å	α =100.5080(1)°	Space Group: *P*1
b = 10.9547 (4) Å	β = 90.0040 (1)°	*Z* = 2
c = 18.5087 (6) Å	γ =102.7740(1)°	*V* = 1146.41(7) Å^3

L1 crystallizes in the triclinic space group *P*1 with one complete **L1** molecule in the asymmetric unit (Figure 2.5). The molecules are stacked in a herringbone fashion and interact *via* C-H···O (2.421 Å), C=O···H (2.241 Å) as well as edge-to-face interactions (3.232 Å). The packing diagram of **L1** viewed onto the ab plane is shown in Figure 2.6.

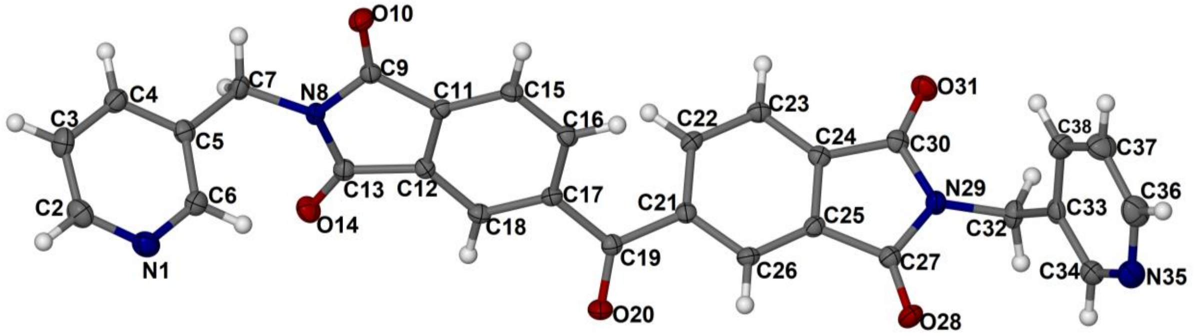

Figure 2.5 The asymmetric unit of **L1** showing the crystallographic labelling scheme. Ellipsoids are shown at the 70% probability level.

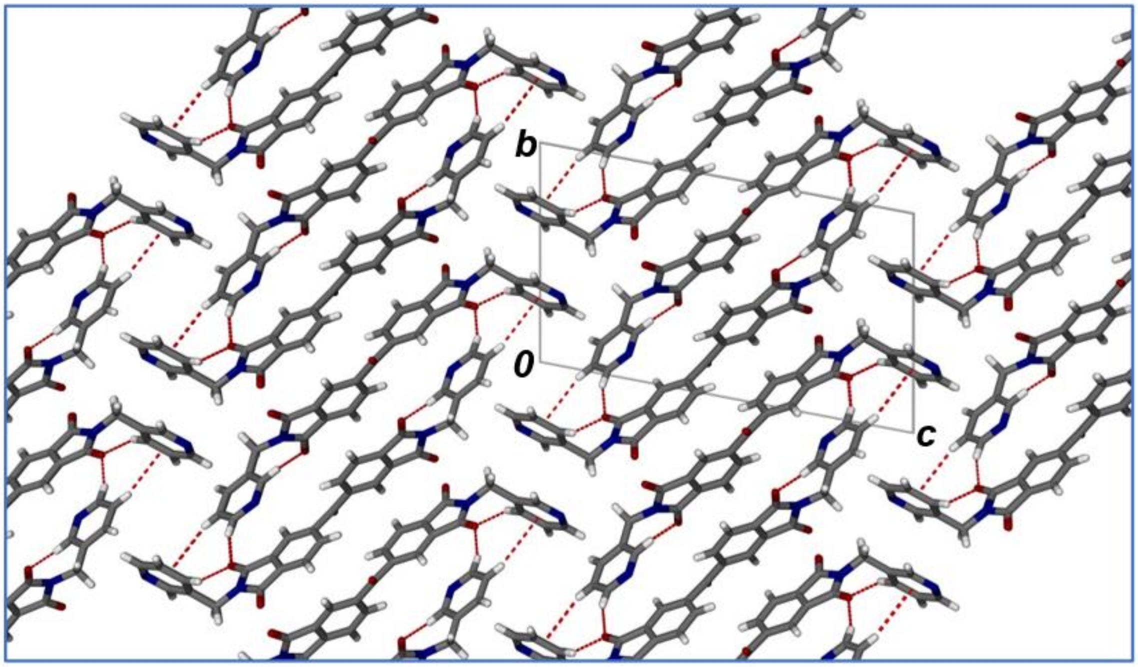

Figure 2.6 The packing diagram of **L1** viewed onto the *ab* plane.

2.1.2. Synthesis of N,N'–bis–(3-pyridylmethyl)–biphenyl diimide (L2)

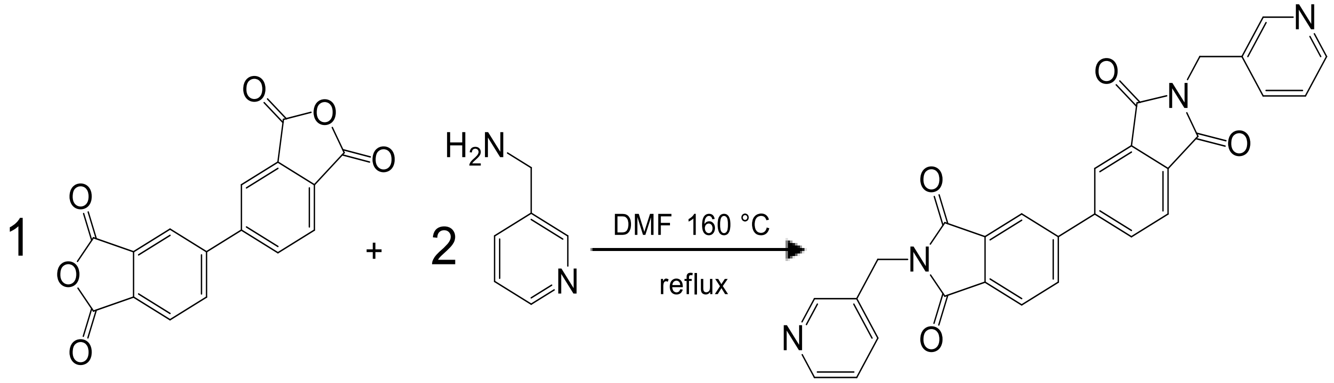

Scheme 2.2. Synthesis of *N,N′*-bis(4-pyridylmethyl)-benzophenone diimide **(L2)**.

3,3′,4,4′-Biphenyltetracarboxylic dianhydride (2.00 g, 6.79 mmol) and 3-(amino) methyl pyridine (1.52 g, 13.98 mmol) were mixed in a quick-fit one-necked round-bottomed flask and dissolved in 20 mL DMF with stirring under reflux conditions (24 h, 160 ºC) (see Scheme 2.2). The mixture was allowed to cool, followed by the filtration and collection of the crude solid which was then recrystallized from DMF. The product was air-dried yielding a white shiny powder. Yield 95%, Mp 297 ºC. FTIR-ATR: Vmax: 2925 cm^{-1} (C=N bend) 1763 cm^{-1} (C=O stretch) 1605 cm^{-1} (C-C bend), 716 cm^{-1}, 696 cm^{-1} (C–H out-of-plane bend) (Figure 2.7). The ^{1}H NMR, ^{13}C NMR and DEPT-135 NMR spectra are shown in Figures 2.8, 2.9 and 2.10 respectively. ^{1}H NMR (400 MHz, $CDCl_3$) δ 8.67 (s, 1H), 8.49 (d, *J* = 4.0 Hz, 1H), 8.04 (s, 1H), 7.92 (s, 2H), 7.92 (s, 2H), 7.75 (d, *J* = 7.9 Hz, 1H), 4.84 (s, 2H). ^{13}C NMR (101 MHz, $CDCl_3$) δ 206.84 (C) , 167.15 (CH×2), 149.87 (CH×2), 149.18 (C×2), 145.22 (CH×2), 136.60 (C×2), 131.87 (C×4), 131.74 (CH×2), 124.35 (CH×2), 123.63 (CH_2×2), 122.31 (CH×2) , 39.30 (CH×2)

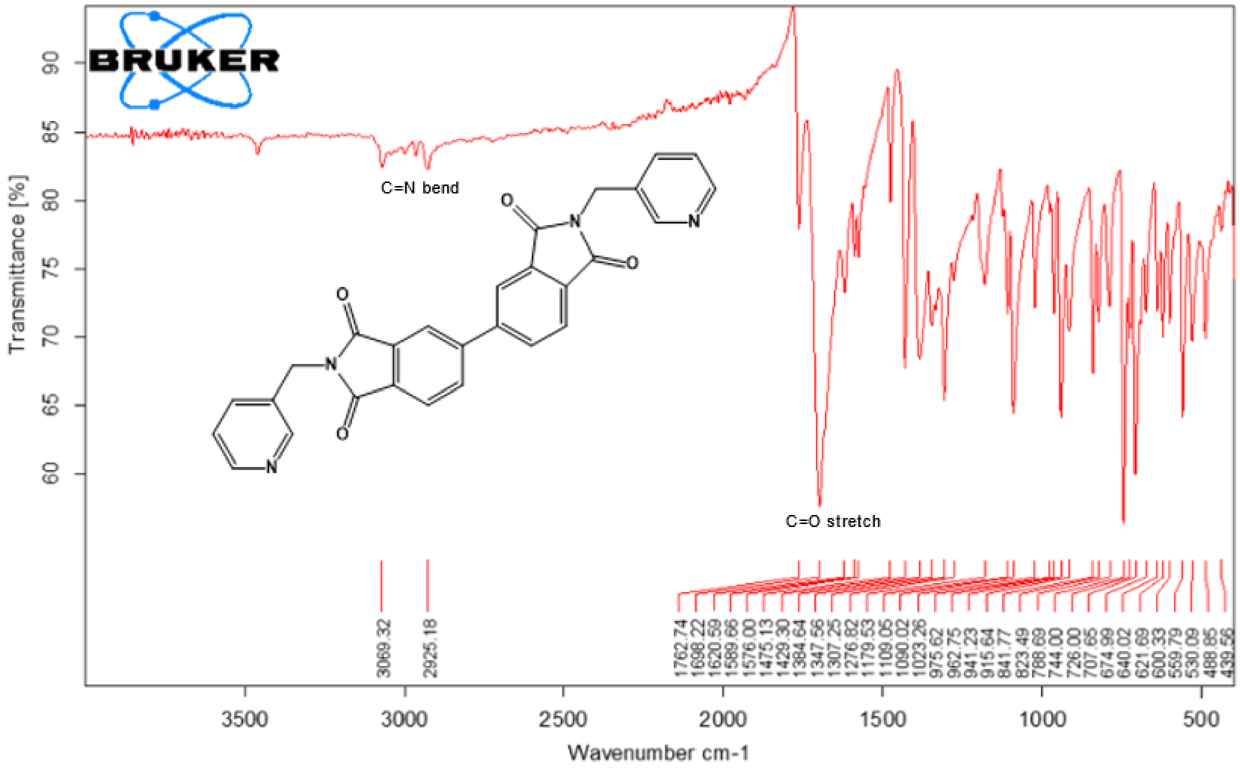

Figure 2.7 FTIR spectrum of **L2.**

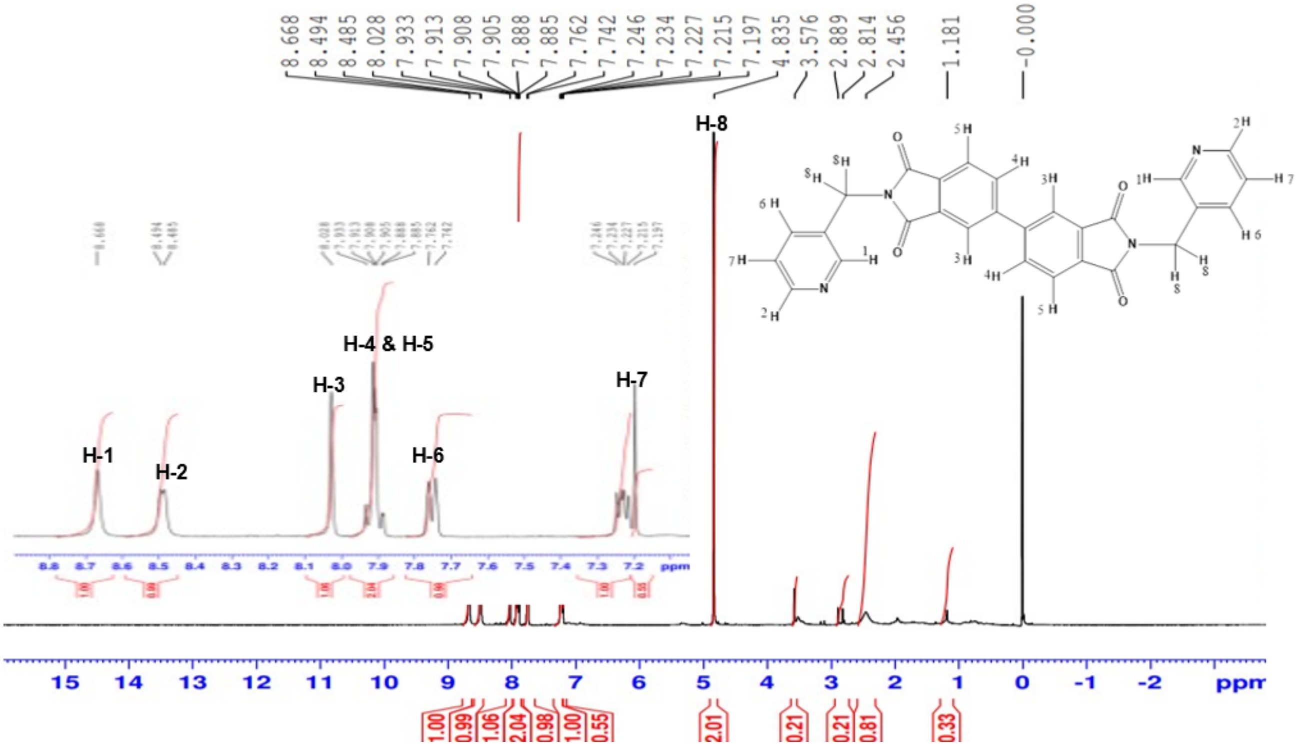

Figure 2.8 ^{1}H NMR spectrum of **L2.**

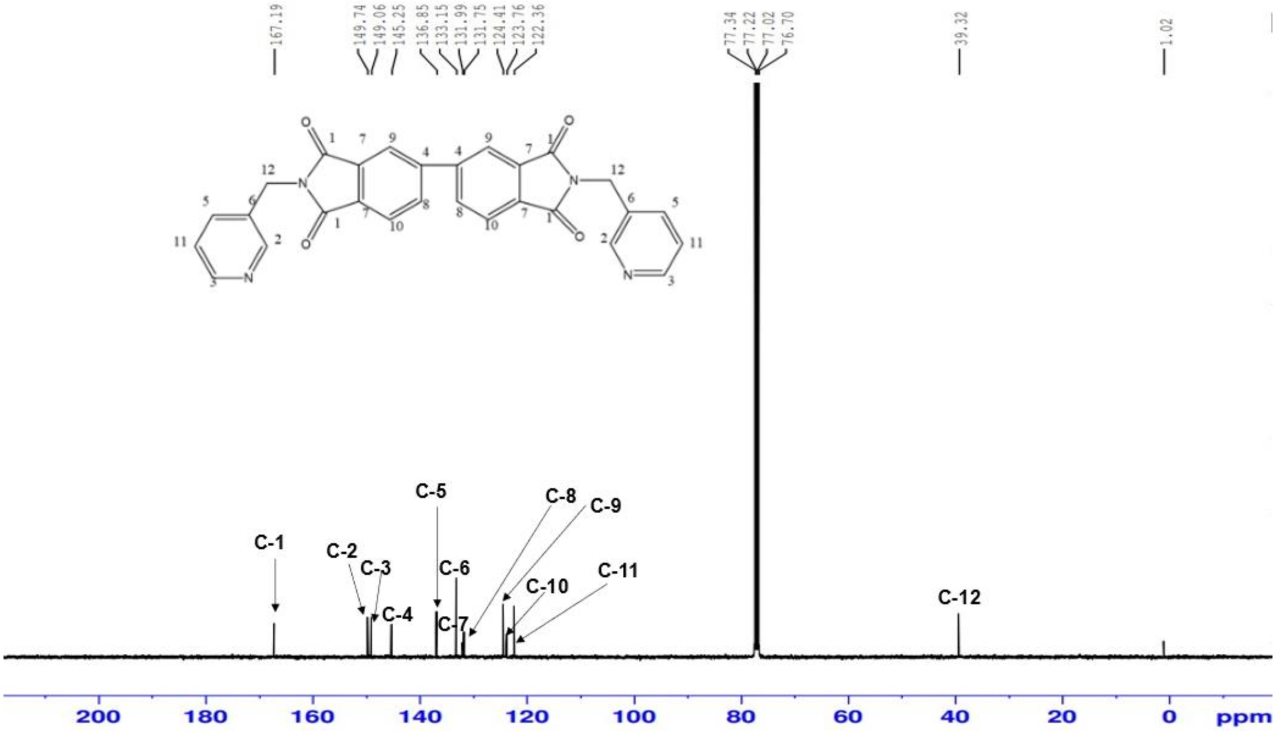

Figure 2.9 ^{13}C NMR spectrum of **L2.**

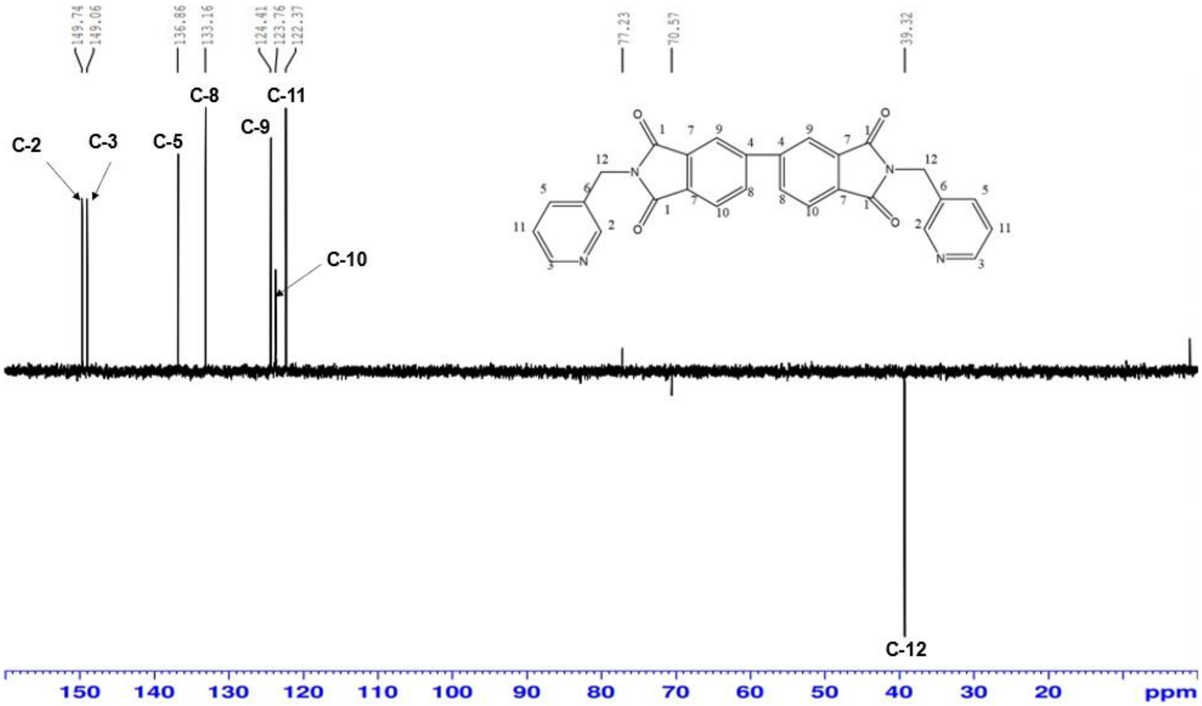

Figure 2.10 DEPT-135 spectrum of **L2.**

2.1.3. Synthesis of *N*,*N'*-bis(pyridin-4-ylmethyl) naphthalene diimide (L3)

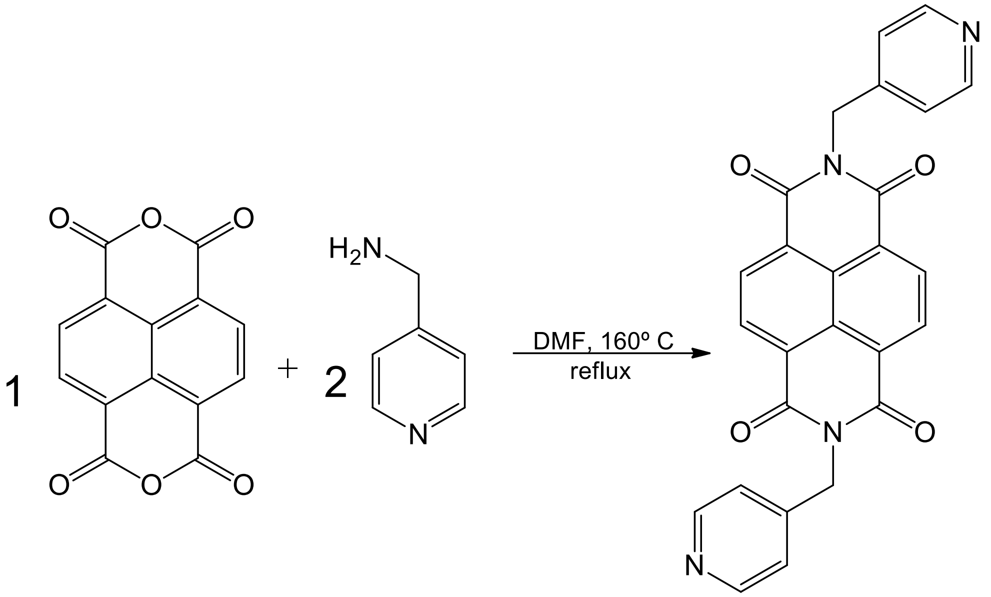

Scheme 2.3 Synthesis of *N*,*N*-bis (pyridiyl-4-methyl) naphthalene diimide **(L3).**

L3 was synthesized by refluxing a mixture of 1, 4, 5, 8-napthalenetetracarboxylic dianhydride (1.0 g, 3.73 mmol) and 4-(aminomethyl) pyridine (1.0 g, 7.46 mmol) in DMF (30 mL) for 12 hours at 160 °C. The mixture was allowed to cool, followed by the filtration and collection of the crude solid which was then recrystallized from DMF. The product was air-dried yielding a brown powder. Yield 85%, Mp 302 ºC. FTIR-ATR: vmax: 3037 cm^{-1} (C–H bonded) 1760 cm^{-1} (C=O stretch) 1701 cm^{-1} (C=O bend) 1605 cm^{-1} (C-C bend), 716 cm^{-1}, 696 cm^{-1} (C–H out-of-plane (oop) bend) (Figure 2.11). The ^{1}H NMR, ^{13}C NMR and DEPT-135 NMR spectra are shown in Figures 2.12, 2.13 and 2.14, respectively. ^{1}H NMR (400 MHz, DMSO) δ 8.74 (s, 1H), 8.50 (d, *J* = 5.8 Hz, 1H), 7.41 (d, *J* = 5.9 Hz, 1H), 5.31 (s, 1H). ^{13}C-NMR ($CDCl_3$, 100 MHz): δ 162.66 (C×4), δ150.03 (C×4), δ 145.17 (C×2), δ 131.50 (CH×4), δ 126.87 (C×4), δ 126.55 (C×2), δ 123.51(CH×4), δ 43.08 (CH_2×2).

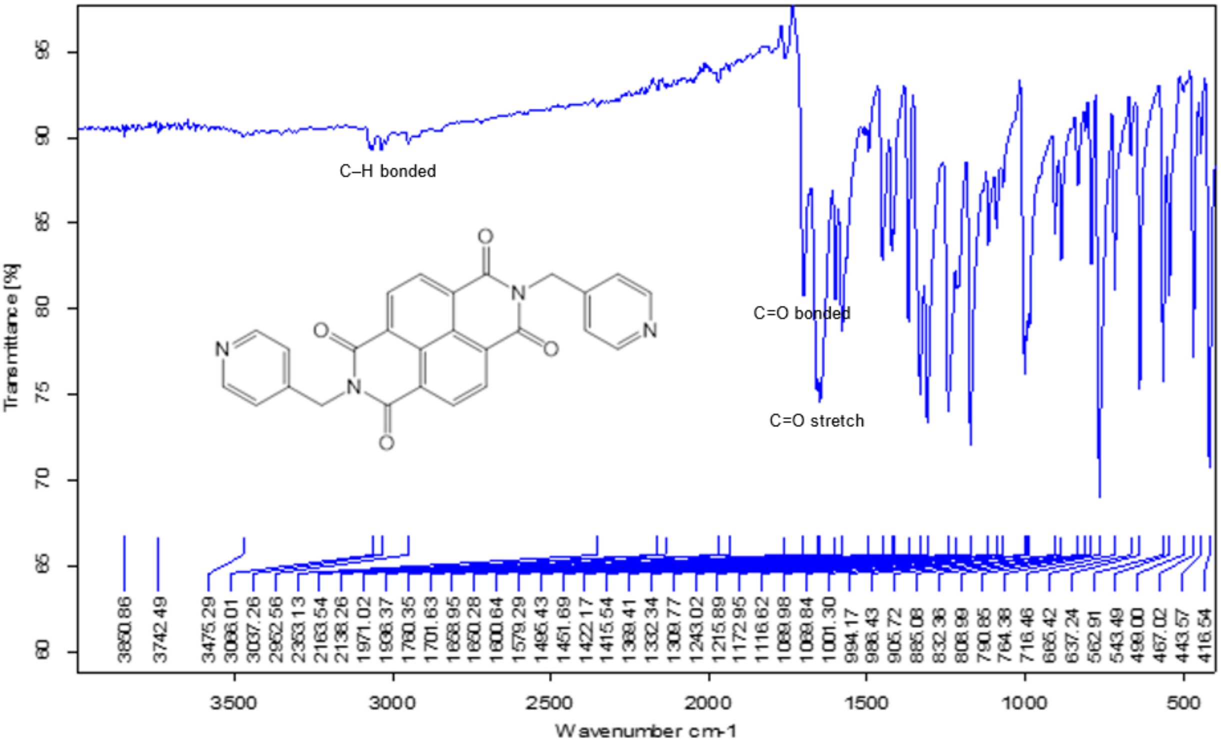

Figure 2.11 FTIR spectrum of **L3.**

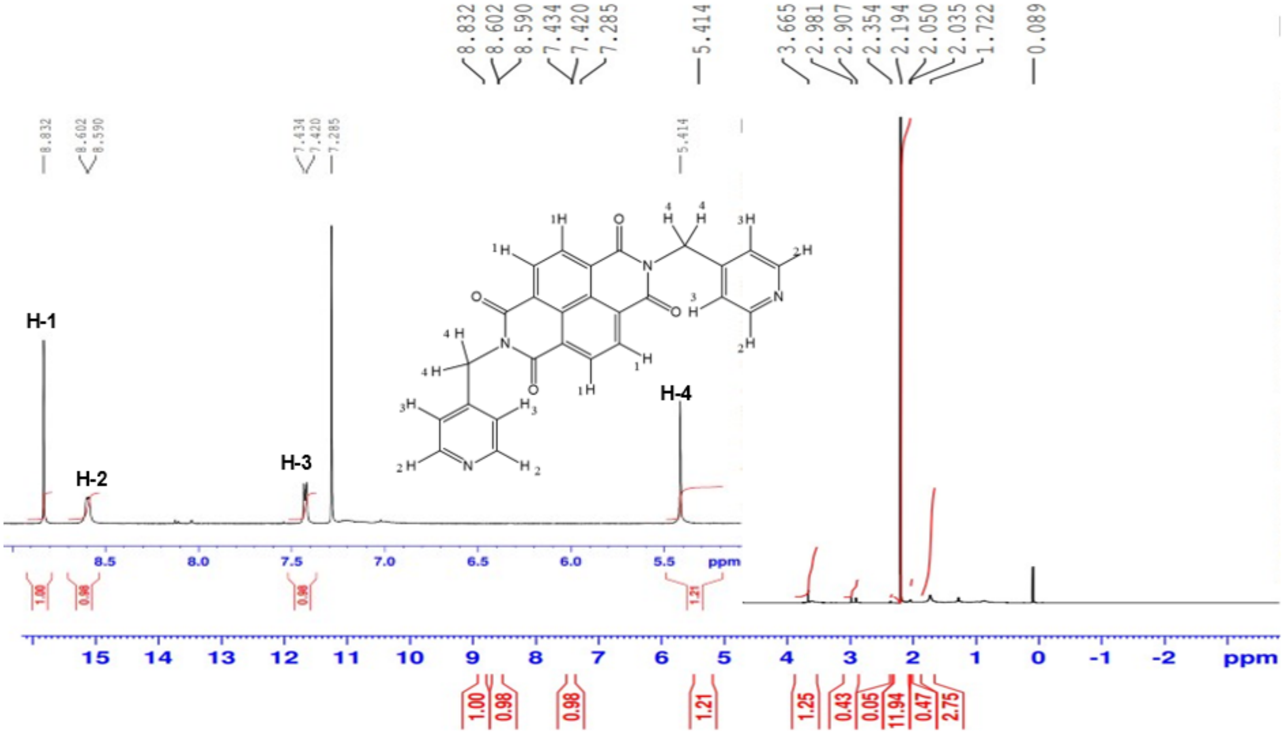

Figure 2.12 ^{1}H NMR spectrum of **L3.**

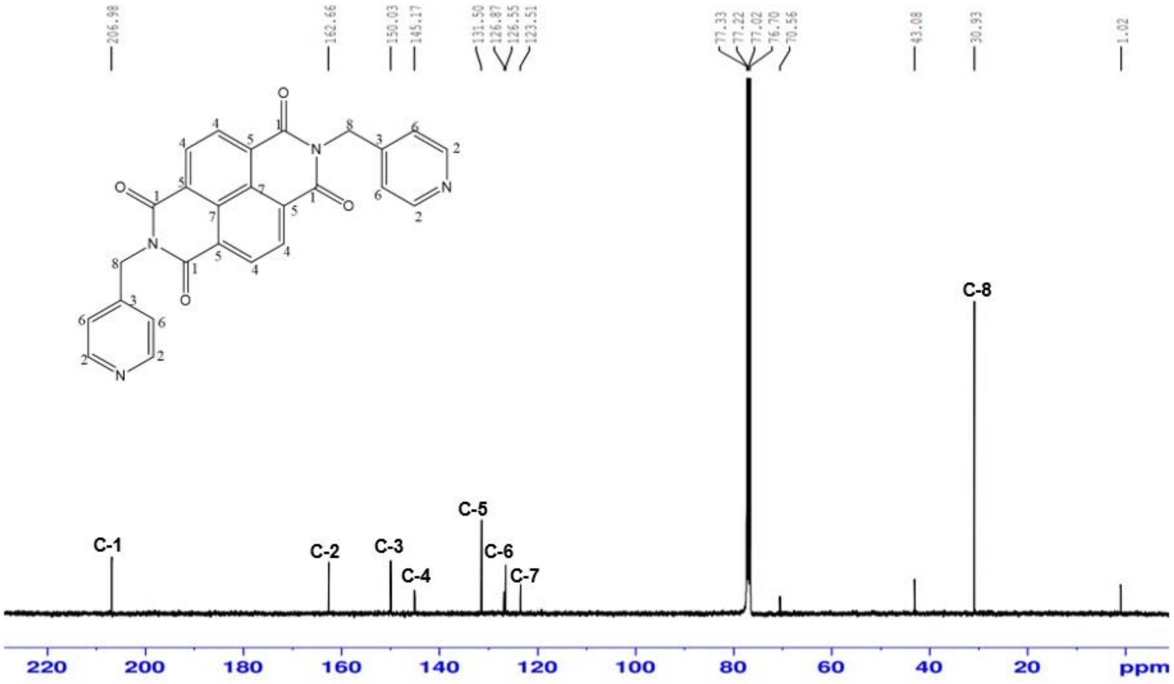

Figure 2.13 ^{13}C NMR spectrum of **L3.**

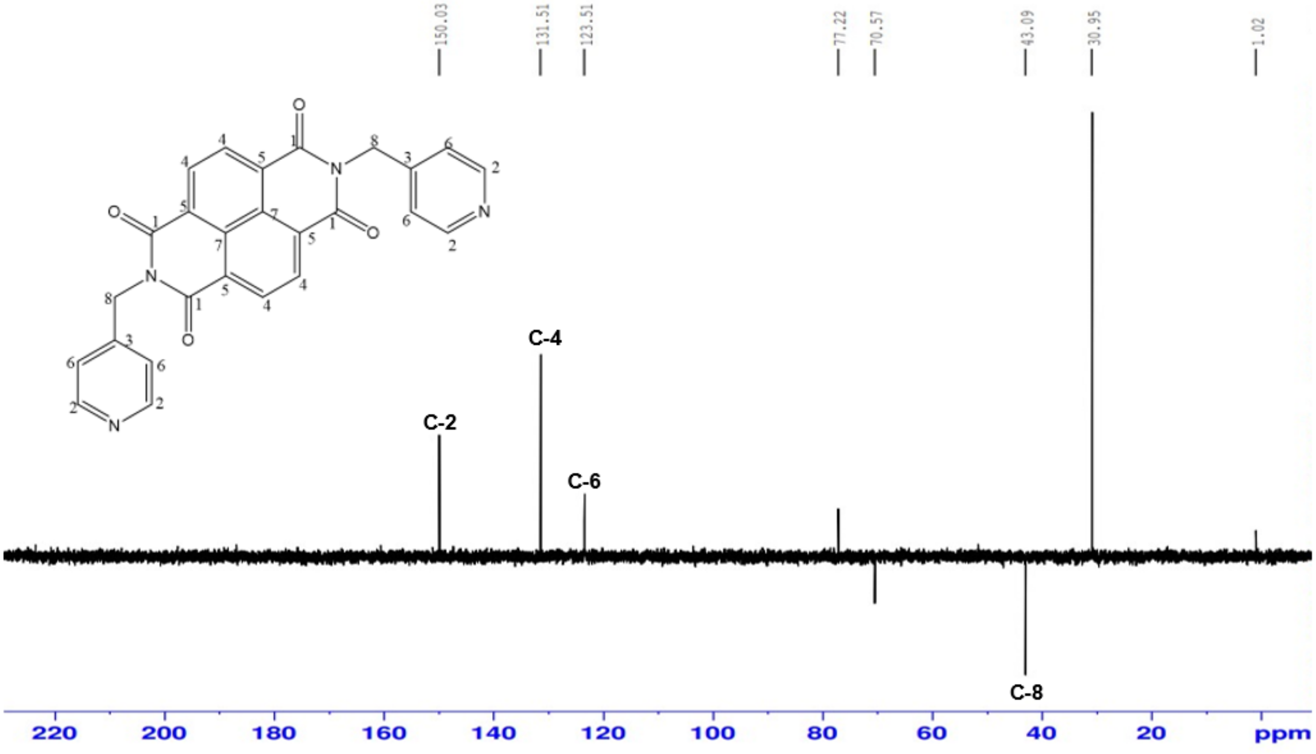

Figure 2.14 DEPT-135 NMR spectrum of **L3.**

2.1.4. Synthesis of *N,N'-bis*(glycinyl)-biphenyl diimide (L4)

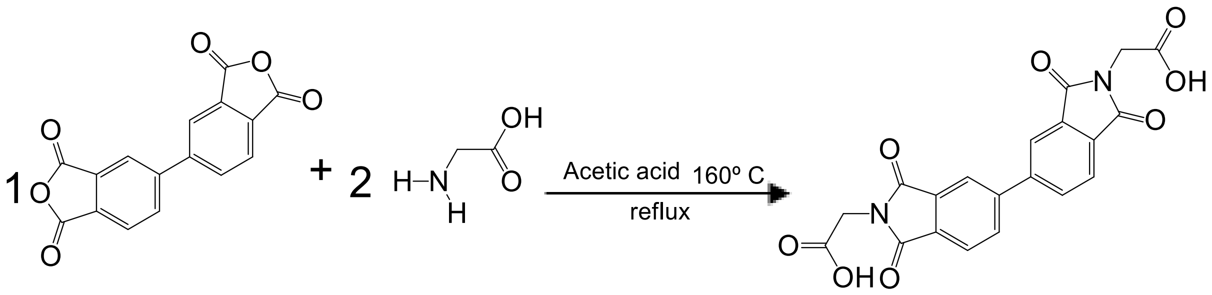

Scheme 2.4 Synthesis of *N,N′-bis*(glycinly)- biphenyl diimide (**L4**).

3,3′,4,4′-Biphenyltetracarboxylic dianhydride (1.00g, 3.40 mmol) and glycine (0.51 g, 6.67 mmol) were mixed in a quick-fit one-necked round-bottomed flask and dissolved in 20 mL DMF with stirring under reflux conditions (24 h, 160 ºC). The mixture was allowed to cool, followed by filtration. The crude solid was then recrystallized from DMF. The ligand was characterized using FTIR and NMR. Yield 80%, Mp 267 ºC. FTIR-ATR: vmax: 3082 cm^{-1} (O–H stretch), 1710 cm^{-1} (C=O stretch), 1478 cm^{-1} (C–C stretch), 716 cm^{-1}, 696 cm^{-1} (C–H bend) (Figure 2.15). The ^{1}H NMR, ^{13}C NMR and DEPT-135 NMR spectra are shown in Figure 2.16, 2.17 and 2.18, respectively ^{1}H NMR (400 MHz, DMSO) δ13.29 (s, 1H) 8.40 (s, 1H), 8.35 (d, *J* = 9.0 Hz, 1H), 8.07 (d, *J* = 7.8 Hz, 1H), 4.37 (s, 1H) (Figure 2.16) ^{13}C NMR (101 MHz, DMSO) δ 168.83(Cx2), 167.10 (Cx4), 144.44 (Cx2), 134.36 (Cx4), 131.48(CHx2), 124.34(CHx2), 123.20 (CHx2), 41,5 (CH_2x2).

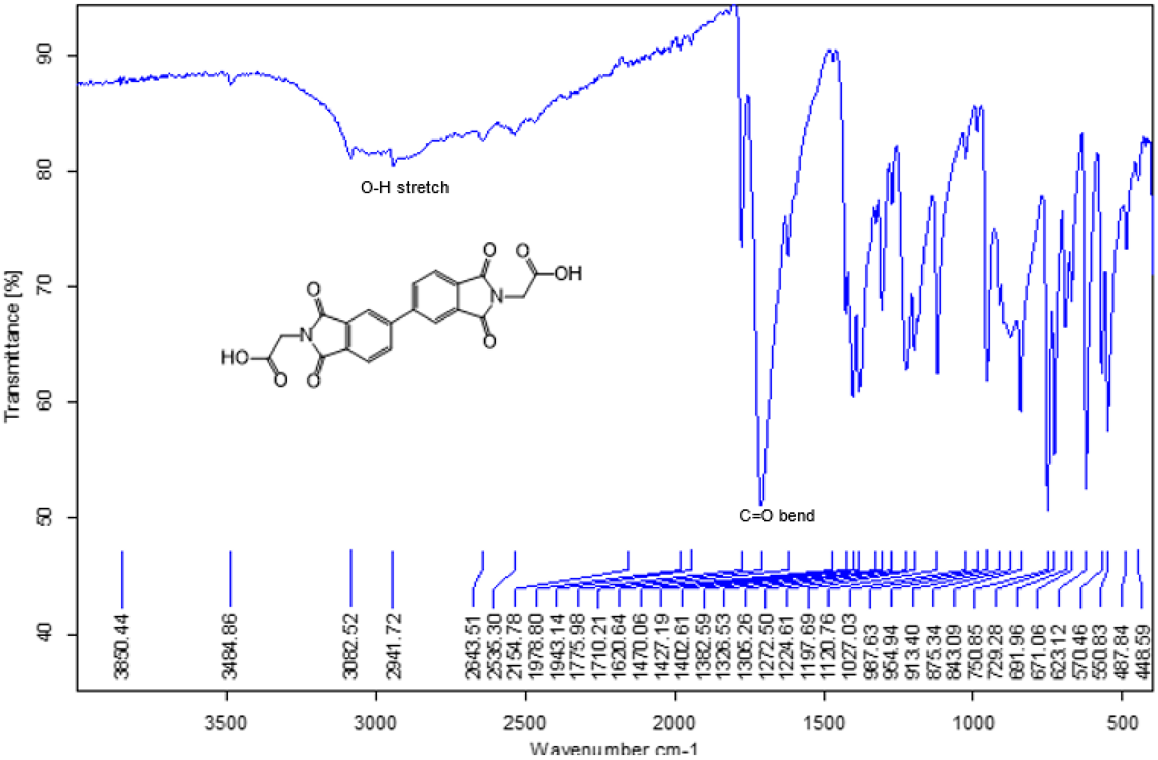

Figure 2.15 FTIR spectrum of **L4.**

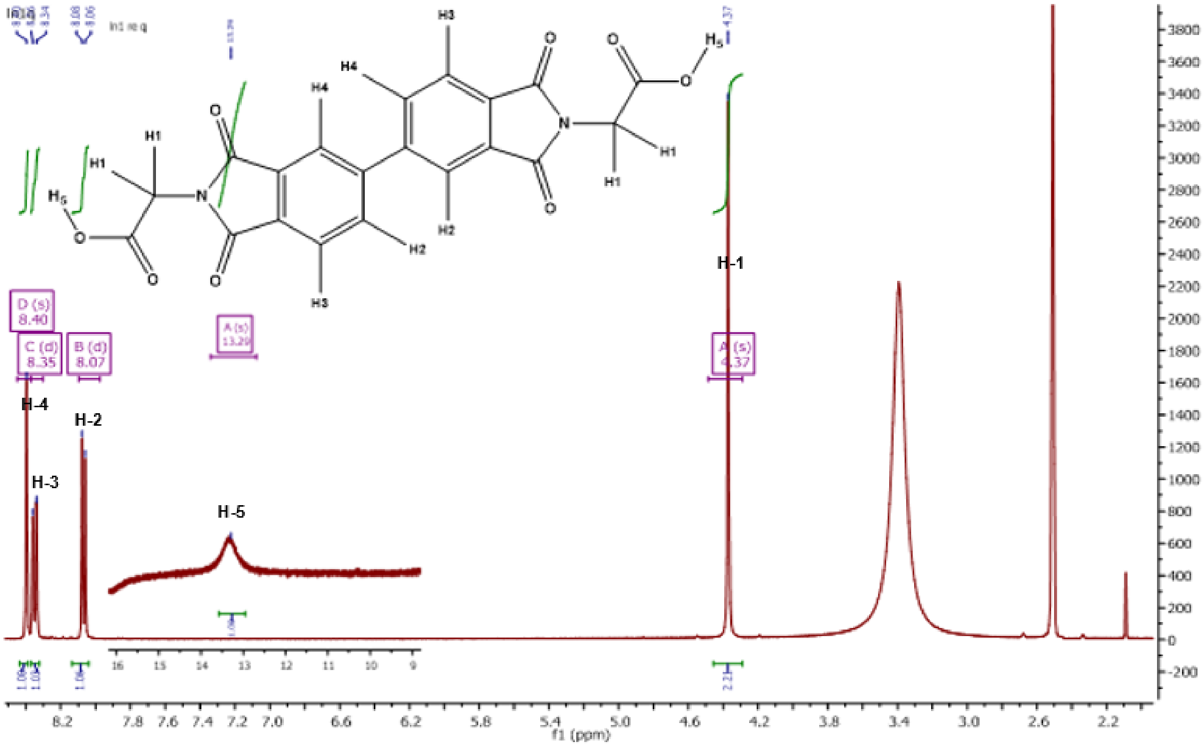

Figure 2.16 ^{1}H NMR spectrum of **L4.**

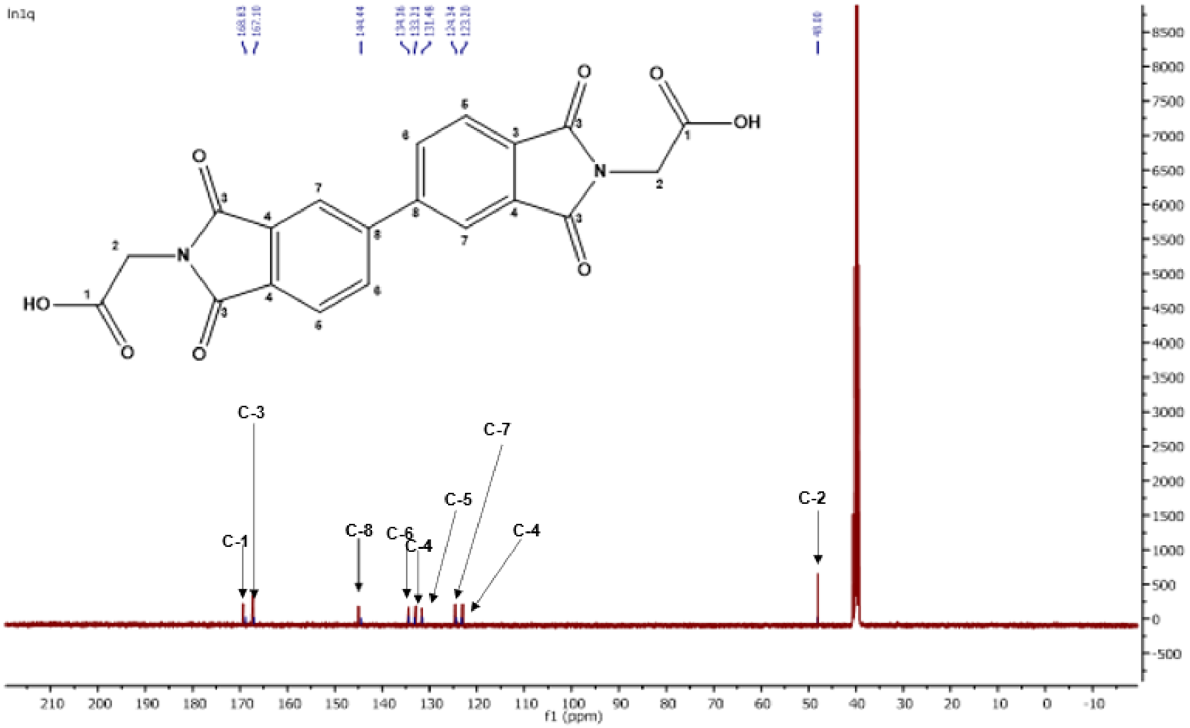

Figure 2.17 ^{13}C NMR spectrum of **L4.**

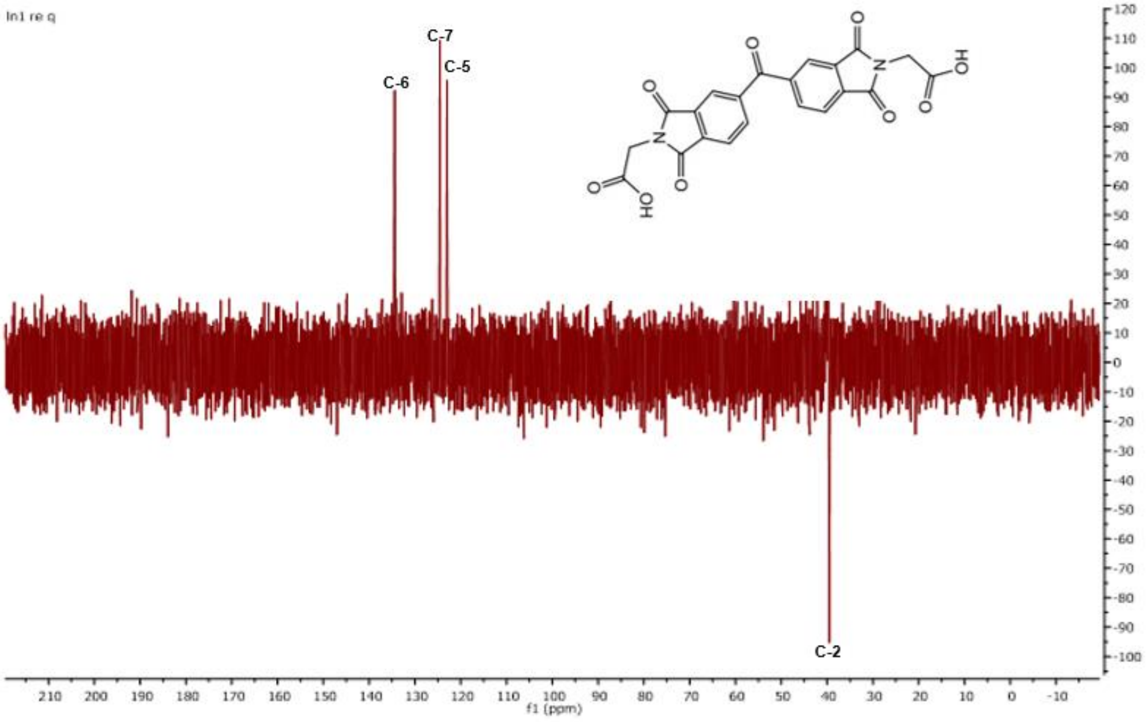

Figure 2.18 DEPT-135 NMR spectrum of **L4.**

2.1.4.1. Crystallisation of L4

Single crystal X-ray diffraction (SCXRD)

Crystal data of L4

Molecular formula: $C_{23}H_{17}N_3O_9$

Formula weight: 479.40 g mol^{-1}

a = 31.387 (6) Å	α = 90°	Space group: *Pc*
b = 4.7952 (1) Å	β = 105.976(3) °	Z = 4
c = 17.537 (4) Å	γ = 90°	V = 2537.5 (9) $Å^3$

L4 crystallizes in the monoclinic *Pc* group with two complete **L4** molecules in the asymmetric unit and four DMF molecules. (Figure 2.19. The molecules are stacked in a herringbone fashion. The packing diagram viewed onto the *ac* plane is shown in Figure 2.20

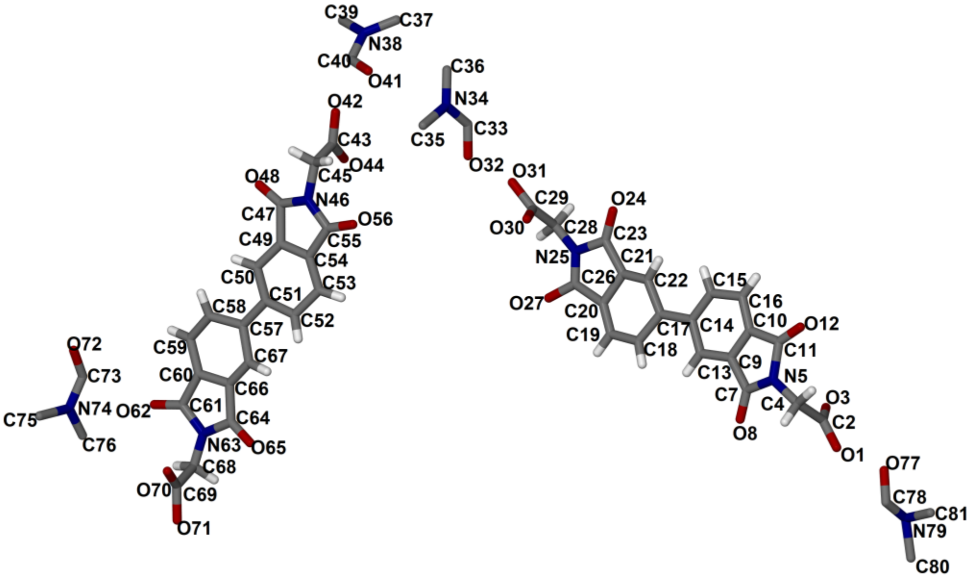

Figure 2.19 The asymmetric unit of **L4** showing the crystallographic labelling scheme. The red, grey, dark blue coloured atoms correspond to oxygen, carbon, and nitrogen atoms, respectively.

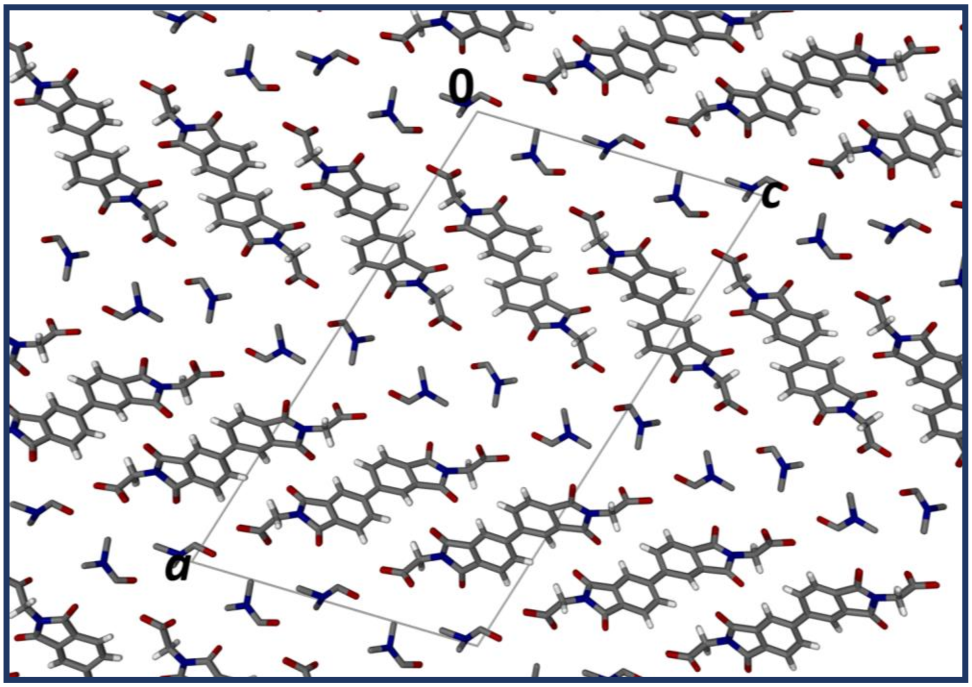

Figure 2.20 The packing diagram of **L4** viewed onto the *ac* plane. The DMF molecules are in channels.

2.2. SYNTHESIS OF MOFs

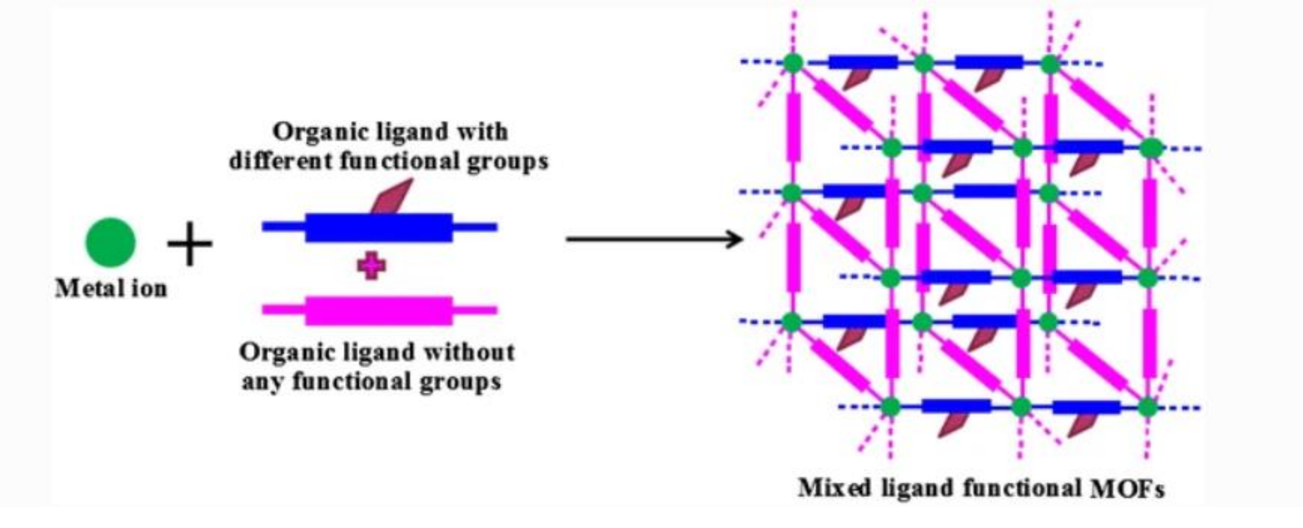

Figure 2.21 Schematic illustration of the synthesis of MOFs using mixed-ligand strategy.[3]

The mixed-ligand strategy was used to synthesize MOFs in this study (Figure 2.21). In the mixed-ligand strategy two organic ligands with different functional groups are used.[1] The mixed-ligand strategy ensures that the coordination requirements of the metal centres are satisfied, resulting in higher dimensional frameworks.[2] In this study, pyridine N-donor ligands and carboxylates ligands were used as the two linkers.

All the MOFs presented in this study were synthesized using the solvothermal method. In general, the ligand, co-ligand and the metal salt were dissolved in a solvent in different vials and mixed or dissolved in a solvent in one vial. The mixture was closed in a vial and heated in an oven at 100 °C. After the formation of crystals, the reaction was stopped and the crystals were washed with the solvent used in the synthetic reaction (Figure 2.22). The crystals were then analyzed using X-ray diffraction (single crystal X-ray diffraction (SCXRD) and powder X-ray diffraction (PXRD)) and thermal analysis using hot stage microscope (HSM) and thermogravimetric analysis (TGA). The MOFs were then assessed for gas sorption capacity. The reactions carried out in the synthesis of MOFs for this study are shown in Table 2.1.

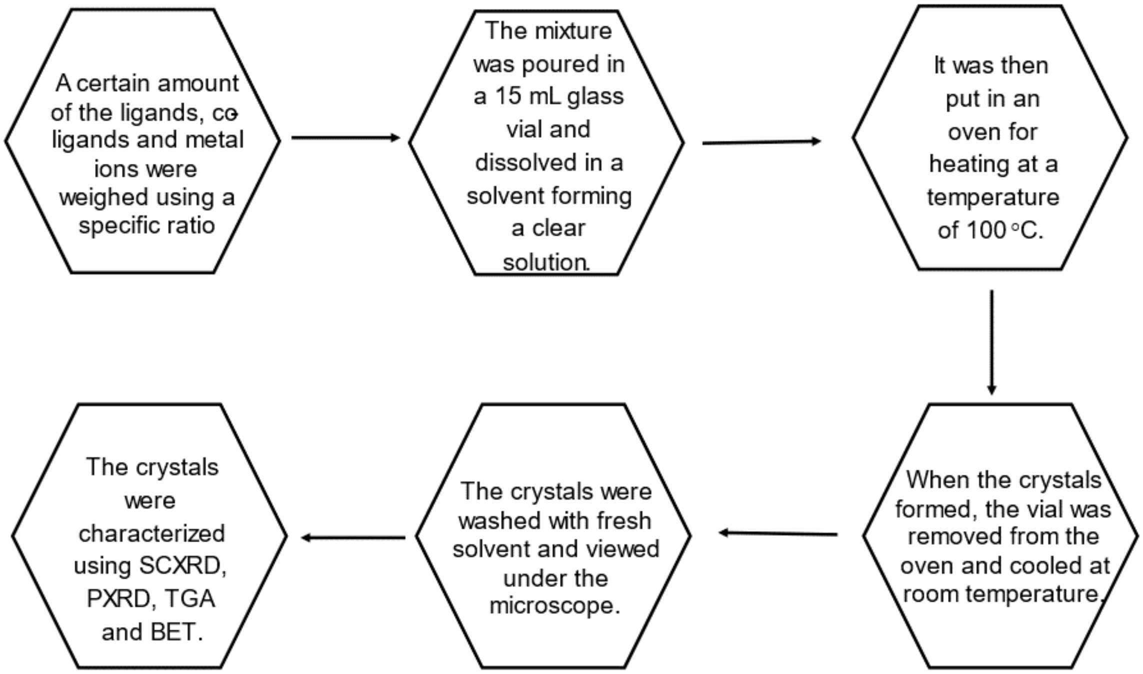

Figure 2.22 A flow chart representing the general synthesis of MOFs.

Table 2. 1 The reactions carried out in the synthesis of MOFs presented in this study

Ligand	**Co-ligand**	**Metal ion** **$M(NO_3)_2XH_2O$**	**Product**	**Structure**
N,N′–bis–(3-pyridylmethy)–benzophone diimide **(L1)**	terephthalic acid	$CoCl_2{\cdot}6H_2O$	Good quality crystals	**LMMOF01**
N,N′–bis –(3-pyridylmethy)–biphenyl diimide **(L2)**	4,4’-oxybis (benzoic acid)	$Zn(NO_3)_2{\cdot}6H_2O$	Good quality crystals	**LMMOF02**
N,N′–bis-(pyridin-4-ylmethyl) naphthalene diimide **(L3)**	terephthalic acid	$Zn(NO_3)_2{\cdot}6H_2O$	Good quality crystals	**LMMOF03**
N,N′–bis-(gly)-biphenyl diimide **(L4)**	2,2-Bipyridyl	$CoCl_2{\cdot}6H_2O$	Good quality crystals	**LMMOF04**
N,N′-bis-(gly)-biphenyl diimide **(L4)**	Phthalic acid	$CuCl_2$	Good quality crystals	**LMMOF05**

2.3. SYNTHESIS OF MOFS PRESENTED IN THE STUDY

2.3.1. Synthesis of LMMOF01

L1 (25 mg, 0.05 mmol), terephthalic acid (17 mg, 0.10 mmol) and $CoCl_2{\cdot}6H_2O$ (24 mg, 0.01 mmol), were mixed in a 15 mL vial and dissolved in 7 mL DMF and 3 mL ethanol (EtOH). The mixture was stirred until the solution was clear and heated in an oven at 100 °C. After 120 hours, purple crystals were formed. The vial was removed from the oven and the crystals were washed using DMF. The crystals were then analysed using SCXRD, PXRD, VT-PXRD, HSM, and TGA and assessed for gas sorption.

2.3.2. Synthesis of LMMOF02

L2 (24 mg, 0.06 mmol)), 4, 4’-oxybis (benzoic acid) (26 mg, 0.10 mmol) and $Zn(NO_3)_2{\cdot}6H_2O$ (30 mg, 0.10 mmol) were mixed in a 15 mL vial in 10 mL DMF. The mixture was stirred until the solution was clear and heated in an oven at 100 °C. After 24 hours, white crystals were formed. The vial was removed from the oven and the crystals were washed using DMF. The crystals were then analysed using SCXRD, PXRD, VT-PXRD, HSM, TGA and assessed for gas sorption.

2.3.3. Synthesis of LMMOF03

L3 (10 mg, 0.4 mmol), terephthalic acid (10 mg, 0.06 mmol) and $Zn(NO_3)_2{\cdot}6H_2O$ (20 mg, 0.07 mmol) were mixed in a 15 mL vial and dissolved in 5 mL DMF. The clear solution was heated in an oven at 100 °C for 24 hours. The brown crystals were washed using fresh DMF. The crystals were then analysed using SCXRD, PXRD, VT-PXRD, HSM, TGA and assessed for gas sorption.

2.3.4. Synthesis of LMMOF04

$CoCl_2{\cdot}6H_2O$ (20 mg, 0.08 mmol), 2,2-bipyridyl (10 mg, 0.06 mmol) and **L4** (10 mg, 0.67 mmol) were mixed in a 15 mL vial in 6 mL DMF and 4 mL EtOH solvent mixture. The mixture was stirred until the solution was clear and heated in an oven at 100 °C. After 96 hours, purple crystals were formed. The crystals were washed using fresh DMF and analysed using SCXRD, PXRD, HSM and TGA.

2.3.5. Synthesis of LMMOF05

L4 (10 mg, 0.05 mmol), phthalic acid and $CuCl_2$ (20 mg, 0.15 mmol) were mixed in a 15 mL vial and dissolved in a 2 mL DMF and 4 mL H_2O solvent mixture. The mixture was stirred until the solution was clear and heated in an oven at 100 °C. The crystals were then analysed using SCXRD, PXRD, HSM and TGA.

2.4. CHARACTERIZATION TECHNIQUES FOR THE NEW MOFs

Characterization of crystalline materials includes the evaluation of chemical arrangement, geometry, electrical and thermal properties of the crystalline solids.[4] There are different characterization techniques available for the analysis and characterization of crystalline solids.[5] Some of the most widely used characterization techniques include thermogravimetric analysis (TGA), hot stage microscopy (HSM), powder X-ray diffraction (PXRD), single-crystal X-ray diffraction (SCXRD), Brunauer–Emmett–Teller (BET) surface area analysis, UV spectroscopy (UV), and FT-IR spectroscopy (FTIR).[6] In this study, the newly synthesized crystalline MOFs were analysed using X-ray diffraction (SCXRD, PXRD, VT-PXRD) and thermal analysis (TGA and HSM) These techniques are explained in detail below.

2.4.1. Single-crystal X-ray diffraction

The single-crystal X-ray diffraction (SCXRD) technique is a non-destructive analytical technique used to provide data about the internal lattice of crystalline materials.[7] The single crystal required for the SCXRD must have a regular shape without cracks and spots, it should be stable and produce good diffraction. The SCXRD technique provides useful information such as atomic positions, crystal symmetry, unit cell dimensions, and space group.[8] These unit cell parameters are very useful in finding out whether the obtained structure is novel or has already been deposited in the Cambridge Structural Database (CSD).[9] In this study, SCXRD was used to determine the 3D atomic coordinates of the synthesized MOFs. The obtained crystals were covered in Paratone-N oil to prevent desolvation. A good quality single crystal was selected and mounted on a nylon loop and immersed in a cold nitrogen stream covered by dry air. The data were collected using a Bruker APEX II Duo diffractometer utilizing graphite monochromated MoK$_\alpha$ X-rays (λ = 0.71073 Å). An Oxford Cryostream-800 was used to maintain the temperature with a constant stream of nitrogen gas at a flow rate of 20 cm^3 min^{-1}. SAINT-Plus was used to supply data reductions and unit cell refinement. XPREP was used to determine the crystal system as well as the space group [10] which was further confirmed using LAYER[13] *via* the visual examination of the reciprocal lattice.[11] SHELXS (direct methods) was used to solve the structure while SHELXL was used to refine the structure.[12] XSeed[18] and OLEX2[13] programs were used as graphical interfaces to the SHELX suite of programs. POV-Ray images were generated using X-seed and Mercury.[15]

2.4.2. Powder X-Ray Diffraction and VT-PXRD

Powder X-ray diffraction (PXRD) is an analytical technique used for the identification of unknown crystalline materials, sample purity measurements and crystal structure determination.[18] PXRD is also used to verify if the bulk sample of the resynthesized material is the same as a previously synthesized compound. In this study, PXRD was used to confirm if the selected single-crystal analyzed using SCXRD was representative of the bulk sample. The synthesized crystals were removed from the mother solvent and dried on a filter paper. The samples were gently ground in a mortar before being placed on a zero-background sample holder. The experiments of variable-temperature PXRD (VT-PXRD) were performed under different temperatures guided by the thermal analysis results obtained from the thermogravimetric analysis. The Bruker D8 Advance diffractometer equipped with a Lynxeye detector using CuK$_\alpha$ radiation (λ = 1.5406 Å) was used to perform the PXRD and VT-PXRD measurements. The X-rays were generated with a current flow of 40 mA and voltage of 30 kV.

The scans were recorded over a 2θ range of 4 - 40°. The calculated PXRD patterns used as reference were generated using the program Mercury obtained from the fully refined single-crystal X-ray MOFs structures. The PXRD patterns were all plotted using Excel software.

2.4.3. Thermal analysis

Hot stage microscopy (HSM) and thermogravimetric analysis (TGA) techniques were used to determine the change in the behaviour of the samples upon heating.

2.4.3.1. Hot stage microscope (HSM)

Hot Stage Microscopy (HSM) is used to visualize desolvation and decomposition thermal events of MOFs. In this study, HSM was conducted on the synthesized MOF crystals to investigate the temperature at which the solvents are removed from the MOF structures, the temperature at which the crystal loses crystallinity and the temperature at which the decomposition of the framework begins. The images of the crystals viewed under a Nikon SMZ-10 stereoscopic microscope were captured using Sony Digital Hyper HAD colour video camera. The visualized images were saved on the Soft Imaging System program analysis (SIS). The sample was placed on a coverslip placed on a Linkam THMS600 hot stage connected to a Linkam TP92 temperature control unit. The crystals were covered in silicone oil followed by heating at a rate of 10 °C min^{-1}.

2.4.3.2. Thermogravimetric analysis (TGA)

Thermogravimetric analysis (TGA) is a reliable analytical technique which is applied in the determination of the thermal stability of a material. It records the weight change of the material as the sample is being heated constantly as a function of time and temperature.[16] [17] In this study, TGA was used to determine the host: guest ratio, the temperature at which desolvation takes place, and also the temperature at which the MOFs decompose. TGA measurements were carried out using TGA Q500 from TA Instruments. The sample with mass varying from 2-3 mg was placed inside an open pan which is attached to a balance. The sample was heated at a rate of 10 °C min^{-1} under a nitrogen purge flow of 60 ml min^{-1}. Results were processed using TA Universal software.

2.4.4. Gas sorption

Gas sorption studies were conducted to investigate the gas adsorption capabilities of the MOFs on gases such as carbon dioxide, nitrogen and hydrogen. The gas sorption experiments were carried out using a Micromeritics 3Flex Surface Area Analyzer. The samples, ranging in mass between 150–200 mg, were dried in a Micromeritics Flowprep with a constant flow of nitrogen gas. This was done to completely desolvate the sample by removing the solvents. Consequently, the sample was also heated under vacuum in situ before the analysis to dessolvate the MOFs making the pore of the MOFs structure empty and receptive to gas. For experiments performed at 273 K, 285 K and 293 K micromeritics water bath was used, and liquid nitrogen was used for experiments conducted at 77 K. A mixture of dry ice and acetone was used to perform gas sorption experiments at 195 K. Dry ice sublimes at −78 °C, a mixture of acetone and dry ice will maintain −78 °C. Also, the solution will not freeze because acetone requires a very low temperature to freeze. In this study, the gas sorption experiments were conducted to investigate the ability of **LMMOF01** to adsorb gases such as carbon dioxide, hydrogen and nitrogen and, to investigate the ability of **LMMOF02** and **LMMOF03** to adsorb carbon dioxide.

2.5. COMPUTER PACKAGES

2.5.1. X-Seed

X-Seed is a program for small-molecule crystallography.[18] It functions as a graphical user interface to SHELX and facilitates the production of high-quality molecular graphics images *via* Persistence of Vision Raytracer (POVray).

2.5.2. Conquest 2.0.5

The Cambridge Structural Database (CSD) (2020.0 CSD release) based on version 5.38, accessed *via* ConQuest, was used to search for information related to this study.[19] It offers a wide range of flexible search options permitting the retrieval of information confined within more than 1 million crystal structures.[19] In this study, CSD was used to check if the synthesized MOFs structures were novel.

2.5.3. Mercury 4.3.2

Mercury is a visualizer which provides tools used to obtain 3-D structure imagining and to explore the crystal packing and solvent-accessible volume of the MOF structure. [20,21] Mercury loads structural data from various formats and provides a wide range of possibilities to support the analysis of crystal structures.[15] This program also generates the packing diagrams of any number of unit cells in any viewed direction. In this study, the Mercury program was used to view the nature of the voids within the structures and to calculate solvent accessible volume.

Crystallographic data of L1 and L4

Identification code	**L1**	**L4**
Empirical formula	$C_{29}H_{19}N_4O_5$	$C_{23}H_{17}N_3O_9$
Formula weight	502.47	479.40
Temperature	173 (2) K	173(2) K
Wavelength	0.71073 Å	0.71073 Å
Crystal system	Triclinic	Monoclinic
Space group	*P*-1	*Pc*
Unit cell dimensions	*a* = 5.9017 (2) Å *b* = 10.9547 (4) Å *c* = 18.5087 (6) Å α =100.5080 (1)° β = 90.0040 (1)° γ =102.7740(1)°	a = 31.387(6) Å b = 4.7952(1) Å c = 17.537(4) Å α = 90° β = 105.976(3) ° γ = 90°
Volume	1146.41 (7) $Å^3$	2537.5(9) A^3
Z	2	4
Density (calculated)	1.456 g/cm^3	1.255 g/cm^3
Absorption coefficient	0.102 mm^{-1}	0.099 mm^{-1}
F(000)	520	992
Crystal size	0.22x 0.13 x 0.06 mm^3	0.24 x 0.11 x 0.10 mm^3
Theta range for data collection	1.12° to 29.62°	1.35° to 27.60°
Index ranges	-8<=h<=8, -15<=k<=15, -25<=l<=25	-40<=h<=40, -6<=k<=6, -22<=l<=22
Reflections collected	48810	57235
Independent reflections	6454[R(int)= 0.0493]	11759 [R(int) = 0.0526]
Completeness to theta = 29.62 °	99.8%	99.9 %
Max. and min. transmission	0.9939 and 0.9779	0.9904 and 0.9771
Refinement method	Full-matrix least-square on F^2	Full-matrix least-squares on F^2
Data/ restraints/ parameters	6454/ 0 /343	11759 / 2 / 285
Goodness-of-fit on F^2	1.064	3.165
Final R indices [I>2sigma(I)]	R_1 = 0.0449 wR_2 =0.1174	R_1 = 0.2449 wR_2 = 0.6124
R indices (all data)	R_1 = 0.0557 wR_2 =0.1174	R_1 = 0.2551 wR_2 = 0.6248
Largest diff. peak and hole	0.458 and -0.244 e.$Å^{-3}$	2.937 and -1.893 e. $Å^{-3}$

REFERENCES

1 P. Pachfule, R. Das, P. Poddar and R. Banerjee, *Cryst. Growth Des.*, 2011, **11**, 1215–1222.

2 J. Yang, B. Li, J.F. Ma, Y. Liu and J.P. Zhang, *Chem. Commun.*, 2010, **46**, 8383.

3 D. K. Maity and D. Ghoshal, *J. Indian Inst. Sci.*, 2017, **97**, 261–279.

4 S. Mourdikoudis, N. T. K. Thanh and R. M. Pallares, *Nanoscale*, 2018, **10**, 12871–12934.

5 M. Ramya, N. Muthukumar, *Int. J. Pure Appl. Math.*, 2017, **116**, 2017.

6 J. Ramya, P. H. Hussain, *Int. J. Pure Appl. Math.*, 2017, **116**, 57–61.

7 A. A. Bunaciu, E.G. Udristioiu and H. Y. Aboul-enein, *Crit. Rev. Anal. Chem.*, 2015, **45**, 298–299.

8 K. Hasegawa, and J. *Rigaku* , 2012, **28**, 14–18.

9 S. Saravana and S. Arulselvi, *J. Pure Appl. Math.*, 2017, **116**, 399–403.

10 W. Kabsch, *J. Appl. Crystallogr.*, 1988, **21**, 916–924.

11 L. J. Barbour, *J. Appl. Crystallogr.*, 1999, **32**, 351–352.

12 G. M. Sheldrick, *Acta Crystallogr. Sect. A Found. Crystallogr.*, 2008, **64**, 112–122.

13 L. J. Barbour, *J. Supramol. Chem.*, 2001, **1**, 189–191.

14 O. V. Pavlyuk, Y. I. Slyvka, N. T. Pokhodylo and M. G. Mys'kiv, *Vopr. Khimii i Khimicheskoi Tekhnologii*, 2021, **41**, 84–89.

15 C. F. Macrae, P. R. Edgington, P. McCabe, E. Pidcock, G. P. Shields, R. Taylor, M. Towler and J. van de Streek, *J. Appl. Crystallogr.*, 2006, **39**, 453.

16 V. V Butova, M. A. Soldatov, A. A. Guda, K. A. Lomachenko and C. Lamberti, *Russ. Chem. Rev.*, 2016, **85**, 280–307.

17 M. V. Borrachero, J. Payá, M. Bonilla and J. Monzó, *J. Therm. Anal. Calorim.*, 2008, **91**, 503–509.

18 L. J. Barbour, *J. Supramol. Chem.*, 1999, **5**, 108.

19 C.R. Groom, I.J. Bruno, M.P. Lightfoot and S.C. Ward, Acta Cryst, 2016, B72, 171-179.

20 D. Moghadam, P.Z. Li, A. Wiggin, S.B. Tao, A. Maloney, A.G.P. Wood, P.A. Ward, S.C. Fairen-Jimenez, *Chem. mater*, 2017, **29**, 2618–2625.

21 C.F. Macrae, I.J. Bruno, J.A. Chisholm, P.R. Edgington, P. McCabe, E. Pidcock, L. Rodriguez-Monge, R. Taylor, J. van de Streek and P.A. Wood, *J. Appl. Crystallogr.*, 2008, **41**, 466.

22 C.F. Macrae, I. Sovogo, S.J. Cottrell, P.T.A. Galek, P. McCabe, E. Pidcock, M. Platings, G.P. Shields, J.S. Stevens, M. Towler and P.A. Wood, *J. Appl. Crystallogr.*, 2012, **38**,470.

CHAPTER 3

MIXED-LIGAND MOFS BASED ON COBALT AND ZINC

This chapter discusses the characterization and structural analysis of the following MOFs; {[$Zn_2(OBZ)_2$(**L2**)]·$(DMF)_3$}$_n$ (**LMMOF01**), {[Zn(TPA)(**L4**)$_{0.5}$]·$(DMF)_2$}$_n$ (**LMMOF02**), {[$Co_3(TPA)_3$(**L1**)]·$(DMF)_4$}$_n$ (**LMMOF03**). The MOFs were characterized using X-ray diffraction (SCXRD and PXRD) and thermal analysis (TGA and HSM). The solvent-accessible volume of the MOFs was estimated using the Mercury program (0.7 Å grid spacing, 1.2 Å probe radius). The MOFs were also assessed for their gas sorption capabilities. This chapter is divided per each characterisation technique wherein the analytical results for each compound are discussed. Crystallographic data of **LMMOF01**, **LMMOF02** and **LMMOF03** are given on page 77.

3.1. LMMOF01

3.1.1. Single-crystal X-ray diffraction (SCXRD)

Crystal structure details of LMMOF01

Molecular formula: $C_{59} H_{40} N_5 O_{17} Zn_2$

Formula Weight: 1221.70 g mol^{-1}

a = 14.024(2) Å	α = 78.350(11)°	Space group: *P*1
b = 14.211(2) Å	β = 79.244(11)°	*Z = 2*
c = 1 6.787(2) Å	γ = 67.243(7)°	*V* = 2999.8(9) Å^3

LMMOF01 was synthesised by the reaction of *N*,*N*'–bis–(3-pyridylmethyl)–biphenyl diimide (**L2**), 4,4'-oxybis(benzoic acid) and zinc(II) nitrate hexahydrate under solvothermal conditions(100 °C, DMF). **LMMOF01** crystallizes in the triclinic space group *P*1. The asymmetric unit (ASU) consists of one **L2** molecule, two oxybis(benzoate) anions, two zinc(II) ions and three DMF molecules (Figure 3.1). Two of the three DMF molecules are disordered and could not be modelled. The coordination environment consists of [$Zn_2(COO)_4$] units and nitrogen atoms at the apex (Figure 3.2). The packing diagram of **LMMOF01** viewed along the *c* axis displaying DMF

molecules occupying the channels is shown in Figure 3.3. The compound has a potential solvent-accessible volume of 36.5% and contains 3-D channels (Figure 3.4).

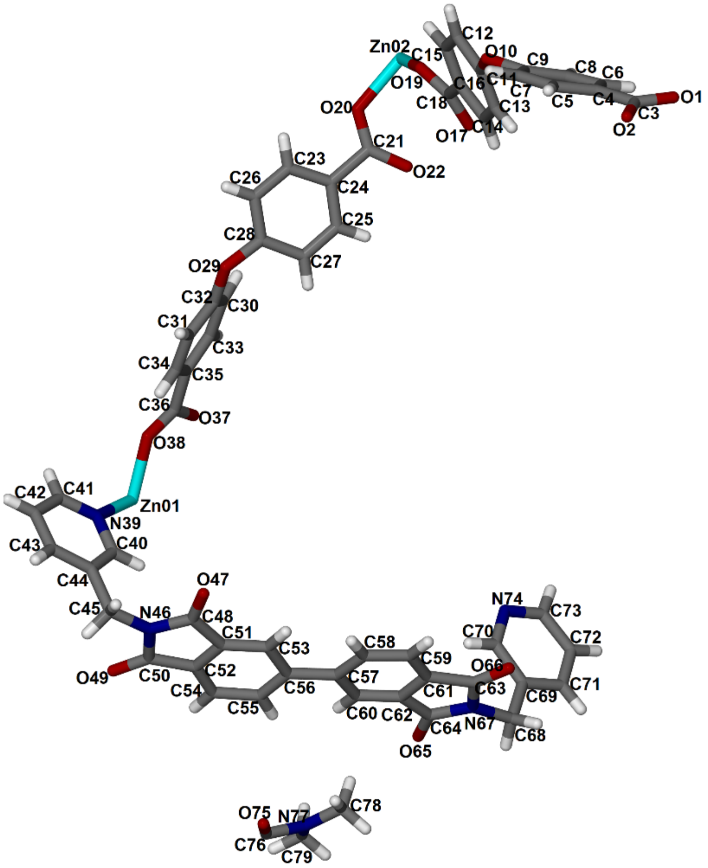

Figure 3.1 The asymmetric unit of **LMMOF01** showing the crystallographic labelling scheme.

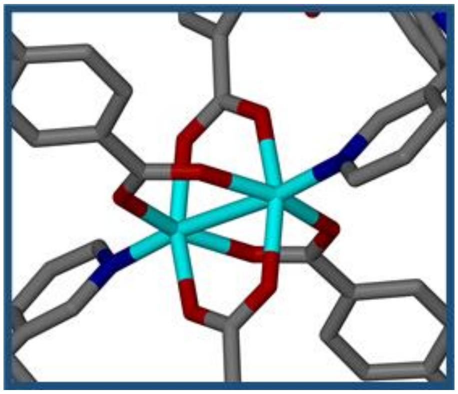

Figure 3.2 The coordination environment around the Zn(II) metal centre.

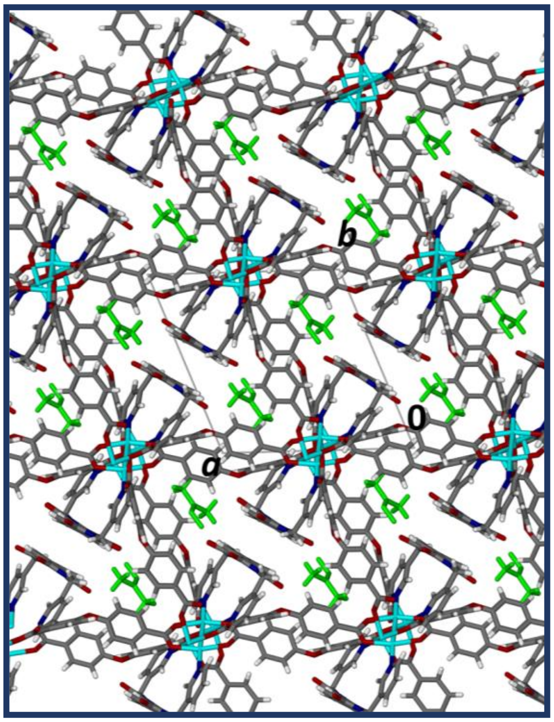

Figure 3.3 The packing diagram of **LMMOF01** viewed in the *ab* plane. The DMF (lime) molecules are in channels running along the *c* axis.

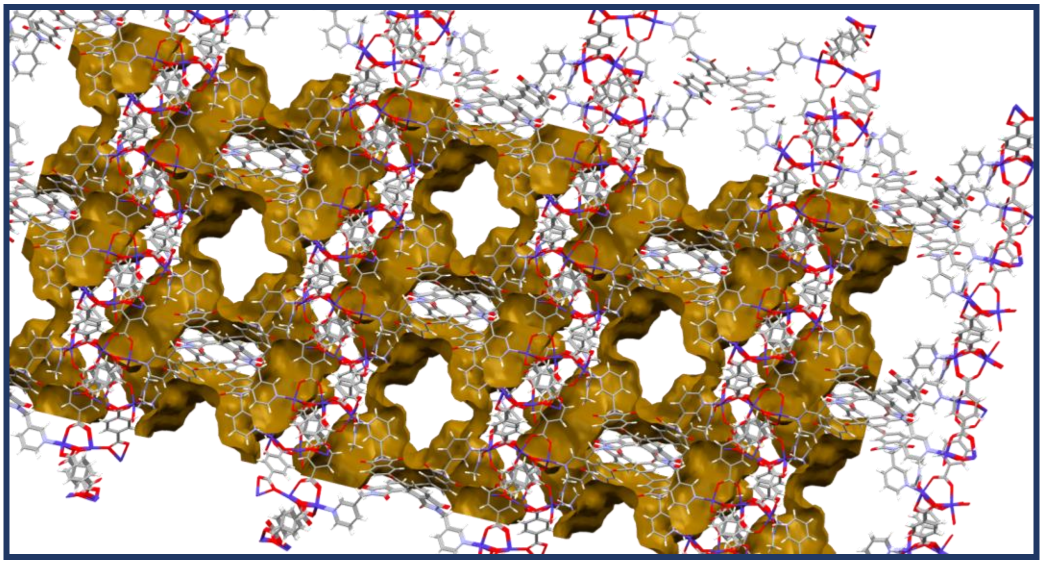

Figure 3.4 A plot of solvent accessible volume in **LMMOF01**. The structure possesses channels extending in three dimensions.

3.1.2. Powder X-ray Diffraction of LMMOF01

The phase purity of **LMMOF01** crystals was confirmed by PXRD measurements. The calculated PXRD pattern is slightly different from the as-synthesized powder pattern (Figure 3.5). The intensities of the peaks on the calculated pattern are stronger than those of the as-synthesized and some of the peaks present on the calculated pattern are missing on the air-dried, desolvated and the as-synthesized samples. This may be attributed to the preferred orientation of the powder samples. **LMMOF01** remains crystalline after desolvation and, the PXRD pattern of the desolvated phase shows minor differences from the as-synthesized PXRD pattern. This may be due to a structural adjustment due to solvent loss.

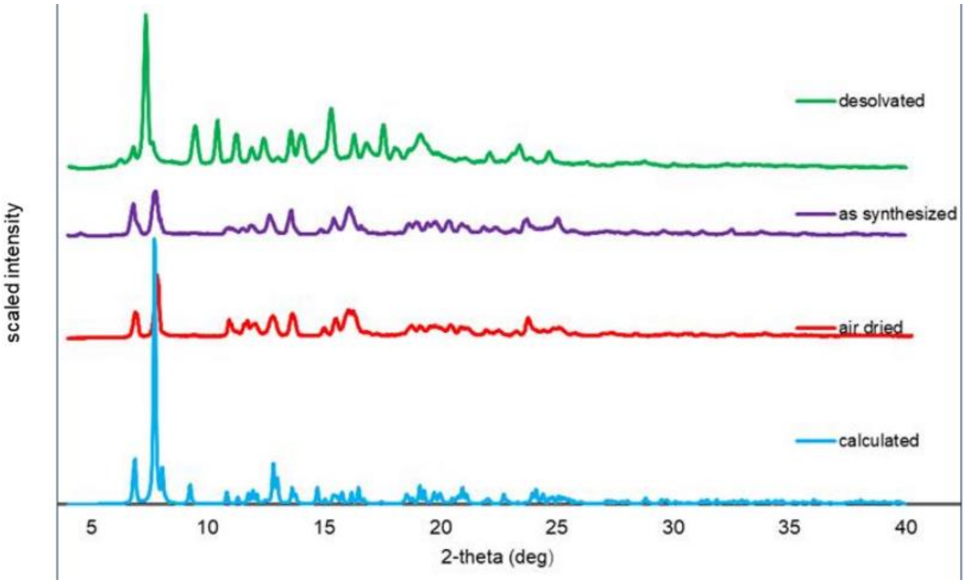

Figure 3.5 The PXRD patterns of **LMMOF01**, calculated (blue), air dried (red), as-synthesized (purple) and desolvated (green) respectively.

3.1.3. Variable-temperature powder X-ray diffraction (VT-PXRD)

To determine the stability of the **LMMOF01** at different temperatures, PXRD patterns (Figure 3.6) were recorded at 25 °C intervals from 25 °C to 300 °C. The PXRD patterns show that the sample retains crystallinity with desolvation up to 300 °C and upon cooling to 25 °C in an open chamber.

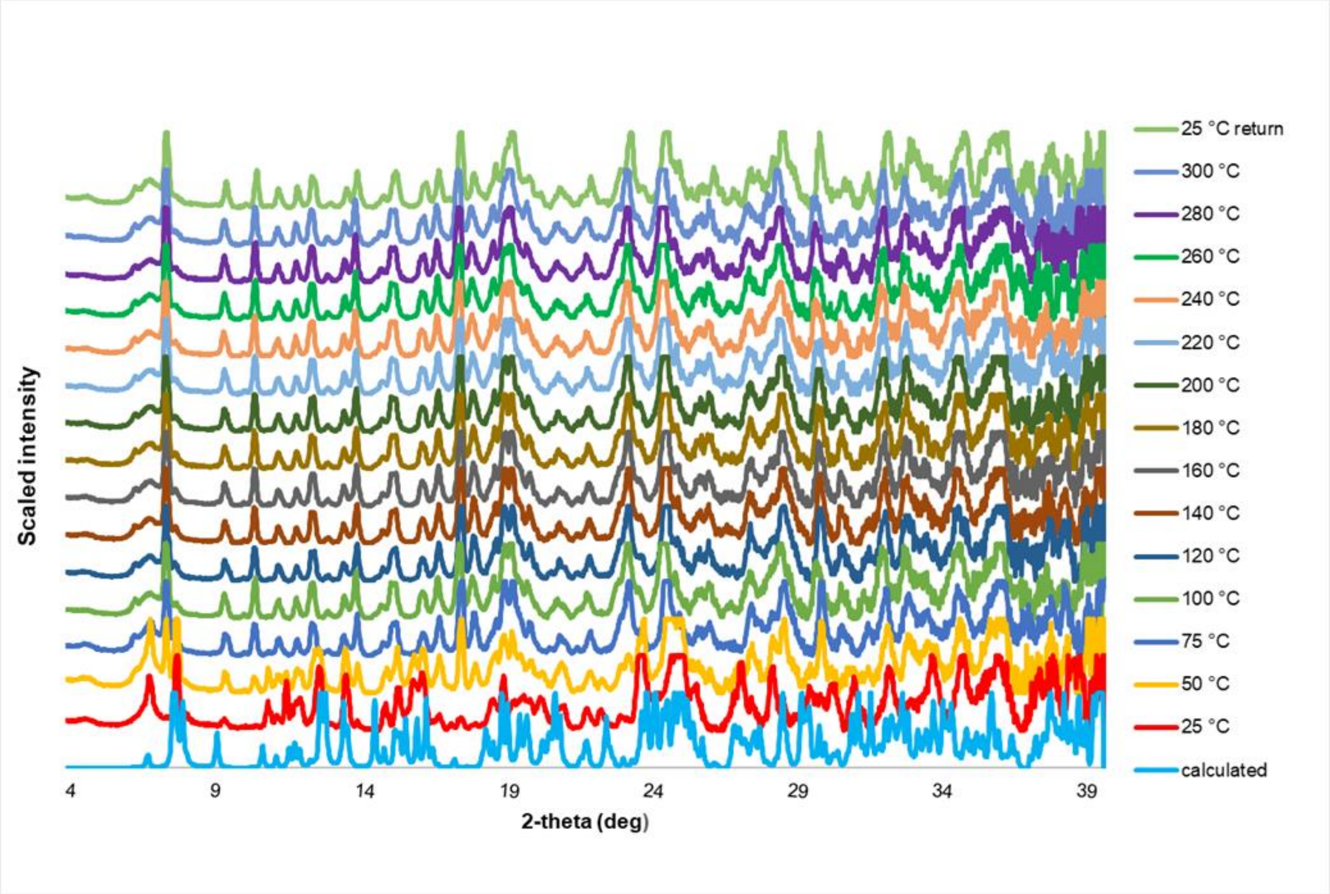

Figure 3.6 VT-PXRD patterns of as-synthesized **LMMOF01** at different temperatures (25 °C - 300 °C). (As the temperature increases from 75 °C to higher temperatures, some of the peaks thicken and become short due to the change of the structure as it's being heated)

3.1.4. Hot stage microscopy (HSM)

HSM was conducted on the as-synthesized **LMMOF01** crystals to investigate the temperature at which the solvent is removed from the MOF, the temperature at which the crystal starts to lose its crystallinity and the temperature at which decomposition of the framework starts. At 190 °C the crystals of **LMMOF01** started bubbling which is due to the solvent leaving the framework. There are more bubbles at 210 °C meaning that most of the DMF is leaving the MOF cavities and it can also be noticed that the MOF starts decomposing at 230 °C. At 250 °C the colour changes from cream white to brownish and it is visible that the crystals are no longer crystalline. A more visible crystal disintegration is observed at 315 °C and is accompanied by fewer bubbles and complete decomposition of the framework (Figure 3.7).

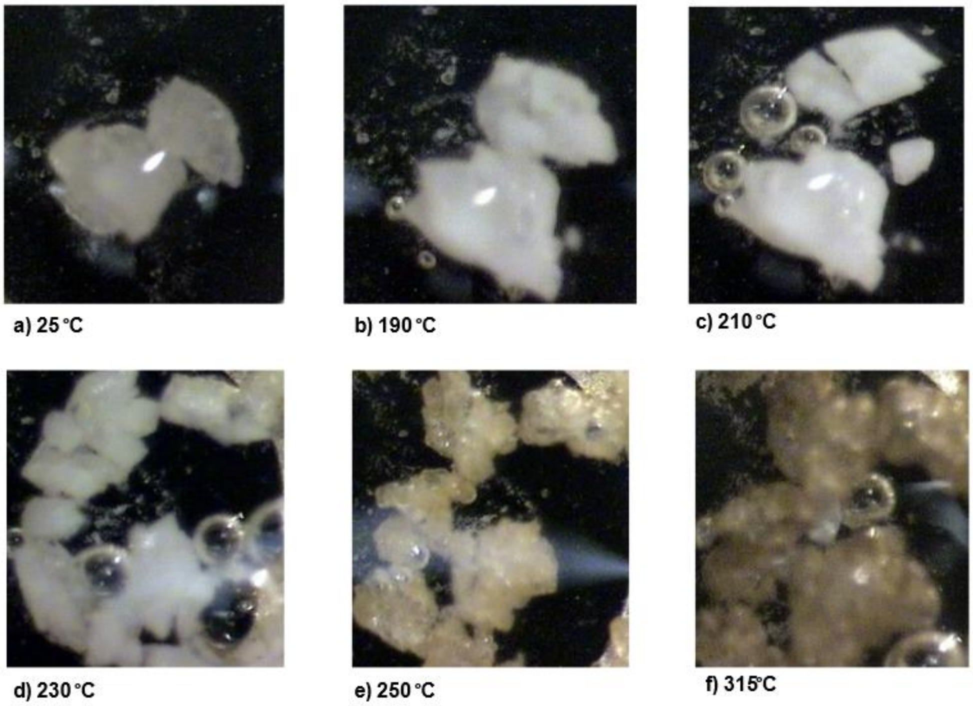

Figure 3.7 LMMOF01 HSM snapshots captured at different temperatures: (a) 25 °C, (b) 190 °C, (c) 210 °C, (d) 230 °C, (e) 250 °C and (f) 315 °C.

3.1.5. Thermogravimetric analysis

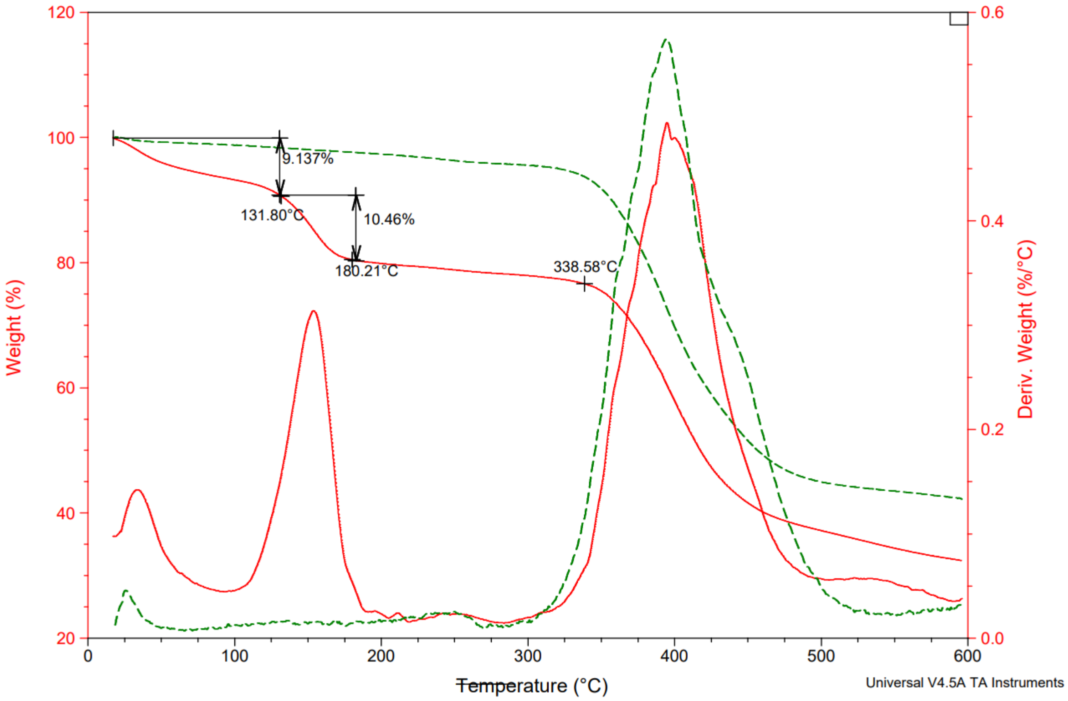

Figure 3.8 TGA profiles of as-synthesized **LMMOF1** (green solid line) and desolvated **LMMOF1** (dashed red) as well as the first derivatives; as-synthesized (solid green) and desolvated (dashed red).

TGA was performed to investigate the thermal stability of **LMMOF01**. The thermal profile of the as-synthesized **LMMOF01** shows a weight loss of 17.18% (calculated 18.31%) in the temperature range of 20°C to 314°C (Figure 3.8). The weight loss is attributed to the loss of three DMF molecules at 190 °C. The framework remains intact after the removal of the solvent from the temperature range of 190 °C – 315 °C and starts to decompose at 315 °C. The TGA results agree with the HSM results. The guest solvent started leaving the MOF at 190 °C in both cases and the decomposition occur at 315 °C in all cases. The desolvated phase of **LMMOF01** was prepared by heating the as-synthesized crystals in an oven under a vacuum at 100 °C for twenty-four (24) hours. TGA was also performed on the desolvated **LMMOF01** to confirm the process of desolvation (Figure 3.8). Desolvated **LMMOF01** remains stable up to 315 °C after which decomposition commences.

3.1.6. Gas sorption

3.1.6.1. CO_2 absorption and desorption

Carbon dioxide adsorption on desolvated **LMMOF01** was done at 195 K, 273 K, 283 K and 298 K respectively. The MOF absorbs more carbon dioxide at 195 K than at 273 K, 283 K and 298 K. At 195 K, desolvated **LMMOF01** adsorbs 120 cm^3 g^{-1} (STP) at *P*/*P*°= 0.90 and displays a reversible type-IV isotherm. This type of isotherm is characterized by clear, broad hysteresis loops (Figure 3.9). The first structural change is observed at *P*/*P*° = 0.2 after the MOF adsorbs 50 cm^3 g^{-1} (STP) followed by the structure opening at 0.35 *P*/*P*° and adsorbing an additional 70 cm^3 g^{-1} (STP). At 273 K, desolvated **LMMOF01** adsorbs 15.1 cm^3 g^{-1} (STP) at 0.030 *P/P*° and displays a reversible type-I isotherm which is characteristic of microporous solids (Figure 3.10). Desolvated **LMMOF01** also displays a type-I isotherm at 283 K (Figure 3.11) and 298 K (Figure 3.12) and adsorbs 11.99 cm^3 g^{-1} (STP) at 0.023 *P*/*P*° and 8.55 cm^3 g^{-1} (STP) at 0.017 *P*/*P*°, respectively. It can be concluded that when the temperature increases, the quantity of gas adsorbed decreases. Desolvated **LMMOF01** absorbs more carbon dioxide at a lower temperature because adsorption is an exothermic process, and is thus favoured by lower temperatures.

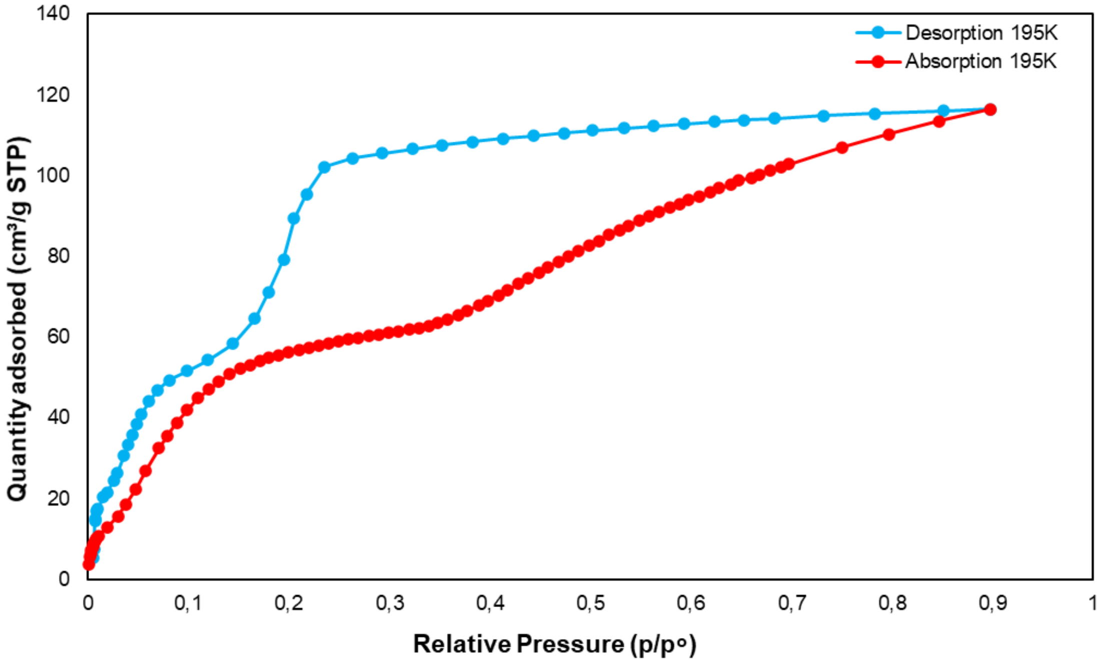

Figure 3.9 CO_2 adsorption (red) and desorption (blue) isotherms of desolvated **LMMOF01** at 195 K.

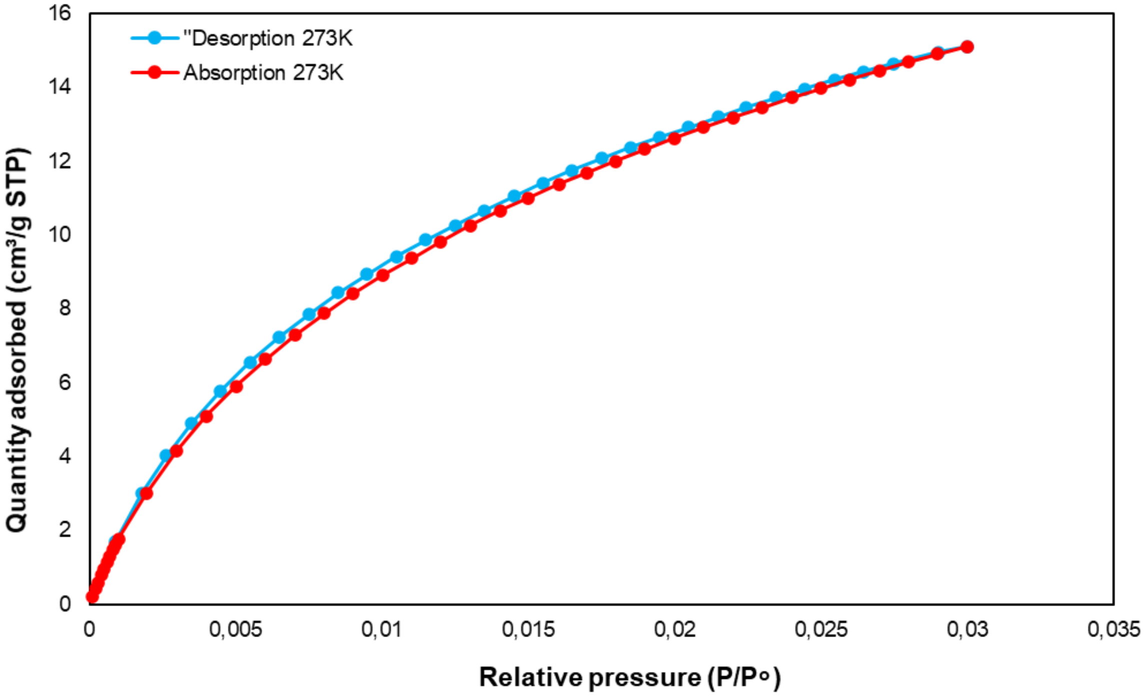

Figure 3.10 CO_2 adsorption (red) and desorption (blue) isotherms of desolvated **LMMOF01** at 273 K.

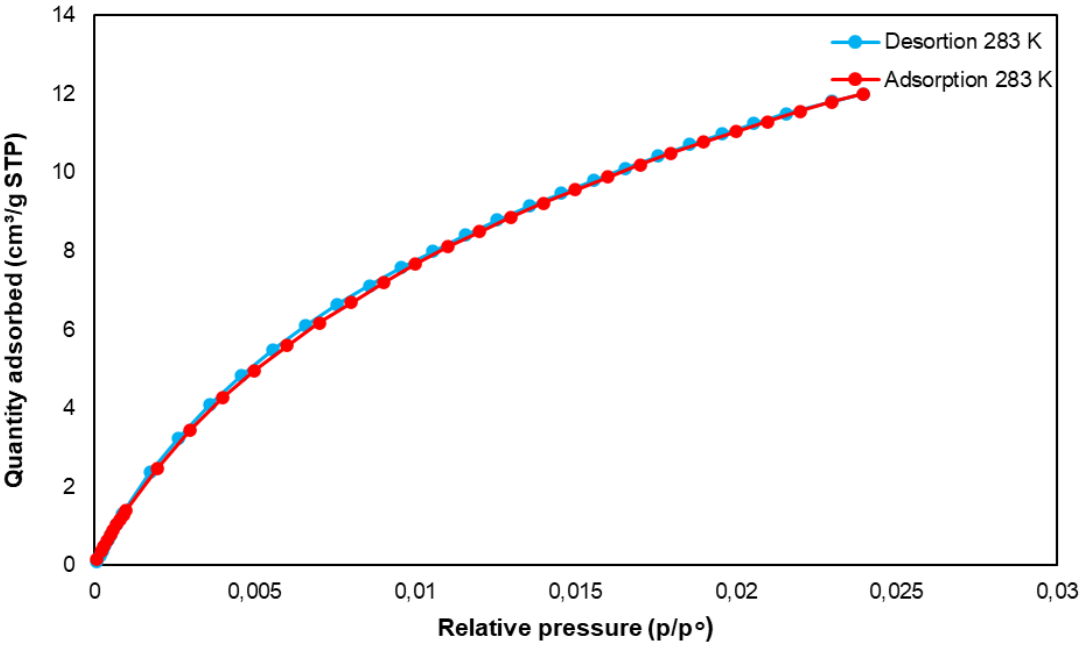

Figure 3.11 CO_2 adsorption (red) and desorption (blue) isotherms of desolvated **LMMOF01** at 283 K.

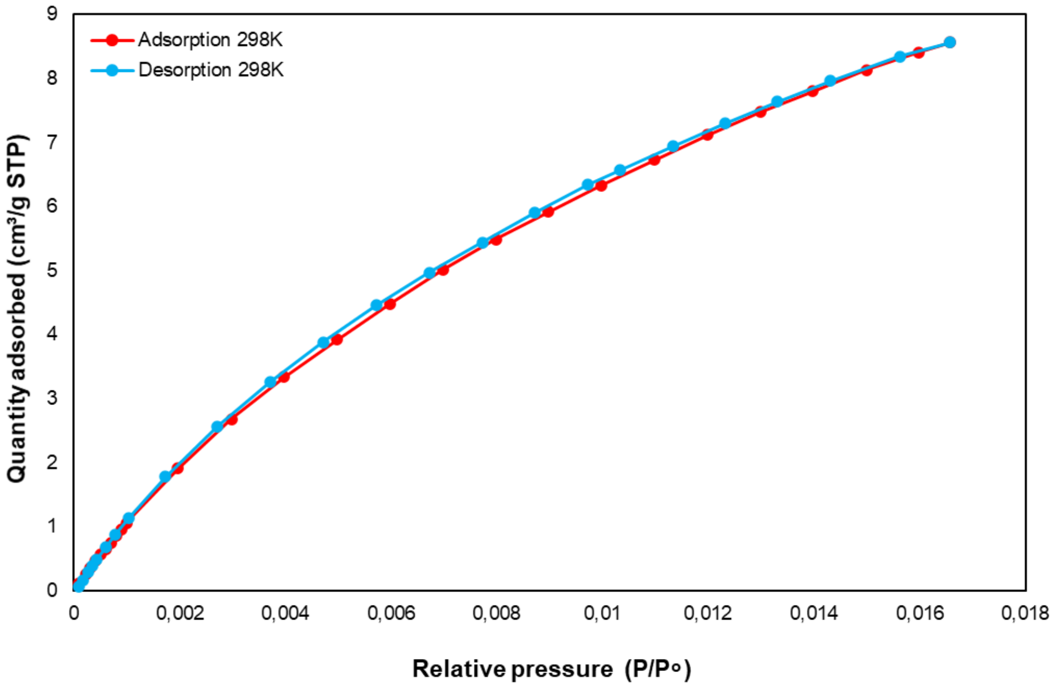

Figure 3.12 CO_2 adsorption (red) and desorption (blue) isotherms of desolvated **LMMOF01** at 298 K.

3.1.6.2. Hydrogen gas adsorption

The hydrogen sorption capacity of desolvated **LMMOF01** was investigated at 77 K (Figure 3.13). The desolvated **LMMOF01** hydrogen sorption isotherm displays reversible type-I behaviour with some degree of hysteresis. The MOF adsorbs approximately 3.00 cm^3 g^{-1} (STP).

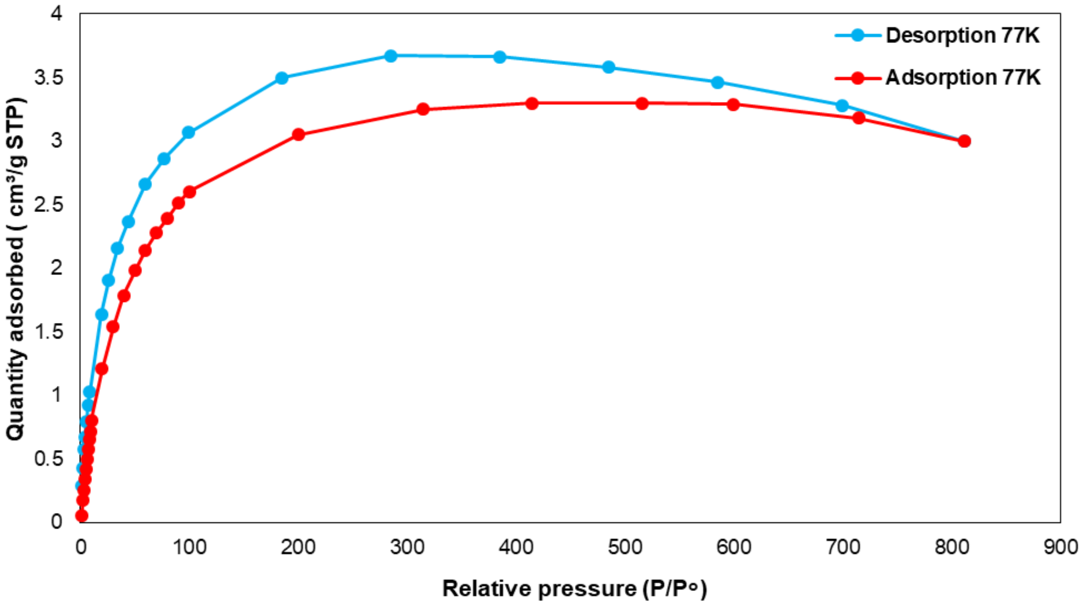

Figure 3.13 H_2 adsorption (red) and desorption (blue) isotherms of desolvated **LMMOF01** at 77 K.

3.1.6.3. Nitrogen gas sorption

The N_2 sorption capacity of desolvated **LMMOF01** was investigated at 77 K (Figure 3.14). Desolvated **LMMOF01** displays a reversible type-II sorption isotherm which is characteristic of mesoporous materials composed of multilayers. The compound adsorbs roughly 11.99 cm^3 g^{-1} (STP) N_2 at 1.02 *P*/*P*°.

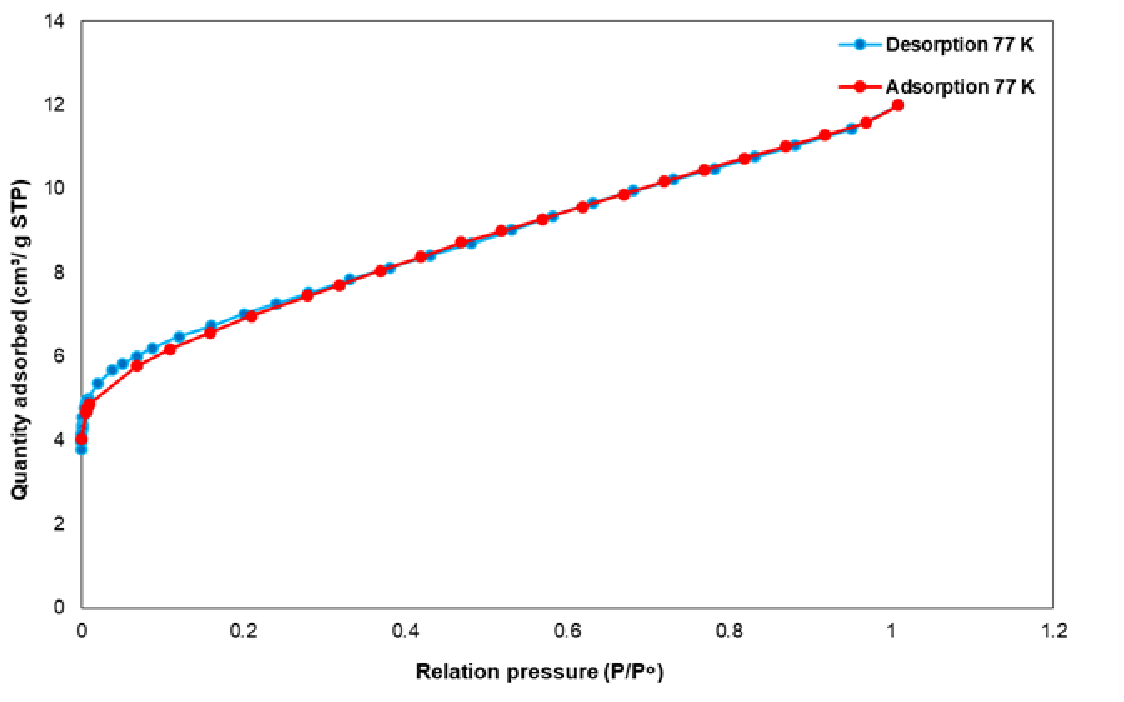

Figure 3.14 N_2 adsorption (red) and desorption (blue) isotherms of desolvated **LMMOF01** at 77 K

3.2. LMMOF02

3.2.1. Single-crystal X-ray diffraction

Crystal structure details of LMMOF02

Molecular formula: $C_{26}H_{19}N_4O_8Zn$

Formula Weight: 580.82 g mol^{-1}

a = 8.5682(12) Å	α = 91.438(2)°	Space group: *P*1
b = 12.1958(16) Å	β = 99.663(3)°	*Z* = 2
c = 2.5471(18) Å	γ=106.671(2)°	*V* = 1234.5(3) Å^3

LMMOF02 was synthesised by the reaction of *N*,*N*'–bis–(3-pyridylmethyl)–biphenyl diimide **(L3)** terephthalic acid and zinc(II) nitrate hexahydrate under solvothermal conditions (100 °C, DMF). **LMMOF02** crystallises in the triclinic space group *P*1. The ASU of **LMMOF02** structure consists of half an **L3** molecule, two independent halves of terephthalate anion, a coordinated DMF molecule and an uncoordinated DMF molecule which is disordered (Figure 3.15). The metal

centre is coordinated to the **L3** molecule *via* the pyridyl nitrogen atom, two independent halves of terephthalate anion *via* the carboxylate oxygen atoms, and to a DMF molecule *via* an oxygen atom (Figure 3.16(a)). The 2-D network of **LMMOF02** is shown in (Figure 3.16(b)). The packing diagram of **LMMOF02** viewed onto the *a* axis direction showing the channels occupied by the DMF molecules is shown in Figure 3.17. The compound has a potential solvent-accessible volume of 31.5% and contains 2-D channels (Figure 3.18).

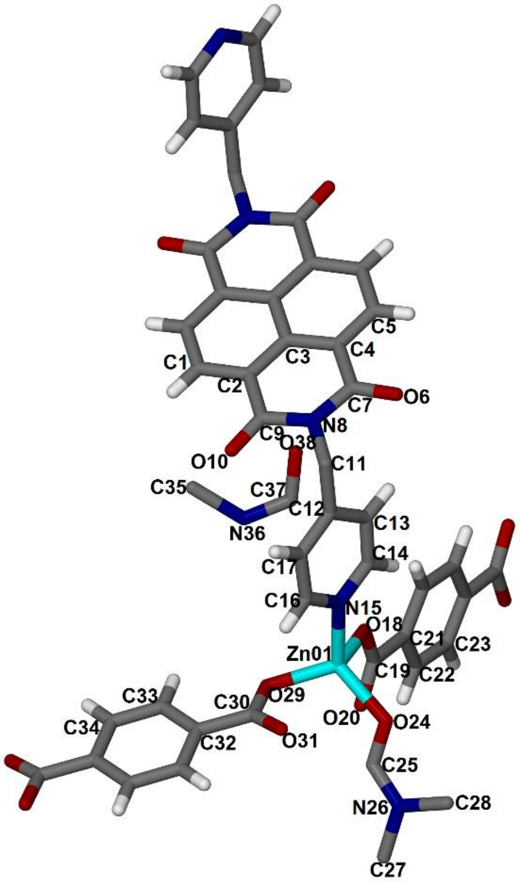

Figure 3.15 The molecular structure of **LMMOF02** showing crystallographic labelling scheme for the ASU.

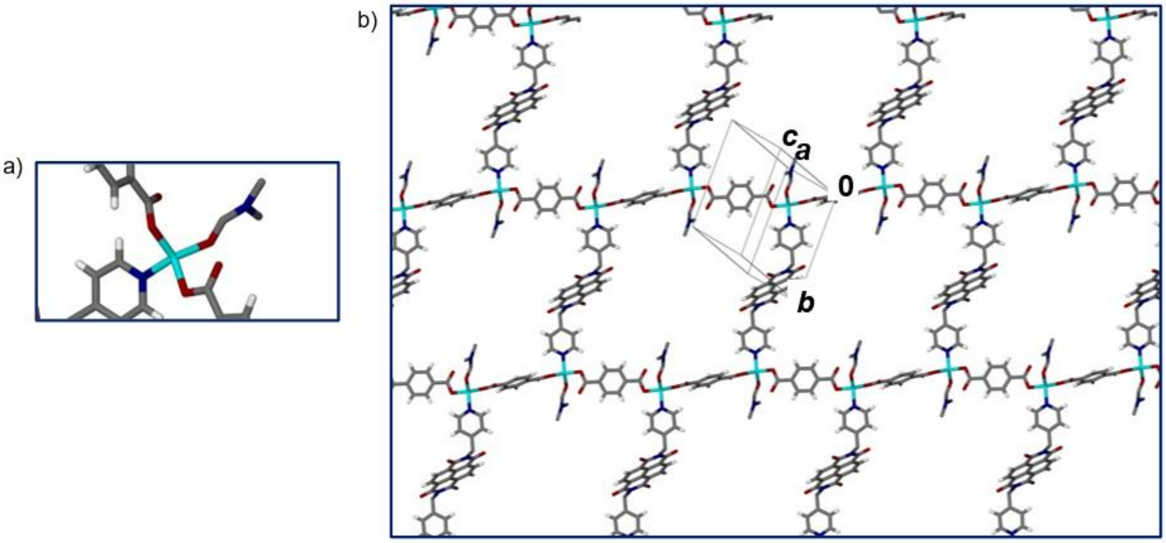

Figure 3.16 (a) The coordination environment around Zn(II) centre and (b) a 2-D network of **LMMOF02**.

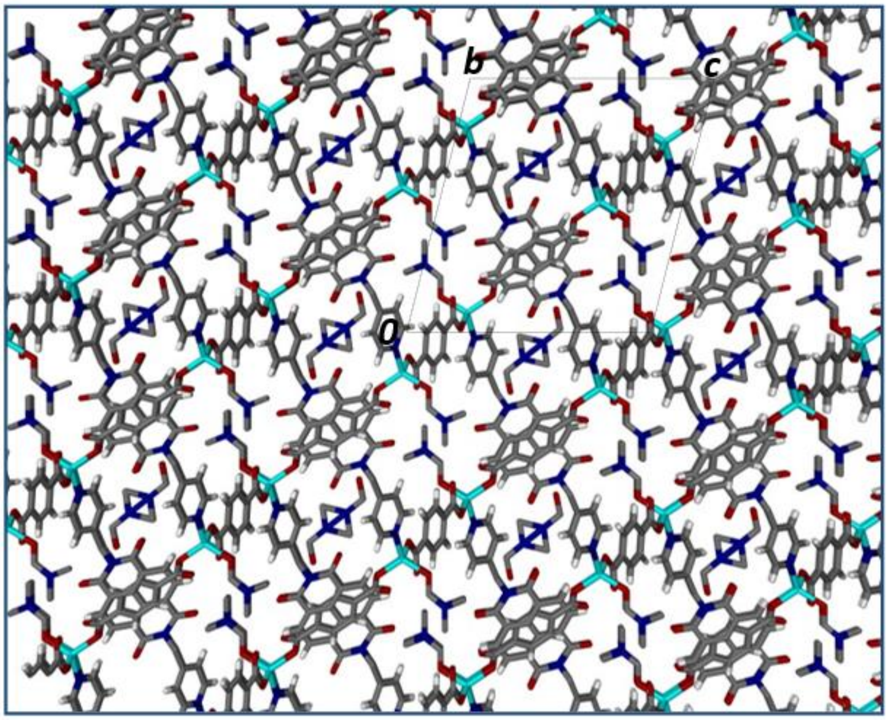

Figure 3.17 The packing diagram of **LMMOF02** viewed down the *a*-axis. The DMF molecules are occupying the pores of the MOF. Hydrogen atoms of the DMF are omitted for clarity.

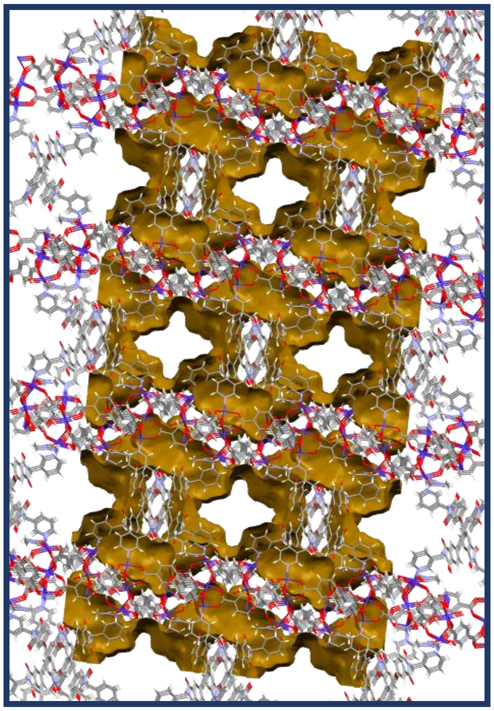

Figure 3.18 A plot of solvent-accessible volume (31.5%) in **LMMOF02**. The structure possesses channels extending into two dimensions.

3.2.2. Powder X-ray Diffraction

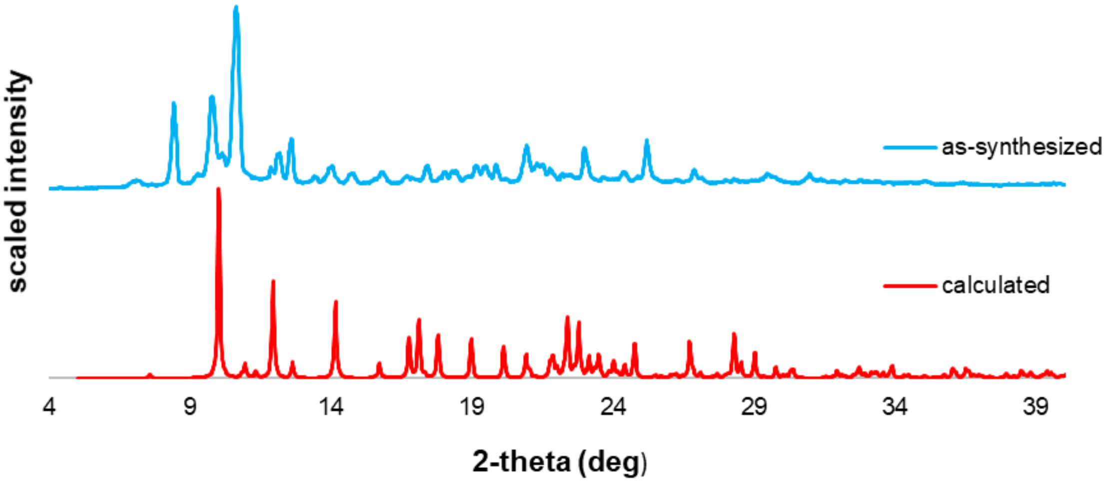

Figure 3.19 The simulated and as-synthesized PXRD patterns of **LMMOF02**.

Crystals of **LMMOF02** were gently ground into a fine powder before being analysed using PXRD. The calculated powder pattern was obtained from the Mercury program and it was compared to the PXRD patterns of the as-synthesized material. There is a little resemblance between the PXRD pattern of the as-synthesized material and the calculated PXRD pattern, this is maybe due to impurities present in the as-synthesized sample (Figure 3.19). Differences in relative peak heights in the experimental pattern can be ascribed to preferred orientation effects.

3.2.3. Variable-temperature powder X-ray diffraction (VT-PXRD)

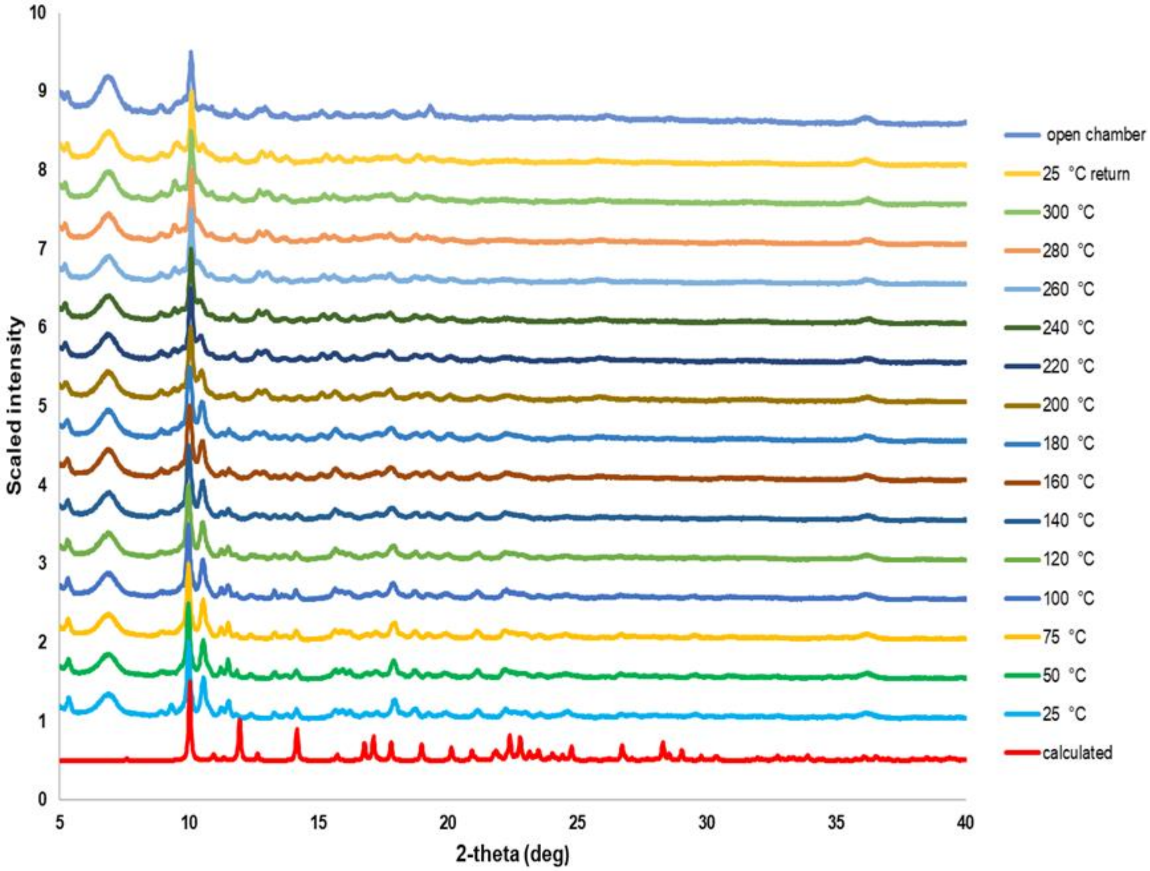

Figure 3.20 VT-PXRD patterns of as-synthesized **LMMOF02** at different temperatures. As the temperature increases, the broadening and the loss of the peaks show a reduction in the crystallinity of the compound.

The VT-PXRD patterns of **LMMOF02** (Figure 3.20) were recorded from 25 °C to 300 °C. The PXRD patterns at elevated temperatures show that the sample retains crystallinity during heating (up to 300 °C) and on cooling to 25 °C in an open chamber.

3.2.4. Hot stage microscopy

HSM was conducted on the as-synthesized **LMMOF02** crystals from 25 °C to 400 °C. The bubbles formed by **LMMOF02** under the microscope were too faint to capture thus the exact temperature at which the solvent started leaving the framework cannot be stated (Figure 3.21). The colour of the crystals changes light brown to dull gold at 275 °C. The crystals start to lose their crystallinity at 275 °C. At 343 °C, the crystals become brown which symbolises the complete decomposition of the framework.

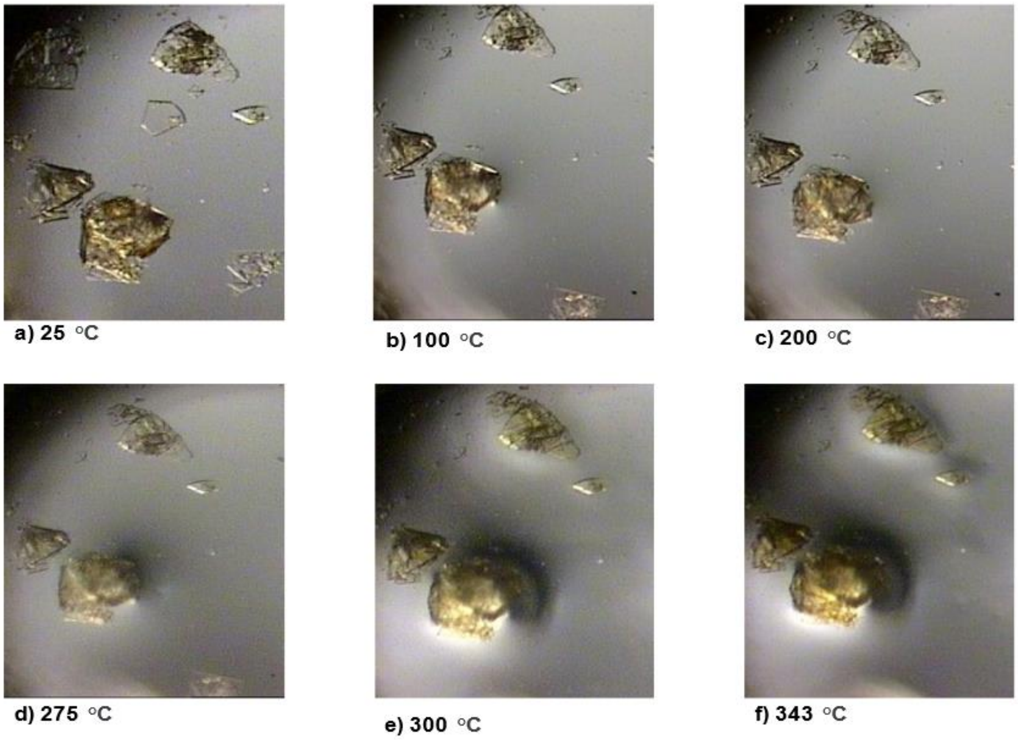

Figure 3.21 LMMOF02 HSM snapshots captured at different temperatures: (a) 25 °C, (b) 100 °C, (c) 200 °C, (d) 275 °C and (e) 300 °C (f) 343 °C.

3.2.5. Thermogravimetric analysis of LMMOF02

The TGA analysis was performed to investigate the thermal stability of the **LMMOF02**. The thermal profile of the as-synthesized **LMMOF02** shows two distinct weight losses. The first weight loss is attributed to the uncoordinated DMF molecules in the pores and the second weight loss is attributed to the coordinated DMF. The TGA shows a total weight loss of 11.78% (calculated 13%) at 195 °C. The framework remains intact from the temperature range of 43 °C – 343 °C and starts to decompose at 343 °C (Figure 3.22). Desolvated **LMMOF02** was obtained by heating the **LMMOF02** crystals under vacuum in situ. The TGA graph of the desolvated

LMMOF02 shows that the MOF is stable from 25 °C to 349 °C and decomposition begins at 349 °C.

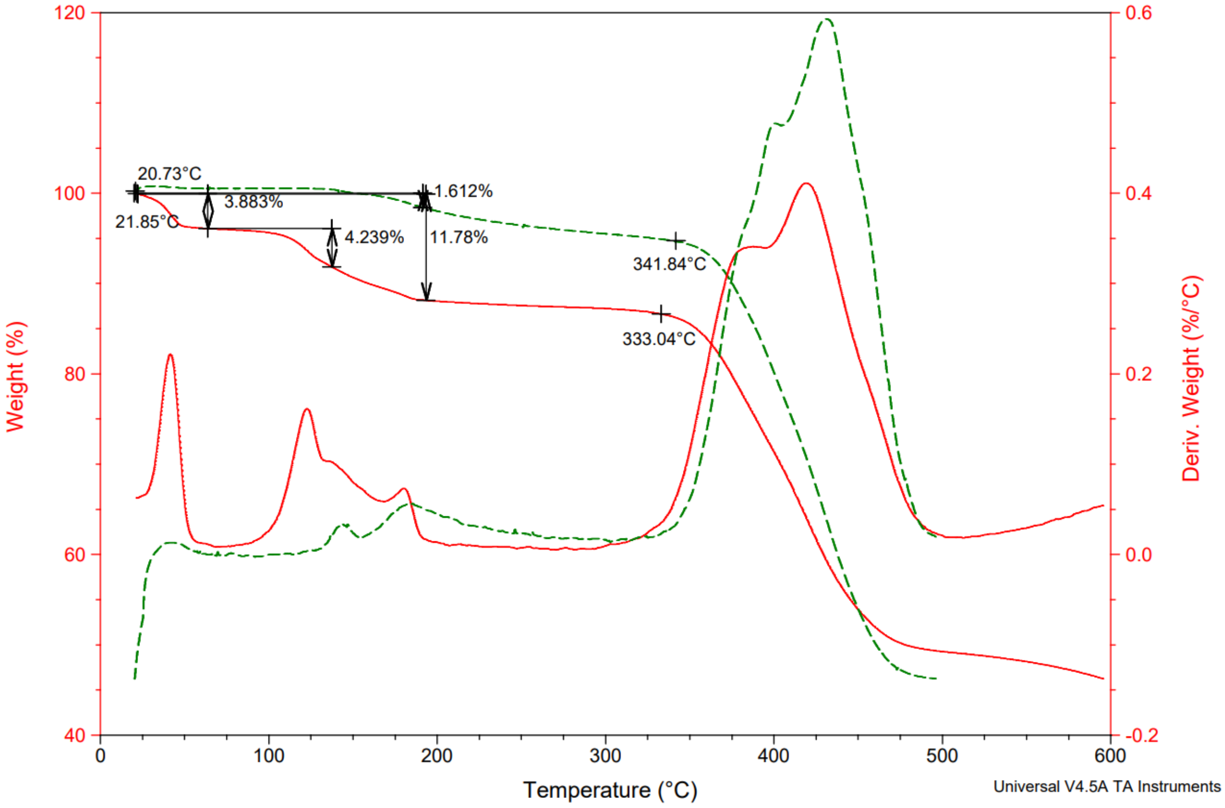

Figure 3.22 TGA profiles of as-synthesized **LMMOF02** (red) and its first derivatives (red) and the desolvated **LMMOF02** (dashed lime) and its derivative weight (dashed lime).

3.2.6. Gas sorption

The porosity of the desolvated **LMMOF02** was investigated using carbon dioxide at 195 K and 273 K. At both temperatures, the sorption isotherm obtained resembles a type-I curve and shows a slight hysteresis on the desorption curve. The compound adsorbs more carbon dioxide at 195 K (65 cm^3 g^{-1} (STP) at $P/P°$ = 0.93) than at 273 K (30 cm^3 g^{-1} (STP) at 0.03 $P/P°$) (Figures 3.23 and 3.24).

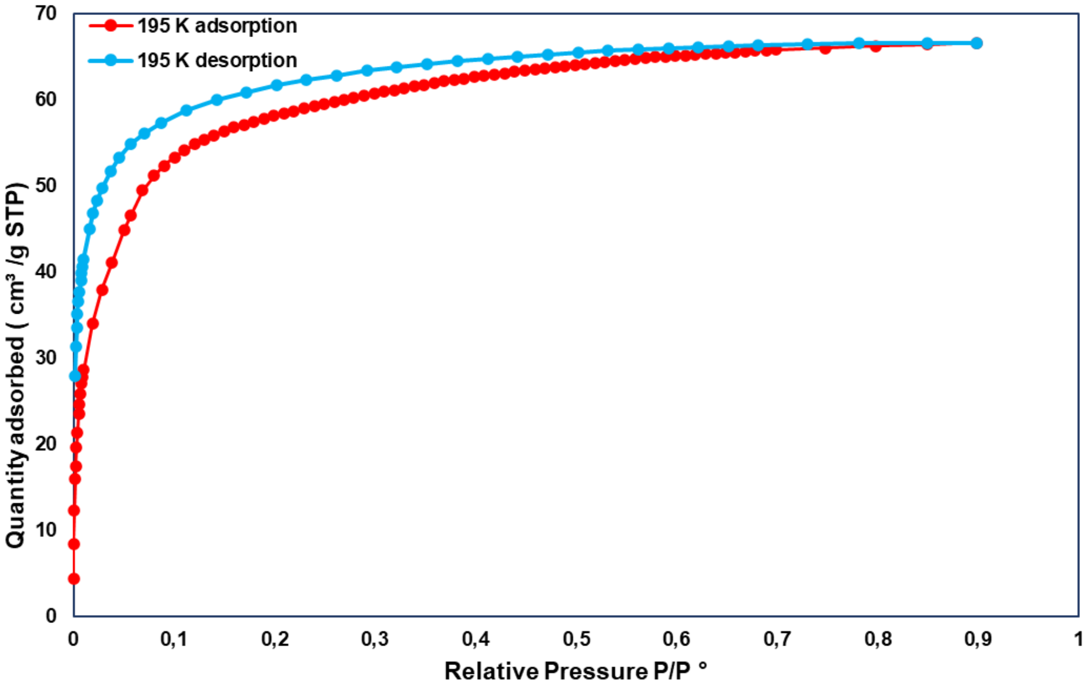

Figure 3.23 CO_2 adsorption (red) and desorption (blue) isotherms of desolvated **LMMOF02** at 195 K.

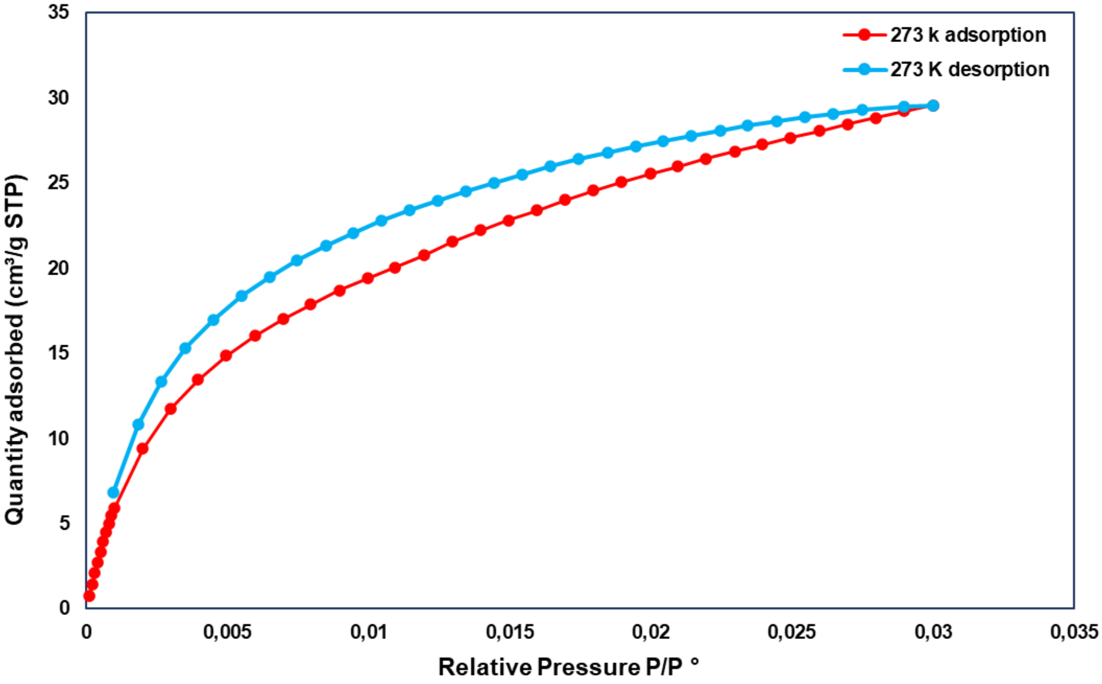

Figure 3.24 CO_2 adsorption (red) and desorption (blue) isotherms of desolvated **LMMOF02** at 273 K.

3.3. LMMOF03

3.3.1. Single-crystal X-ray diffraction (SCXRD)

Crystal structure details of LMMOF03

Molecular formula: $C_{63}H_{53}N_8O_{23}Co_3$

Formula weight: 1466.92 g mol^{-1}

a = 48.175 (3) Å	α = 90°	Space group: *C2/c*
b = 21.8096(1) Å	β = 101.066(2)°	*Z* = 4
c = 16.2927(1) Å	γ = 90°	*V* = 16799.95 (3) Å^3

LMMOF03 was synthesized by reacting *N,N*'–bis–(3-pyridylmethyl)–benzophone diimide (**L1**), terephthalic acid and cobalt(II) chloride hexahydrate in DMF under solvothermal conditions (100 °C, DMF). The MOF crystallizes in the monoclinic space group *C*2/*c*. The ASU consists of one **L1** molecule, three terephthalate anions, three cobalt(II) ions, one coordinated DMF and three uncoordinated DMF molecules (Figure 3.25). The structure has three (3) cobalt ions (Figure 3.26(a)). Co01 is coordinated to six terephthalate ions *via* one (1) oxygen atom, Co02 is coordinated to one **L1** *via* a nitrogen atom, one terephthalate ion *via* an oxygen atom, another terephthalate ion *via* two oxygen atoms and one DMF molecule *via* an oxygen atom. Co03 has the same coordination environment as Co02. The 3-D network of **LMMOF03** is shown in Figure 3.26(b). The packing diagram of **LMMOF03** viewed in the *ab* plane is displayed in Figure 3.27. The structure possesses channels running along the *c* direction occupied by DMF molecules. The solvent-accessible volume of 36.7% was estimated using mercury. and contains 1-D channels (Figure 3.28).

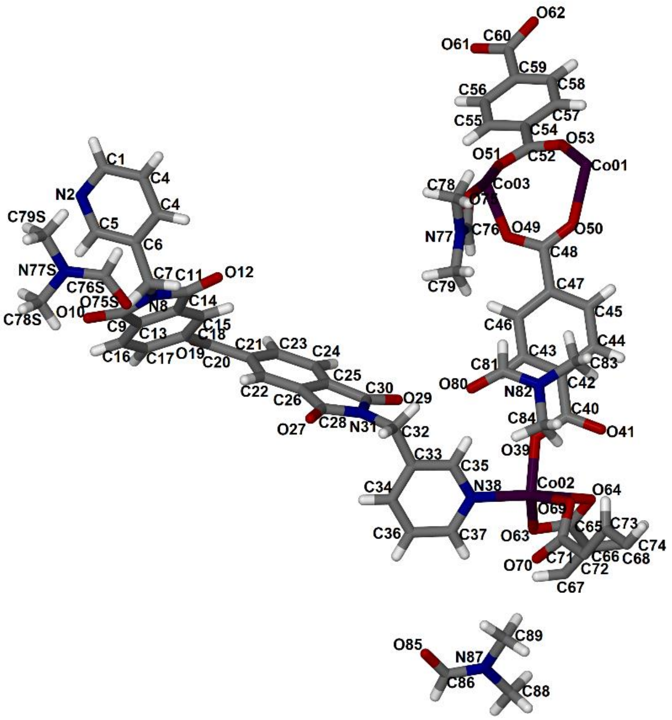

Figure 3.25 The asymmetric unit of **LMMOF03** showing the crystallographic labelling scheme for the ASU.

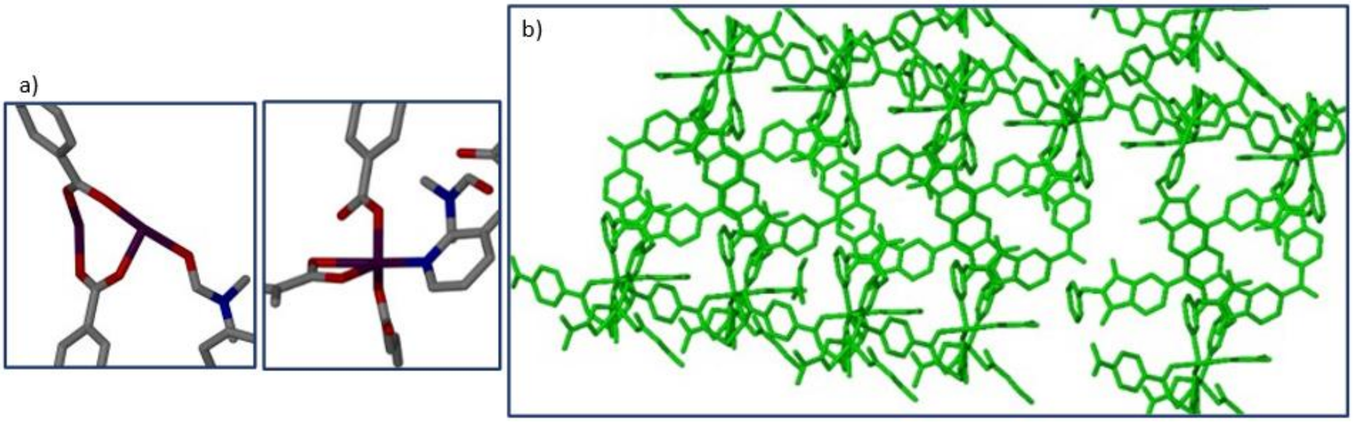

Figure 3.26 (a) The coordination environment around the metal centres and (b) 3-D chain of **LMMOF03**. Hydrogen atoms are omitted for clarity.

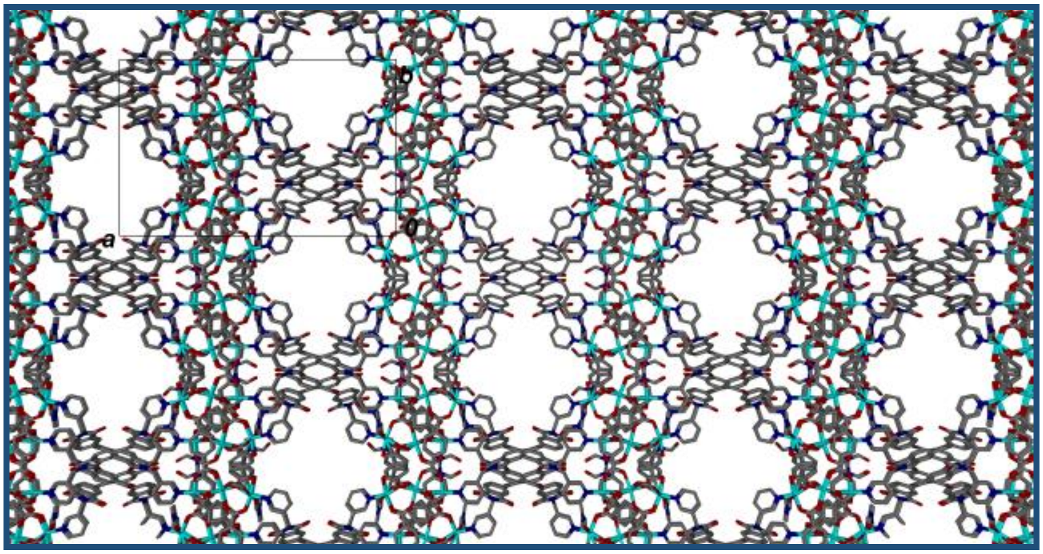

Figure 3.27 The packing diagram of **LMMOF01** viewed down the *c* axis displaying the channels on the MOF structure.

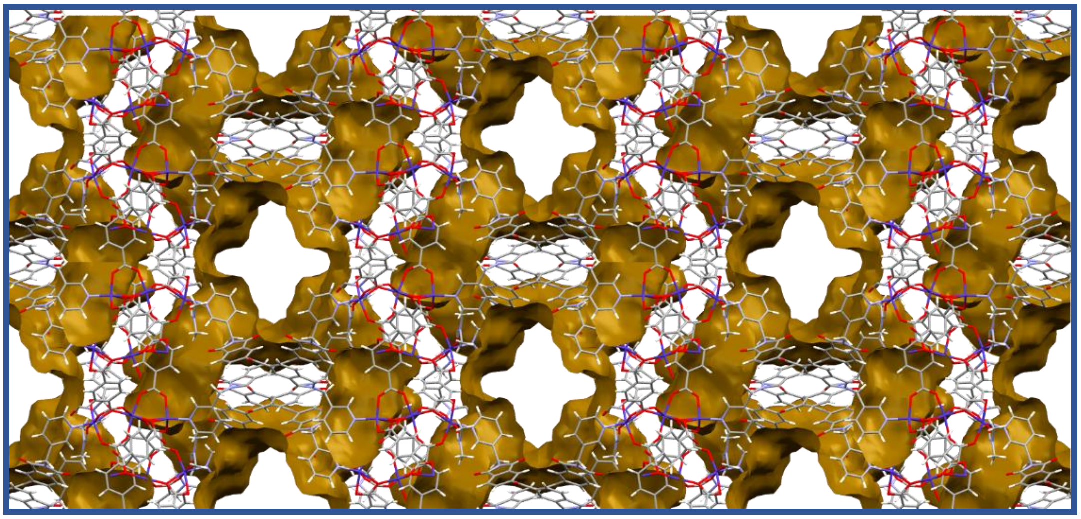

Figure 3.28 A plot of solvent-accessible volume (36.7%) in **LMMOF03** (DMF molecules deleted). The structure possesses 2-D channels.

3.3.2. Powder X-ray diffraction (PXRD)

Crystals of **LMMOF03** were gently ground into a fine powder before being analysed using PXRD. The calculated powder pattern was obtained from the Mercury program and compared to the as-synthesized PXRD pattern. The as-synthesized PXRD pattern does not match with the calculated PXRD (Figure 3.29). The high background on the as-synthesized pattern is possibly due to the fluorescence of the cobalt metal that is present in the MOF, which makes comparisons of the patterns difficult.

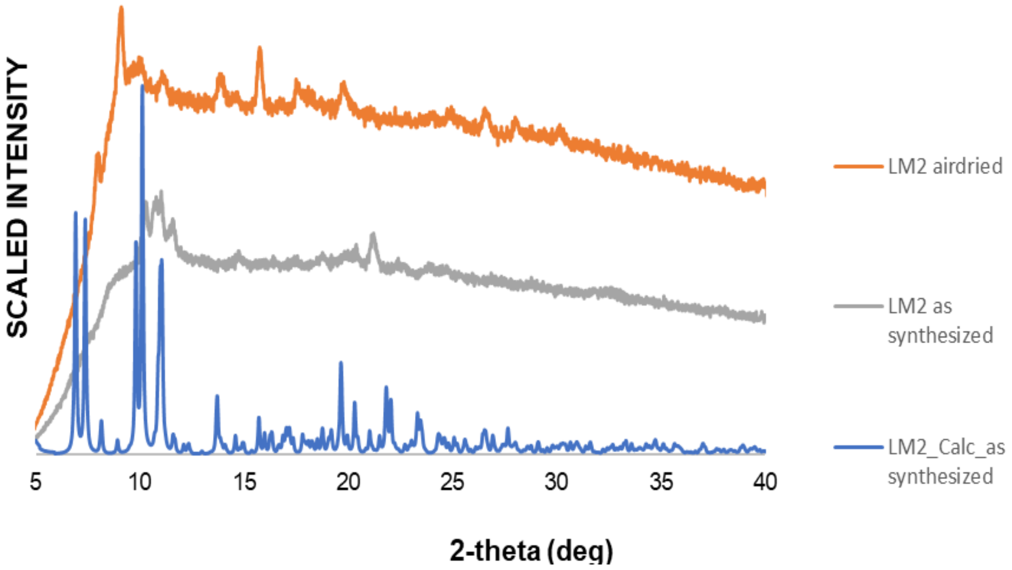

Figure 3.29 LMMOF03 PXRD patterns of calculated (blue), as-synthesized (grey) and air-dried (orange).

3.3.3. Variable-temperature powder X-ray diffraction (VT-PXRD)

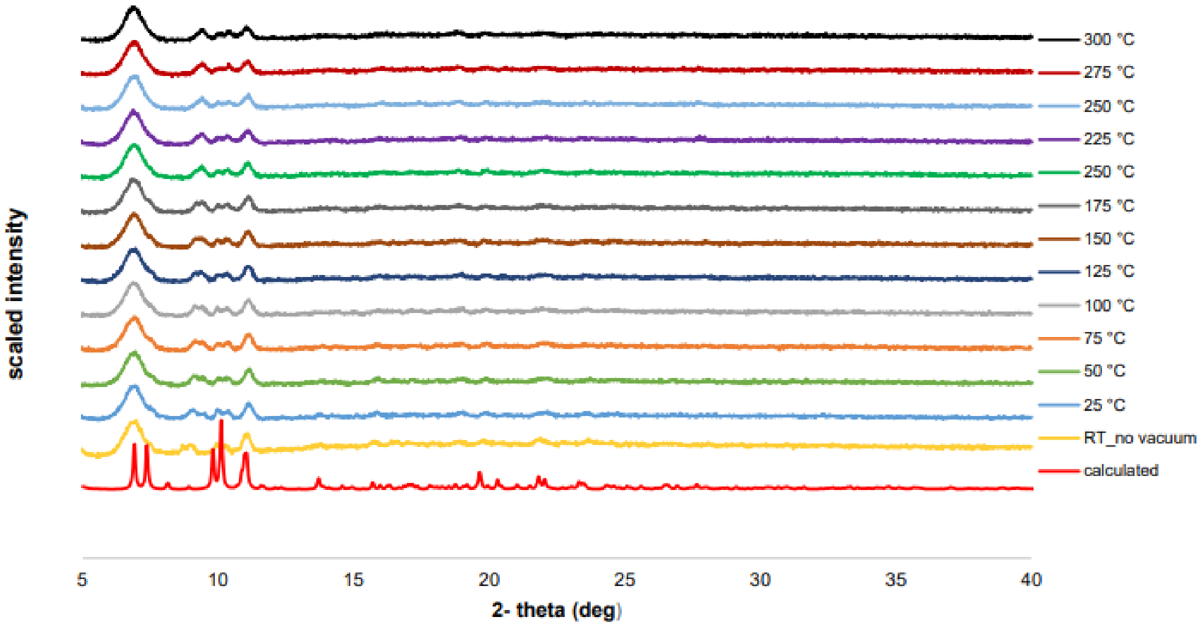

Figure 3.30 VT-PXRD patterns of as-synthesized **LMMOF03** at different temperature.

To determine the stability of the **LMMOF03** at different temperatures, PXRD patterns were recorded at 25 °C intervals from 25 °C to 300 °C. The PXRD patterns show that desolvation begins at room temperature as evidenced by the changes in the PXRD pattern at 25 °C.

3.3.4. Hot Stage Microscopy (HSM)

HSM was conducted on crystals of the as-synthesized **LMMOF03** from 25 °C to 400 °C. The HSM of **LMMOF03** (Figure 3.31) does not show any solvent loss. LMMOF03 crystals become opaque at 200 °C which indicates the loss of monocrystallinity due to desolvation. There is also a notable colour change from light purple to dark purple from 200 °C. The opacification of the crystals is complete at 300 °C. At 390 °C, crystals begin to turn black which indicates the disintegration of the framework.

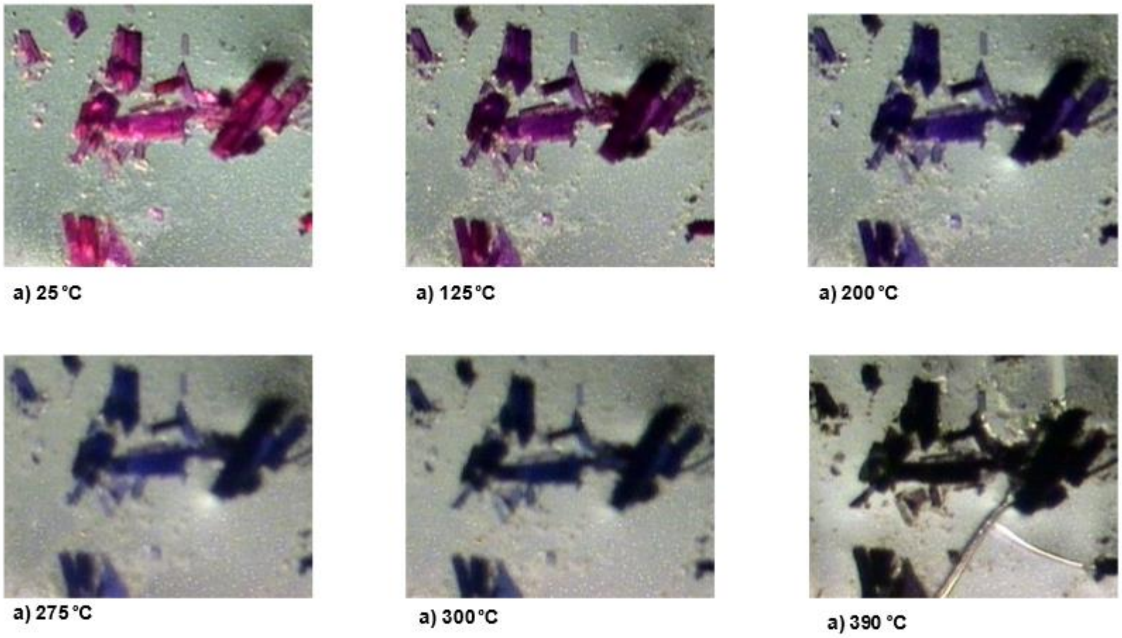
a) 25 °C a) 125 °C a) 200 °C

a) 275 °C a) 300 °C a) 390 °C

Figure 3.31 LMMOF03 HSM snapshots captured at different temperatures: (a) 25 °C, (b) 125 °C, (c) 200 °C, (d) 275 °C, (e) 300 °C and (f) 400 °C.

3.3.5. Thermogravimetric analysis of LMMOF03

TGA was performed to investigate the thermal stability of **LMMOF03**. The thermal profile of the as-synthesized **LMMOF03** shows a total weight loss of 25.24% (calculated 27.69%) in the temperature range of 18 °C to 279 °C (Figure 3.32). The first weight loss from 18 °C to 98 °C is attributed to loss of the free DMF and the second weight loss is attributed to loss of the coordinated DMF in the temperature range of 98°C to 279°C. The framework remains intact from the temperature range of 279 °C – 390 °C and starts to decompose at 390 °C. **LMMOF03** was desolvated by heating the sample under vacuum in situ. Desolvated **LMMOF03** remained stable from 24 °C to 390 °C and its framework only starts to decompose at around 390 °C (Figure 3.8). The TGA results resemble the HSM results.

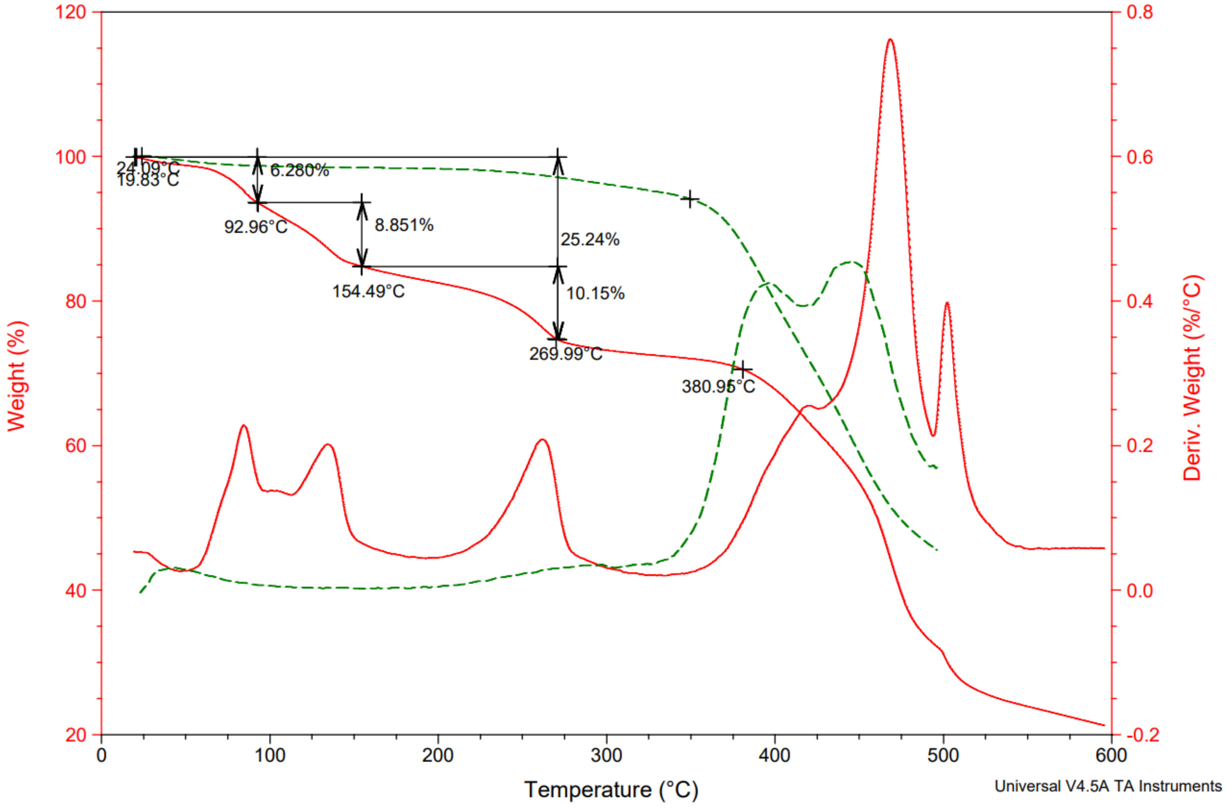

Figure 3.32 TGA profiles of as-synthesized **LMMOF03** (red) and its first derivative (red) and the desolvated **LMMOF03** (dashed lime green) and its derivative weight (dashed lime green).

3.3.6. Gas sorption

The porosity of the desolvated **LMMOF03** was investigated at 195 K and 273 K using CO_2 as the test gas. The compound adsorbs a larger amount of CO_2 at 195 K than at 273 K. At 195 K the quantity of CO_2 adsorbed by **LMMOF03** is 35 cm^3 g^{-1} (STP) while at 273 K the compound adsorbed 12 cm^3 g^{-1} (STP). The sorption isotherms obtained at both 195 K and 273 K display type-I sorption behaviour. The sorption isotherm at 195 K shows hysteresis on the adsorption curve while at 273 K the curve shows no hysteresis.

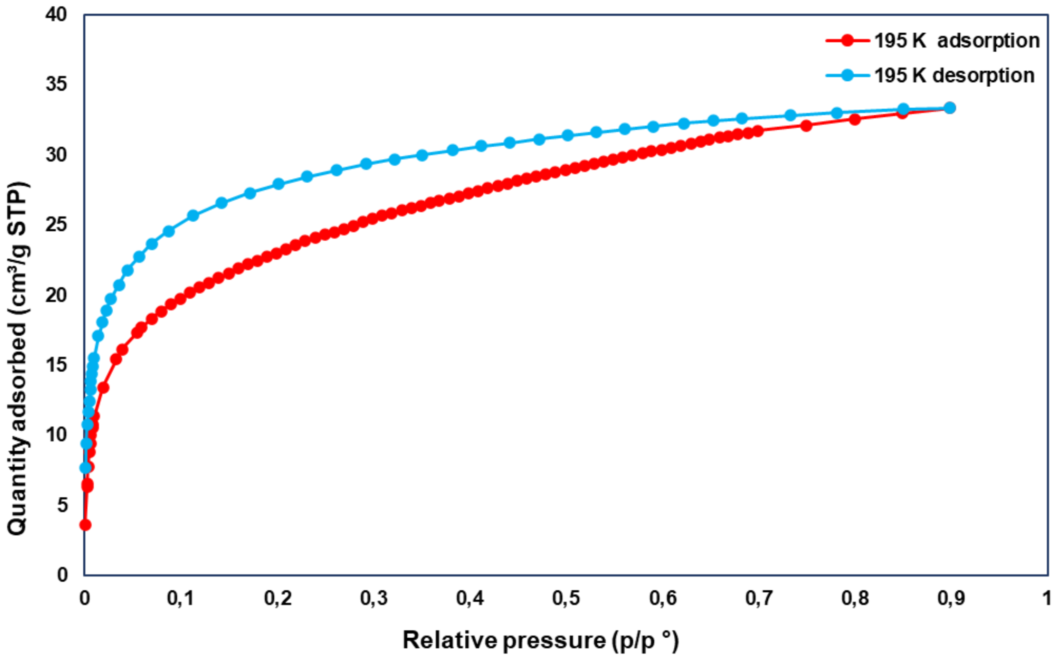

Figure 3.33 CO_2 adsorption (red) and desorption (blue) isotherms of desolvated **LMMOF03** at 195 K.

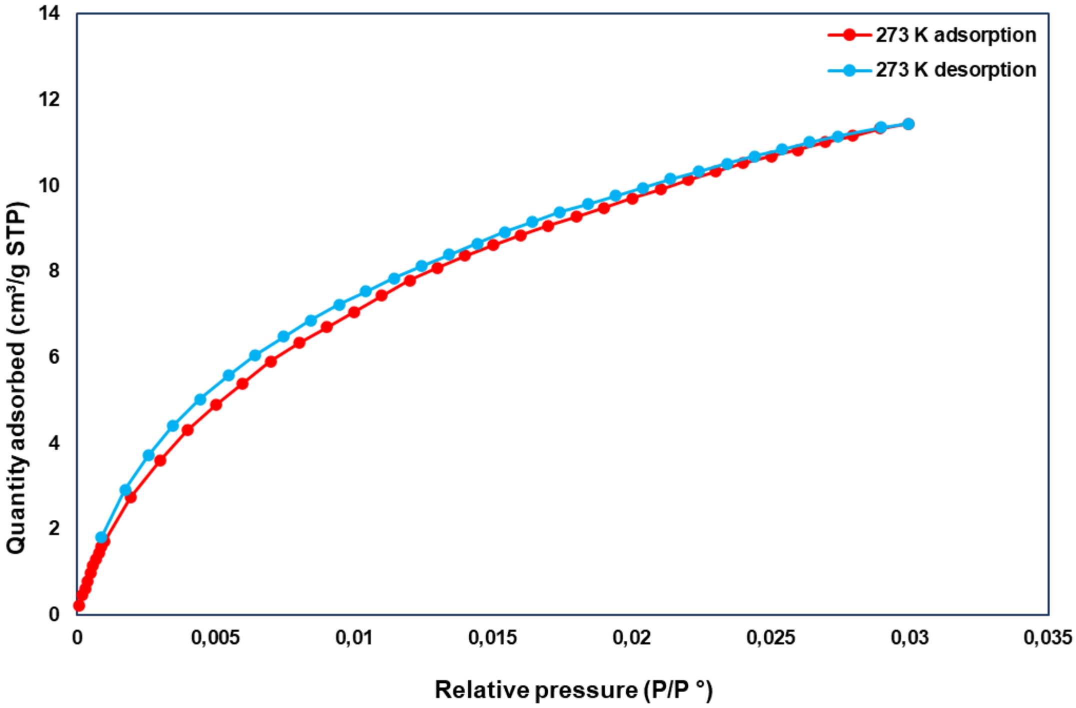

Figure 3.34 CO_2 adsorption (red) and desorption (blue) isotherms of desolvated **LMMOF03** at 273 K.

3.3.7. SUMMARY

Three (3) mixed-ligand porous MOFs namely **LMMOF01**, **LMMOF02** and **LMMOF03** were successfully synthesized using the solvothermal method. The MOFs were fully characterized using SCXRD, PXRD and VT-PXRD. The thermal stability of the MOFs was assessed using TGA and HSM. **LMMOF02** is the most stable MOF with a decomposition temperature of 343 °C. **LMMOF01** and **LMMOF03** decompose at 315 °C and 279 °C respectively. SCXRD showed that **LMMOF01** and **LMMOF03** are 3-D while **LMMOF03** is 2-D. The MOFs have channels of varying sizes occupied by the solvent molecules (DMF). The solvent-accessible volumes and nature of the voids were determined using the Mercury program. It was found that **LMMOF03** has the largest solvent-accessible volume of 36.5% while **LMMOF0**1 and **LMMOF02** possess 30.7% and 31.5% solvent-accessible volumes, respectively. The gas sorption experiments for **LMMOF01** were conducted at 195 K, 273 K, 285 K and 298 K using CO_2 and, at 77 K using nitrogen and hydrogen gases. The sorption capacities of **LMMOF02** and **LMMOF03** were assessed using carbon dioxide gas at 195 K and 273 K. **LMMOF01** showed the highest carbon dioxide adsorption capacity at 195 K, adsorbing a total of 120 cm^3 g^{-1} (STP). **LMMOF01** displays an interesting reversible type-IV isotherm with stepwise CO_2 adsorption. The hysteresis could be indicative of a structural transformation during sorption. In general, the MOFs reported in this chapter show relatively low adsorption capacities of carbon dioxide compared to other MOFs reported in the literature. For example, MOF Cu-BTC showed a CO_2 uptake of 9.59 mmol g^{-1} at 298 K[67] while MOF-177 reaches storage of 320 cm^3 g^{-1} (STP).[67] Another example is ZIF-78, which adsorbs around 60 cm^3 cm^{-3} at 298 K and 800 torr, a value much higher than the CO_2 uptake value of other MOFs at a higher temperature. [68]

Crystallographic data of LMMOF01, LMMOF02 and LMMOF03

Identification code	**LMMOF01**	**LMMOF02**	**LMMOF03**
Empirical formula	$C_{59} H_{40} N_5 O_{17} Zn_2$	$C_{26} H_{19} N_4 O_8 Zn$	$C_{63} H_{53} Co_3 N_8 O_{23}$
Formula weight	1221.70	580.82	1466.92
Temperature	173(2) K	173(2) K	173(2) K
Wavelength	0.71073 Å	0.71073	0.71073 Å
Crystal system	Triclinic	Triclinic	Monoclinic
Space group	*P*1	*P*1	*C2/c*
Unit cell dimensions	a = 14.024(2) Å b = 14.211(2) Å c = 16.787(3) Å α = 78.350(11)° β = 79.244(11)° γ = 67.243(7)°	a = 8.5682(12) Å b = 12.1958(16) Å c = 12.5471(18) Å α = 91.438(2)° β = 99.663(3)° γ =106.671(2)°	a = 48.175(3) Å b = 21.8096(12) Å c = 16.2927(10) Å α = 90° β = 101.066(2)° γ = 90°
Volume	2999.8(9) Å^3	1234.5(3) A^3	16799.95(3) Å^3
Z	2	2	4
Density (calculated)	1.353 g/cm^3	1.563 g/cm^3	1.160 g/cm^3
Absorption coefficient	0.872 mm^{-1}	1.055 mm^{-1}	0.652 mm^{-1}
F(000)	1250	594	6016
Crystal size	0.1 x 0.17 x 0.23 mm	0.10 x 0.10 x 0.10 mm	0.31 x 0.11 x 0.07 mm
Theta range for data collection	2.50° to 27.96°	1.65° to 28.27°	2.19° to 27.12°
Limiting indices	-17<=h<=17, -17<=k<=18, 0<=l<=21	-11<=h<=11, -15<=k<=16, -16<=l<=16	-61<=h<=61, -25<=k<=27, -20<=l<=20
Reflections collected	13344 / 13344 [R(int) = 0.0000]	9575 / 5759 [R(int) = 0.0255]	172519 / 18527 [R(int) = 0.1003]
Completeness to theta = 27.96	92.5 %	93.9 %	99.8 %
Max. and min. transmission	0.9012 and 0.9085	0.9019 and 0.9019	0.9546 and 0.8249
Refinement method	Full-matrix least-squares on F^2	Full-matrix least-squares on F^2	Full-matrix least-squares on F^2
Data/ restraints/ parameters	13344 / 0 / 740	5759 / 0 / 334	18527 / 0 / 901
Goodness-of-fit on F^2	1.804	1.054	1.067
Final R indices [I>2sigma(I)]	R_1 = 0.1588 wR_2 = 0.4357	R_1 = 0.0600 wR_2 = 0.1692	R_1 = 0.0697 wR_2 = 0.2232
R indices (all data)	R_1 = 0.1923 wR_2 = 0.4556	R_1 = 0.0757 wR_2 = 0.1807	R_1 = 0.0950 wR_2 = 0.2496
Largest diff. peak and hole	8.874 and -1.589 e.Å^{-3}	0.729 and -1.225 e.A^{-3}	1.708 and -0.476 e.A^{-3}

CHAPTER 4

ONE-DIMENSIONAL METAL-ORGANIC FRAMEWORKS

RESULTS AND DISCUSSION

This chapter discusses the characterization and structural analysis of 1-D MOFs namely, {[Co(BYP)(**L4**)]·(H_2O)}$_n$ (**LMMOF04**) and {[Cu(**L4**)$_{0.5}$]·(DMF)}n (**LMMOF05**). The MOFs were characterised using X-ray diffraction (SCXRD and PXRD) and thermal analysis (TGA and HSM). The solvent-accessible space of the MOFs was estimated using the program mercury. This chapter is divided per each characterisation technique wherein the analytical results for each compound are discussed. Crystallographic data of **LMMOF04** and **LMMOF05** are given on page 87.

4.1. LMMOF04

4.1.1. Single-crystal X-ray diffraction

Crystal structure details of LMMOF04

Molecular formula: $C_{30}H_{18}N_4O_{10}Co$

Formula Weight: 653.41 g mol^{-1}

a = 11.8161(17) Å	α = 90°	Space group: *Pc*
b = 8.7415(13) Å	β = 90.970(3)°	*Z* = 2
c = 12.9662(19) Å	γ = 90°	*V* = 1339.1(3) Å^3

LMMOF04 was synthesized by reacting *N,N'*-bis(gly)-biphenyl diimide (**L4**), 2,2'-bypiridyl and cobalt(II) chloride hexahydrate in H_2O: EtOH (6 mL:4 mL) under solvothermal conditions (100 °C, 24 hours). **LMMOF04** crystallises in the monoclinic space group *Pc*. The asymmetric unit (ASU) consists of one **L4** molecule, one 2,2'-bipyridyl molecule, one cobalt(II) cation and one coordinated water molecule (Figure 4.1). The Co(II) centre is six-coordinate; the coordination environment comprises two **L4** nitrogen atoms, one oxygen atom of the water molecule and three oxygen atoms of **L4**. The ligand (**L4**) links the metal centres into 1-D chains running along

the *b* axis (Figure 4.2). The packing diagram viewed in the *ac* plane is shown in Figure 4.3. The neighbouring aromatic rings of **L4** and BPY interact *via* π5π interactions.

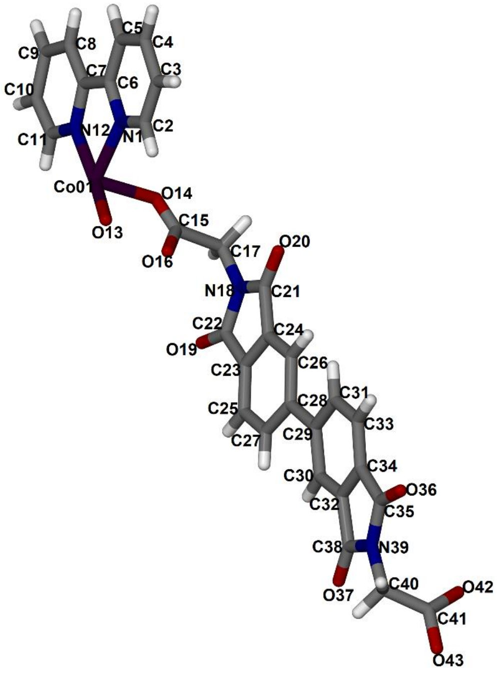

Figure 4.1 The asymmetric unit of **LMMOF04** showing the crystallographic labelling scheme.

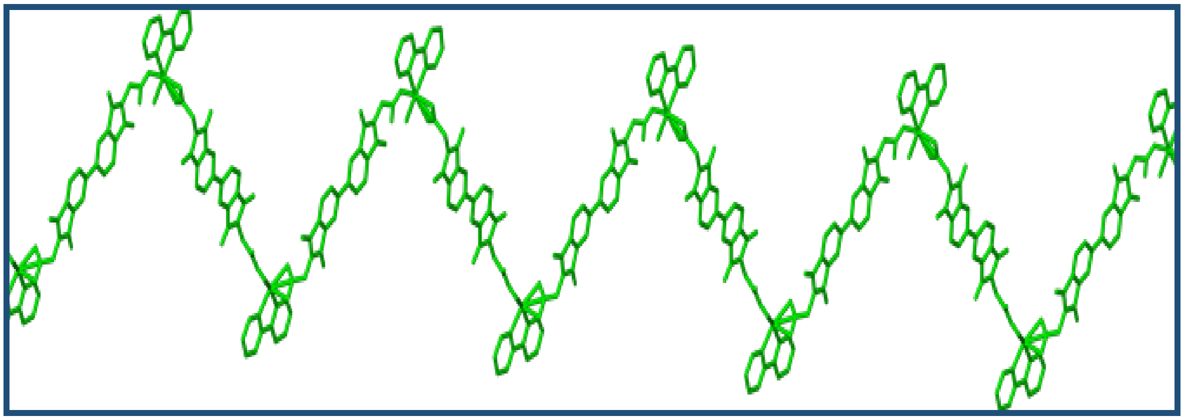

Figure 4.2 The 1-D chains of **LMMOF04** extending in one direction along the *c* axis. Hydrogen atoms omitted for clarity.

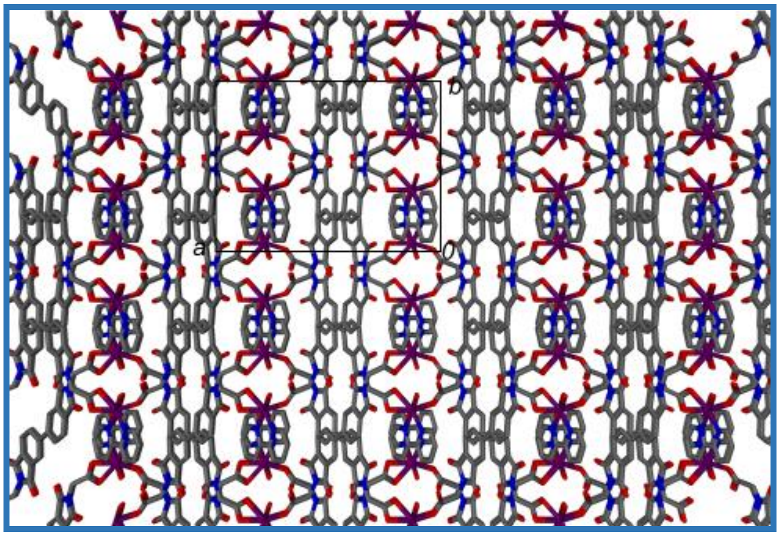

Figure 4.3 The packing diagram of **LMMOF04** viewed down the *c* axis. Hydrogens were omitted for clarity.

4.1.2. Powder X-ray Diffraction

Crystals of **LMMOF04** were gently ground into a fine powder before being analyzed using PXRD. The calculated powder pattern was obtained from Mercury and it was compared to the PXRD pattern of the as-synthesized material. There is a little resemblance between the PXRD pattern of the as-synthesized material and the calculated PXRD. (Figure 4.4). Differences in relative peak heights in the as-synthesized pattern can be ascribed to preferred orientation effects.

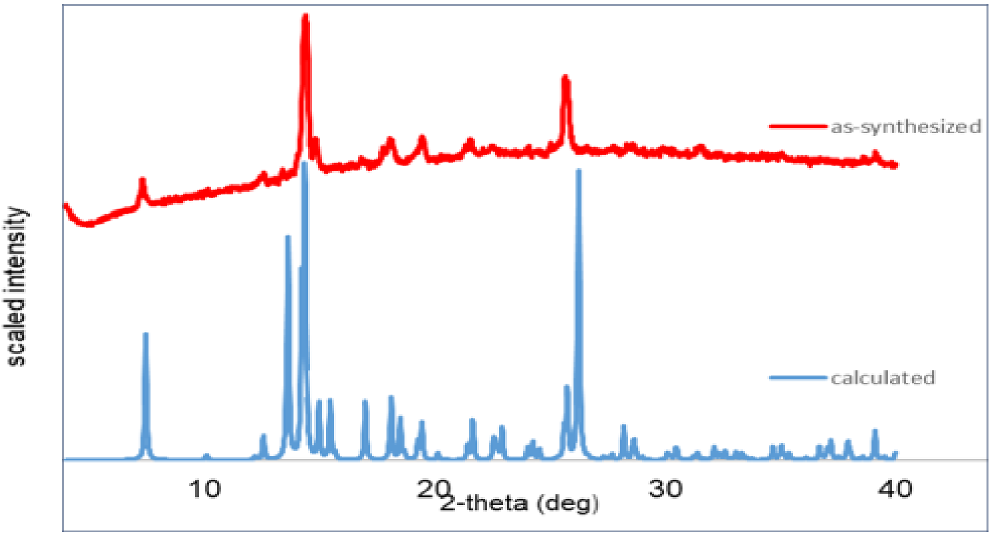

Figure 4. 4 PXRD patterns of calculated **LMMOF04** (blue) and as-synthesized **LMMOF04** (red).

4.1.3. Hot stage microscopy (HSM)

LMMOF04 crystals were heated from 25 °C to 400 °C. The HSM of **LMMOF04** (Figure 4.5) does not show any solvent loss although the TGA graph indicates a weight loss of 3.3% at 97 °C. At 350 °C, crystals are no longer crystalline and they begin to turn brown which indicates the decomposition of the framework. The decomposition process is complete at 400 °C when the crystals are black.

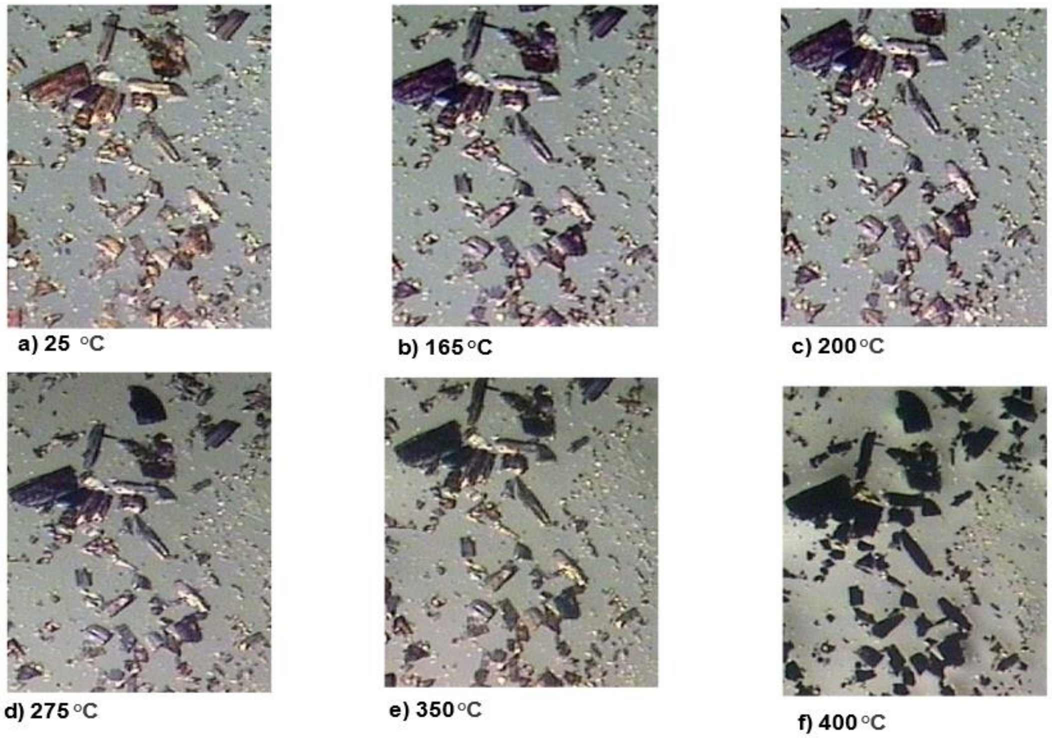

Figure 4.5 Hot stage microscope photographs of **LMMOF04** under silicone oil at different temperatures: (a) 25 °C, (b) 165 °C, (c) 200 °C, (d) 275 °C, (e) 350 °C and (f) 400 °C.

4.1.4. Thermogravimetric analysis

TGA was performed to investigate the thermal stability of **LMMOF04.** The TGA profile of the as-synthesized air-dried **LMMOF04** is shown in Figure 4.6. The curve displays a weight loss of 3.3% (calculated 4.21%) in the temperature range of 30 °C to 97.10 °C which is attributed to the loss of one ligated water molecule. The framework is stable from 97 °C to 350°C, and it starts to disintegrate at 350 °C.

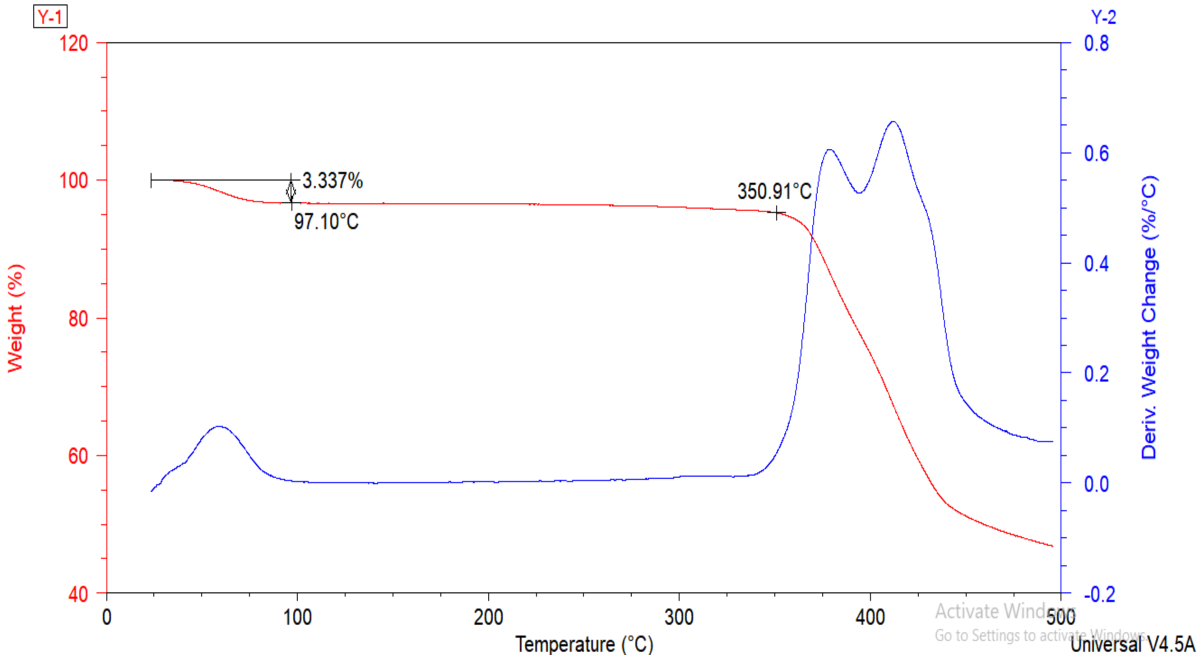

Figure 4.6 TGA profile of as-synthesized air dried **LMMOF04** (red) and the first derivative weight change of the as-synthesized (blue).

4.2. LMMOF05

4.2.1. Single-crystal X-ray diffraction

Crystal structure details of LMMOF05

Molecular formula: $C_{23}H_{12}N_2O_5Cu$

Formula weight: 542.94 g mol^{-1}

a = 24.224(4) Å	α= 90°	Space group: *C2/c*
b = 12.079(17) Å	β = 93.778(3)°	*Z* = 4
c = 7.4827(11) Å	γ = 90°	*V* = 2184.7(5) Å^3

LMMOF05 was synthesised by the reaction of copper(II) chloride hexahydrate, *N,N'-bis*(gly)-biphenyl diimide **(L4)** and phthalic acid in DMF: H_2O (2 mL:4 mL) under solvothermal conditions (100 °C, 96 hours). The phthalic acid co-ligand did not coordinate to the copper(II) ion, it remained unreacted in the solution. The MOF only consists of **L4**, copper(II) ion and DMF. **LMMOF05** crystallises in the monoclinic space group *C2/c*. The ASU of **LMMOF05** consists of

half an **L4** ligand, one Cu(II) ion and one coordinated DMF molecule (Figure 4.7). The Cu(II) ion is coordinated to **L4** *via* an oxygen atom and coordinated to the DMF molecule *via* an oxygen atom. The extension of the 1-D chains of **LMMOF05** viewed onto the *ab* plane is shown in Figure 4.8(a) and the packing diagram viewed onto the *ac* plane is shown in Figure 4.8(b).

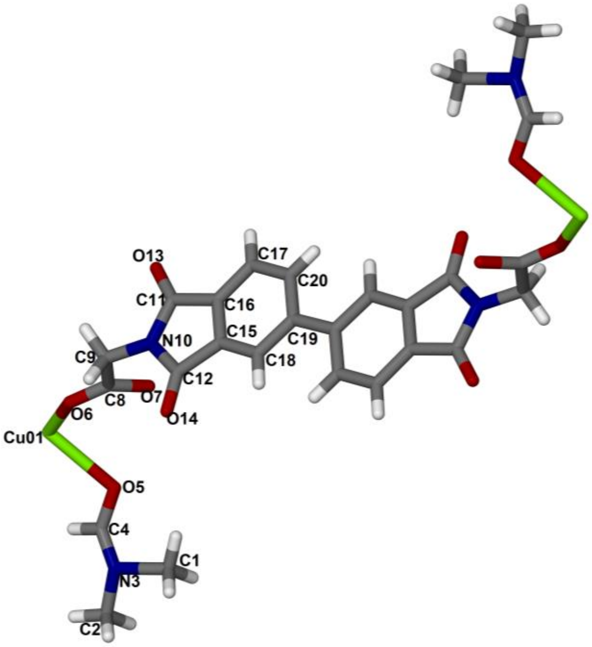

Figure 4.7 The molecular structure of **LMMOF05** showing the crystallographic labelling scheme for the ASU.

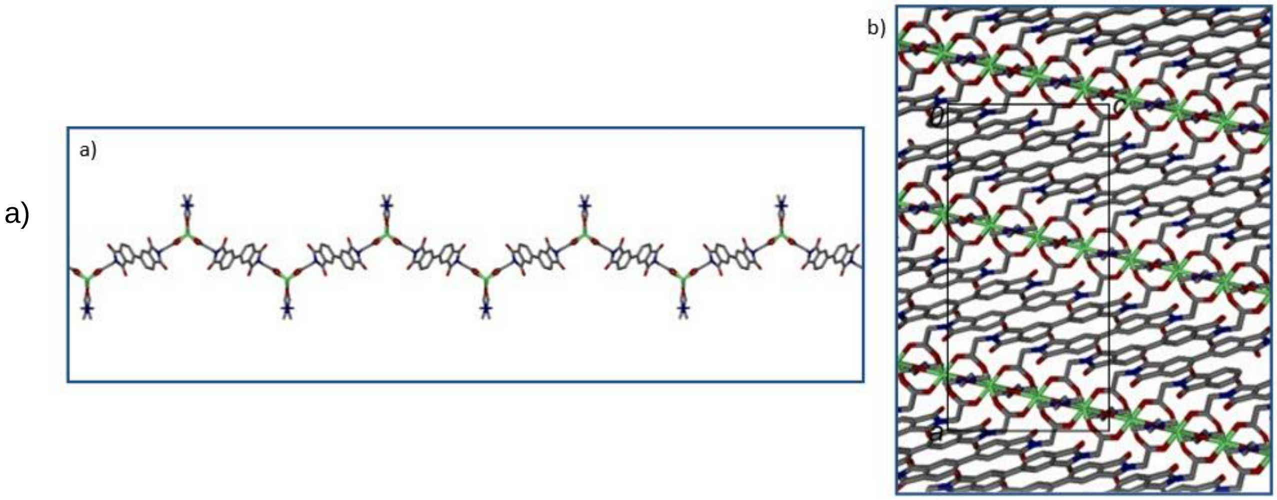

Figure 4.8 (a) The 1-D chains of **LMMOF05** (b) the packing diagram of **LMMOF05** viewed onto the *ab* plane.

4.2.2. Powder X-ray Diffraction

Crystals of **LMMOF05** were gently ground before being analyzed using PXRD. The calculated pattern was generated from Mercury. The PXRD patterns confirmed the purity of the bulk material because the calculated pattern is in good agreement with the as-synthesized pattern (Figure 4.9). The differences in the heights of the comparative peaks in the experimental patterns can be attributed to preferred orientation effects.

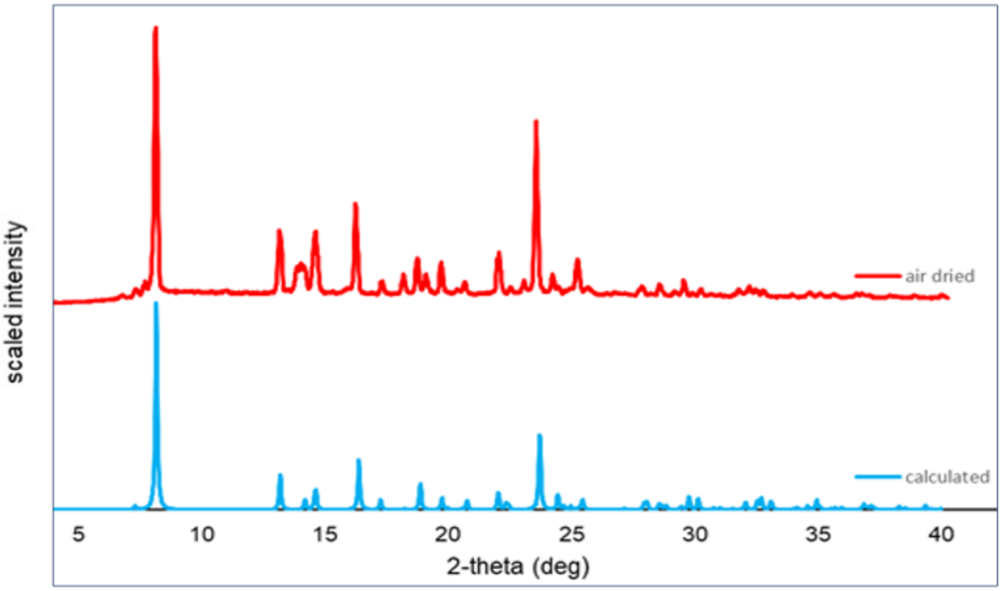

Figure 4. 9 The PXRD patterns of calculated **LMMOF05** (blue) and as-synthesized **LMMOF05** (red).

4.2.3. Hot stage microscopy (HSM)

A few drops of silicone oil were placed over selected crystals which were heated from 25 °C to 400 °C at a heating rate of 10 °C min^{-1} (Figure 4.10). The appearance of bubbles at 70 °C indicates the beginning of the loss of solvent with concomitant opacification. The colour of the crystals changed at 295 °C which indicates decomposition of the MOF. At 365 °C the crystals are completely decomposed. The HSM results complement the TGA results.

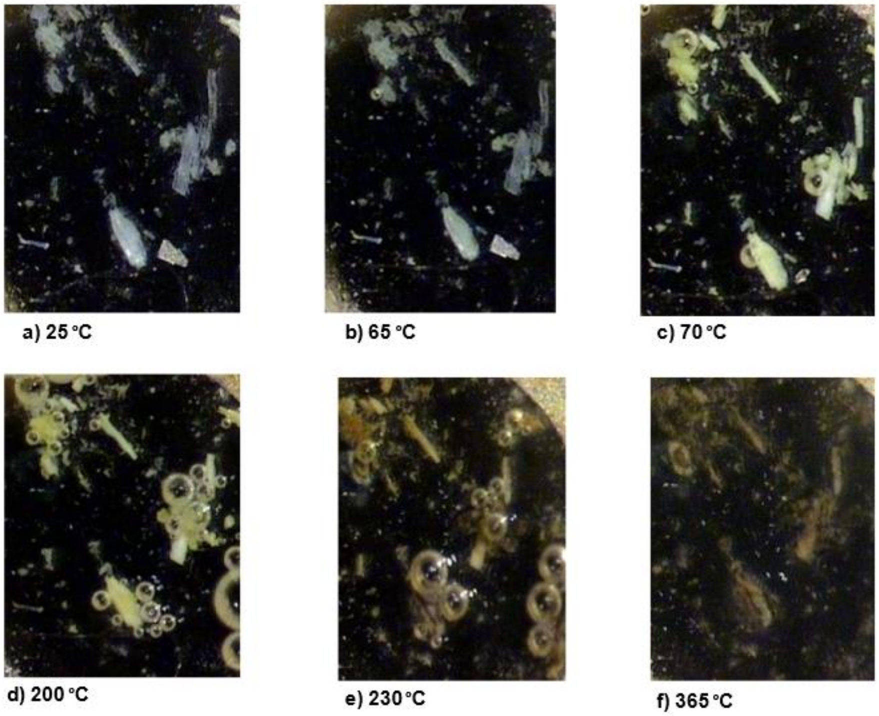

Figure 4.10 Hot stage microscope photographs of **LMMOF05** under silicone oil at different temperatures: (a) 25 °C, (b) 65 °C, (c) 70 °C, (d) 200 °C and (e) 230 °C (f) 365 °C

4.2.4. Thermogravimetric analysis

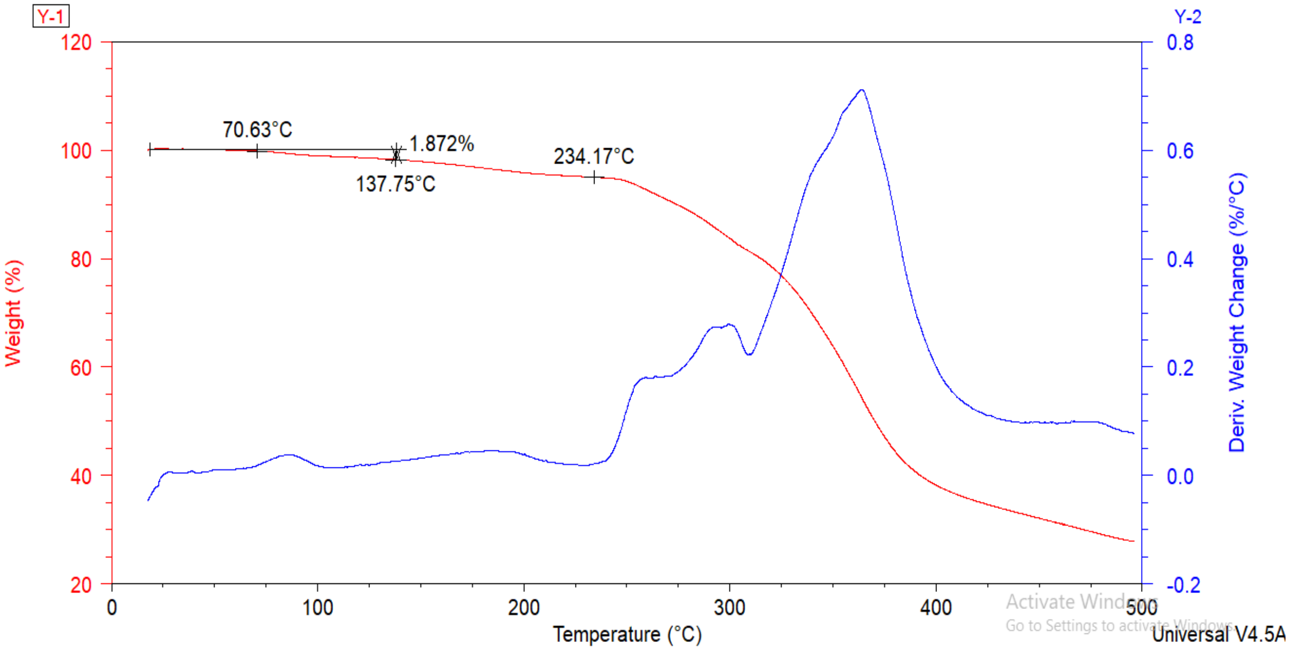

Figure 4.11 TGA profile of as-synthesized **LMMOF05** (red) and the first derivatives weight change of as-synthesized (blue)

The thermal profile of **LMMOF05** is shown in Figure 4.11. The curve displayed a weight loss of 1.9% in the temperature range of 20 °C to 138 °C. The framework is stable from 137 °C to 243 °C and the framework starts to disintegrate at 234 °C. the TGA results correspond with the HSM results. There is a significant weight loss at 70 °C on the TGA which is attributed to the loss of solvent seen at the same temperature on the HSM results. The structure started decomposing at 234 °C.

4.3. SUMMARY

LMMOF04 and **LMMOF05** are novel 1-D MOFs. Both these MOFs contain **L4** which is a novel carboxylic ligand. The thermal stability of the MOFs was determined using TGA. TGA revealed that **LMMOF04** decomposes at 350 °C and **LMMOF05** decomposes at 243 °C. The purity of the MOFs was determined using PXRD. The PXRD patterns confirmed that the chosen crystal for SCXRD is representative of the bulk.

Crystallographic data of LMMOF04 and LMMOF05

Identification code	**LMMOF04**	**LMMOF05**
Empirical formula	$C_{30}H_{18}CoN_4O_{10}$	$C_{23}H_{17}CuN_3O_9$
Formula weight	653.41	542.94
Temperature	173(2) K	173(2) K
Wavelength	0.71073 Å	0.71073 A
Crystal system	Monoclinic	Monoclinic
Space group	*Pc*	*C2/c*
Unit cell dimensions	a = 11.8161(17) Å b = 8.7415(13) Å c = 12.9662(19) Å α = 90° β = 90.970(3)° γ = 90°	a = 24.224(4) Å b = 12.0790(17) Å c = 7.4827(11) Å α= 90° β = 93.778(3)° γ = 90°
Volume	1339.1(3) A^3	2184.7(5) A^3
Z	2	4
Density (calculated)	1.621 g/cm^3	1.651 g/cm^3
Absorption coefficient	0.712 mm^{-1}	1.063 mm^{-1}
F(000)	666	1108
Crystal size	0.10 x 0.10 x 0.10 mm	0.50 x 0.16 x 0.10 mm
Theta range for data collection	1.72° to 25.90°	1.68° to 27.08°
Limiting indices	-14<=h<=14, -10<=k<=10, -15<=l<=15	-30<=h<=30, 0<=k<=15, 0<=l<=9
Reflections collected	25334 / 5105 [R(int) = 0.0431]	2416 / 2416 [R(int) = 0.0000]
Completeness to theta = 29.62 °	99.0 %	100.0 %
Max. and min. transmission	0.9322 and 0.9322	0.9021 and 0.6185
Refinement method	Full-matrix least-squares on F^2	Full-matrix least-squares on F^2
Data/ restraints/ parameters	5105 / 2 / 406	2416 / 0 / 81
Goodness-of-fit on F^2	1.048	1.073
Final R indices [I>2sigma(I)]	R_1 = 0.0943 wR_2 = 0.2495	R_1 = 0.0534 wR_2 = 0.1175
R indices (all data)	R_1 = 0.1213 wR_2 = 0.2779	R_1 = 0.0664, wR_2 = 0.1233
Largest diff. peak and hole	2.462 and -0.731 e.$Å^{-3}$	1.512 and -1.311 e.A^{-3}

CHAPTER 5

CONCLUSION AND FUTURE WORK

5.1. CONCLUSION

In conclusion three (3) pyridyl donor diimide ligands and one (1) carboxylate donor ligand were successfully synthesized and characterized using FTIR and NMR. A search on the CSD (2020, version 5.38) revealed that ligands **L1** and **L4** are novel ligands. **L1** is a pyridyl N-donor ligand containing a benzophenone moiety and **L4** is a carboxylate donor ligand which contains a biphenyl moiety. Five (5) new mixed-ligand MOFs namely **LMMOF01**, **LMMOF02**, **LMMOF03**, **LMMOF04** and **LMMOF05** were prepared solvothermally. The MOFs were characterized using single-crystal X-ray diffraction (SCXRD), powder X-ray diffraction (PXRD) and variable temperature (VT-PXRD).

SCXRD revealed that the synthesized MOFs have different dimensions; **LMMOF01** and **LMMOF03** are 3-D, **LMMOF02** is 2-D, while **LMMOF04** and **LMMOF05** are 1-D. **LMMOF01**, **LMMOF02** and **LMMOF03** have pores of varying sizes occupied by the solvent molecules (DMF). The solvent-accessible volumes and nature of the voids were determined using the Mercury program. It was found that **LMMOF03** has the largest solvent-accessible volume of 36.5% while **LMMOF01** and **LMMOF02** possess 30.7% and 31.5% solvent-accessible volumes, respectively.

The VT-PXRD was conducted on **LMMOF01, LMMOF02** and **LMMOF03**. The patterns show that the crystals of **LMMOF01** and **LMMOF02** retained crystallinity with desolvation up to 300 °C and upon cooling to 25 °C in an open chamber, while for **LMMOF03**, the peaks become broad. The thermal stability of the MOFs was assessed using thermogravimetric analysis (TGA) and hot stage microscopy (HSM). **LMMOF04** is the most stable MOF with a decomposition temperature of 350 °C. **LMMOF01, LMMOF02, LMMOF03** and **LMMOF05** decompose at 315 °C, 343 °C, 279 °C and 243 °C respectively.

The CO_2 sorption capacity of **LMMOF01** was determined at 195 K, 273 K, 285 K and 298 K and the MOF adsorbs 120 $cm^3\ g^{-1}$ (STP), 15.5 $cm^3\ g^{-1}$ (STP), 11.99 $cm^3\ g^{-1}$ (STP) and 8.55 $cm^3\ g^{-1}$ (STP), respectively. At 195 K, **LMMOF01** displays a reversible type-IV isotherm associated with mesoporous materials and characterized by clear, broad hysteresis loops. The curve displays stepwise adsorption with the first structural change observed at $P/P°$ = 0.2 followed by the structure opening wide at 0.35 $P/P°$. The stepwise carbon dioxide adsorption could be due to an increase in the strength of the intermolecular interactions, which induces the opening of the structure. Nitrogen and hydrogen sorption experiments were also conducted on **LMMOF01** at 77 K. The amount of hydrogen adsorbed is 11.99 cm^3 g^{-1} (STP) and the amount of nitrogen absorbed is 3.00 cm^3 g^{-1} (STP). For **LMMOF02** and **LMMOF03**, the sorption capacities were determined using CO_2 gas at 195 K and 273 K. At 273 K, **LMMOF02** adsorbs 30 cm^3 g^{-1} (STP) while **LMMOF03** adsorbs 12 cm^3 g^{-1} (STP). At 195 K, the amount of CO_2 adsorbed increases to 65 cm^3 g^{-1} (STP) for **LMMOF02** and **LMMOF03**, and the amount increases to 35 cm^3 g^{-1} (STP). The adsorption capacities of these MOFs are relatively low when compared to other MOFs reported in the literature, however, the steep uptake of CO_2 gas at low P/P^o signifies a high selectivity of CO_2 which means that these MOFs can find application in direct CO_2 capture and gas separation.

5.2. FUTURE WORK

The objectives of this study were met. However, we planned to assess the gas sorption of the MOFs using both carbon dioxide, hydrogen and nitrogen. Due to challenges associated with COVID-19 and travel restrictions some of the gas sorption experiments could not be completed. Therefore, future work planned for this project includes carbon dioxide sorption experiments for **LMMOF02** and **LMMOF03** at 285 K and 298 K as well as nitrogen gas and hydrogen gas sorption.